Femtosecond spectroscopy studies of incoherent and coherent processes in DNA bases and laser dyes

By

Bing Xue

To

Department of Engineering Science,

Graduate School of Information and Engineering Sciences,

University of Electro-Communications

for the Doctor of Science Degree

March 2016

論文題目： Femtosecond spectroscopy studies of incoherent and coherent processes in DNA bases and laser dyes

審査委員：	小林　孝嘉（主査，主任指導教員）	先進理工学専攻
	奥野　剛史（指導教員）	先進理工学専攻
	美濃島　薫	先進理工学専攻
	森下　亨	先進理工学専攻
	山北　佳宏	先進理工学専攻

承　　諾　　書（博士学位論文）

平成 28年 3 月 25 日

電気通信大学附属図書館長　殿

著作者
氏名　　薛　冰　　印
所属　　情報理工学研究科
学籍番号　　1143005

連絡先
住所　〒182-0024 調布市布田5-3-3
TEL：　　080-3389-0578
e-mail：　xuebing@ils.uec.ac.jp

電気通信大学附属図書館が下記学位論文を利用することを、著作権者である学位申請者として承諾します。

記

１．論　文　名　　Femtosecond spectroscopy studies of incoherent and coherent processes in DNA bases and laser dyes

２．著　者　名　　薛　冰

３．提出年月日　　平成　28 年　3 月　25 日

４．指導教員名　　小林　孝嘉

５．その他（承諾に関しての条件等あれば記入）

【利用許諾の内容】

（１）　電気通信大学学術機関リポジトリに複製・保管した論文を、インターネットを通じて学内外へ公開し、利用者が全文ダウンロードあるいは出力すること。

（２）　電気通信大学附属図書館が、提出したファイルを印刷製本し、附属図書館内への保存及び、学内外の閲覧利用に供すること。

（１）　上記の研究成果に、承諾者以外の著作権者がいる場合は、承諾者はあらかじめ全ての著作権者の同意を得ておくものとする。

（２）　公開後、承諾者がインターネット上での非公開を希望する場合は、承諾者はその旨を付して申請するものとする。

（３）　提出するファイルの様式については、別紙参照のこと。

論文の和文概要

論文題目	Femtosecond spectroscopy studies of incoherent and coherent processes in DNA bases and laser dyes 核酸塩基及びレーザー色素のインコヒーレント・コヒーレント過程のフェムト秒分光
氏　　名	薛　冰

本研究では、電気通信大学先端超高速レーザー研究センターで開発してきた深紫外（DUV）フェムト秒レーザーパルスを光源として、ポンプ・プローブ分光法を活用し、物質の動的な過程及び非線形光学過程を研究した。このレーザーは分光研究用としては、世界最短パルス幅のDUVレーザーである。具体的な研究内容は、ポンプパルスとプローブパルスの間の異なる遅延時間領域における、光により誘起されたインコヒーレント及びコヒーレントな過程を研究対象とした。

正の時間帯領域におけるインコヒーレント現象について、最短パルスである10フェムト秒深紫外レーザーパルスの励起によって、核酸塩基分子の励起状態のダイナミクスを調べた。核酸塩基分子の中のウラシル分子とチミン分子の水溶液を実験対象として、-200から1800フェムト秒までの時間範囲で285nm-260nm(4.35eV-4.76eV)の時間分解差吸収スペクトルを測定した。実験結果の分析によって、その時間分解差吸収スペクトルは2つの寿命成分寿命からなることがわかった。しかも、その２つの成分共に、その寿命の値がプローブ光の光子エネルギーに依存するという驚くべきことがわかった。これらの寿命のプローブ波長依存性を示すスペクトルを、円錐交差（CI、Conical Intersection）を介する緩和過程として理解することが出来る。これまでの先行研究で用いられた深紫外レーザーパルスの幅は、最も短いものでもせいぜい100fs程度であり、全ての論文の結論は、短寿命成分の寿命は100fs以下ということ述べるに過ぎなかった。本研究は1桁高い時間分解能で研究した成果である。

ゼロ遅延時間領域のコヒーレント現象について、非縮退二光子吸収（TPA）断面積測定する新しい方法を考案した。システム構成の利点は、より少ない誤差で測定出来る、TPA係数を直接的に高い確度で計算することがでる。さらに、広帯域TPAスペクトルを、単一の測定手順で取得することができるので、それを用いて、レーザー色素の非縮退2光子吸収断面積を測定した。本研究で測定したレーザー色素（ローダミン6G以外）の非縮退TPA断面積の絶対値については、初めての報告である。ローダミン6Gの報告された縮退TPAの結果と比較して、非縮退TPAはその断面積の増強が確認され、理論計算との対応も良いことが判った。測定実験に使った溶媒によるラマン散乱現象も同時に出現することを見出した。このラマン信号とサンプルのTPA信号との干渉及び区別方法について、考察しそれを取り除きその影響を受けていない２光子吸収スペクトルを得ることに成功した。

Abstract

TITLE	Femtosecond spectroscopy studies of incoherent and coherent processes in DNA bases and laser dyes
NAME	Bing Xue

Pump probe spectroscopy is a powerful method to study dynamic processes in materials or chemical compounds. In this thesis, by using the femtosecond laser pulses, we investigated two kinds of photon induced incoherent and coherent phenomena in the different delay time domain:

The incoherent phenomena: the dynamics of excited states of RNA/DNA base molecule (uracil and thymine) by sub 10 femtosecond deep ultraviolet laser pulses excitation. From experimental result, two probe photon energy dependent lifetime constants were extracted from the difference absorption spectra measurement in the time range up to 1800 fs. From the lifetime constants, the relaxation processes through conical intersection (CI) are clearly understood. The shortest time constant less than 100 fs is assigned to due to relaxation through CI(S_2-S_1) from the first excited S_2 $^1(\pi\pi^*)$ state to the S_1 $^1(n\pi^*)$ state. The second shortest time constant about 1 picosecond is assigned to the relaxation through another CI(S_2^d-S_0) from the deformed excited S_2^d state to the S_0 ground state. Specially the location of CI(S_2-S_1) and CI(S_2^d-S_0) are first time experimentally clarified at 4.33 eV and 4.36 eV for uracil, 4.45 eV and 4.36 for thymine. With the CI width of 0.21 eV and 0.038 eV for uracil, 0.05 eV and 0.031 eV for thymine, respectively.

The coherent phenomena: A new method for non-degenerate two photon absorption cross section measurement was demonstrated and applied for several laser dyes. We improved the traditional method by introducing white light supercontinuum probe and multi-channel lock-in detection. With the advantage of the simplified system structure ensured less error sources, broadband TPA coefficients could be directly acquired in single measurement procedure with high confident data reliability. In this work, several laser dye chromophores are investigated, several of them to be the first reported to our knowledge. Compared to reported degenerate TPA result, an enhancement phenomena was confirmed and discussed with the help of theoretical calculations.

Contents

Chaptor 1: Introduction 1

1.1 Ultrafast lasers 1

1.2 Time-resolved spectroscopy with ultrashort laser 3

1.2.1 Pump-probe experiment 4

1.2.2 The advantages of ultrafast pump-probe spectroscopy 5

1.2.3 Incoherent and coherent processes in time-resolved spectroscopy 6

1.3 Research motivation 8

1.4 Organization of the dissertation 10

Chaptor 2: Supercontinuum and ultrafast deep ultraviolet laser system 15

2.1 Introduction 15

2.2 White light supercontinuum generation 15

2.2.1 White light supercontinuum generation in nonlinear crystals 17

2.2.2 White light supercontinuum generation in noble gas filled hollow fibers 18

2.3 Ultrafast deep-ultraviolet (DUV) laser system 19

2.3.1 Chirped-pulse four wave mixing 20

2.3.2 DUV laser system setup 21

2.3.3 Pulse duration measurement of DUV laser 22

2.3.4 Stability control for the DUV laser system 24

Chaptor 3: Deep ultraviolet pump ultrafast dynamics for uracil and thymine in

aqueous 28

3.1 Introduction 28

3.2 DUV pump and DUV probe experiment 32

3.2.1 Experimental setup 32

3.2.2 Sample preparation 33

3.2.3 Experimental results 35

3.3 Deep ultraviolet dynamics of DNA base: uracil and thymine 38

3.3.1 Assignment of the difference absorption spectra 39

3.3.2 Probe photon energy dependence of lifetimes 41

3.3.3 Relaxation processes though the conical intersection 44

3.3.4 Vibrational dynamics in the DNA bases 50

3.3.5 An attempt for DUV pump and visible probe experiment 54

3.4 Conclusion 57

Appendix I 58

Chaptor 4: Measurement of non-degenerate two-photon absorption spectrum by using super continuum beam 63

4.1 Introduction 63

4.2 Theory of non-degenerate two photon absorption (TPA) 65

4.3 Experimental setup for TPA spectral acquirement 67

4.4 TPA spectral features of the laser dyes 69

4.4.1 TPA spectral features of coumarin 6 and rhodamine 6G in solvent 70

4.4.2 Interference between resonant solute signal and non-resonant solvent signal 72

4.4.3 TPA spectral features of rhodamine 6G in polymer 75

4.4.4 Dependence of the incident pump pulse intensity and sample concentration on the TPA spectra 76

4.4.5 Enhanced phenomenon on non-degenerate TPA cross section 77

4.4.6 Other dyes 79

4.5 Theoretical calculation conformation 80

4.6 Conclusion 83

Appendix II 84

Appendix III 95

Chaptor 5: Summary 99

Acknowledgment 100

Chaptor 1: Introduction

This Chapter is organized in the following way. A short history of the evolution of ultrafast lasers is first introduced in Section 1.1. Then the time-resolved spectroscopy, one of the important applications by using the ultrashort laser, is introduced in Section 1.2. In this section, it is shown that coherent and incoherent processes can be discussed on the common theoretical basis, which is based on the same pump-probe experiment. In Section 1.3, the motivation of the present work is discussed utilizing this concept and methodology. Finally in Section 1.4, the organization of this dissertation is described.

1.1 Ultrafast lasers

The first laser action was reported by Theodore H. Maiman in 1960.[1] The amplified stimulated emission was observed in a ruby crystal under the pump of a flash lamp. After that, lasers and related technologies developed very quickly. Q-switching[3] and mode-locking[4] technologies are among the most successful ones to obtain pulsed lasers. The pulse duration for Q-switched lasers is in nanosecond scale, and that for mode-locked lasers is in the range of several femtosecond to tens of picosecond. Only considering the pulse duration, there are two milestones for the mode-locking technologies and mode-locked lasers. The first one is the colliding-pulse mode-locked dye lasers developed by Shank *et al.* in 1981,[5] which proceeded the pulse duration to sub-100 fs range. The second milestone is the application of an extremely excellent laser crystal - Ti: sapphire crystal in the mode-locked laser system. The shortest pulse duration for the mode-locked lasers is always limited by the spectral width under the restriction of the Fourier transform limit. Thus, a broad gain bandwidth is the key property for the laser medium in ultrashort laser systems. Ti: sapphire crystal has a gain bandwidth of > 450 nm, and it can support a pulse duration of ~1.5 fs (calculated with the Fourier transform limit). In 1991, Sibbett, *et al.*, achieved a pulse duration of 60 fs[6] in a Kerr-lens mode-locked Ti:sapphire laser system. Ten year later, the pulse duration was reduced to 5 fs with intracavity spectra

broadening and a pair of double-chirped mirror for pulse compensation.[7] In 2008, Kärtner and his coworkers obtained the state-of-art result in the mode-locked Ti:sapphire laser with a novel double-chirped mirror pair and CEP control techniques, with the pulse duration of 4.9 fs.[8]

Intra-cavity dispersion compensation is very important for obtaining short pulse using laser medium with broadband gain bandwidth. Typically, a prism pair, a grating pair, a chirped mirror, deformable mirror, and a liquid crystal spatial light modulator are the frequently used for dispersion compensation. Both the intra-cavity dispersion compensation, the extra-cavity compression techniques are used to reduce the pulse duration to even shorter value. The following two processes are involved for the extra-cavity compression technique: (1) Spectral broadening of the ultrashort pulses in nonlinear optical medium, such as bulk materials[9,10] and fibers;[11~13] and (2) Dispersion compensation.

The ultrashort pulses generated in an oscillator always have a pulse energy of nanojoules level. To increase the pulse energy, many works have performed to develop different types of amplifiers. Chirped pulses amplification (CPA)[14] and optical parametric amplifier (OPA)[15] are among the most successful technologies. With CPA technology, the highest pulse energy can reach hundreds of joules, and the highest peak intensity can reach even several petawatts.[16] Besides the large systems, commercial or homemade relatively compact CPA and OPA laser systems are commonly used not only in laser labs, but also in chemistry and material labs.[17~20] Especially in Kobayashi's group, the noncollinear optic parametric amplifier[21] (NOPA) system had been achieving the shortest pulse in reported in visible range since 2011.[22~28] The shortest pulse generated in a visible NOPA in our group has a duration of 2.4 fs (1.1 cycle) and a spectral range of 410-820 nm. Extending over one octave such short pulses are constantly used in the application to spectroscopic research for years.[29,30]

The application of femtosecond laser with such advantageous properties as high

intensity and ultrashort pulse duration can be used in the following two research field of dynamics:

Because of the high peak intensity and ultrashort pulse duration, femtosecond laser pulses are widely used in different research fields. The focused femtosecond laser pulses from an amplifier can easily reach a peak intensity $>10^{12}$ GW/cm^2, and as a result, the light field can be higher than the Coulomb field (about 10^8 V/cm) in an atom.[31] Under such condition, the electric field could be sufficiently inducing field ionization and multiphoton ionization, removing the electrons out of their orbits and accelerating them sufficiently to induce avalanche ionization.[32,33] Therefore, it is possible to study higher-order nonlinear phenomena and multi-photon ionization behaviors in the atoms, molecules, and crystals by using ultrafast femtosecond lasers.

The other is the application of the ultra-short pulse duration to the study of ultrafast physical and chemical processes. The femtosecond laser can be used as a "pinpoint detection" in temporal and special dynamics to record the instantaneous state during material interaction. In temporal domain, the lifetimes of transient states, which play a very important role in chemical reaction study can be as short as in the range of femtosecond. In spatial domain, the velocity of nuclear motion on potential energy surface in the order of 10^3 m/s indicates that nucleus moves only 1 Å in 100 fs.[34] In another words, femtosecond laser allows us to observe the chemical reaction with resolution of sub nanometer.

1.2 Time-resolved spectroscopy with ultrashort laser

Transient spectroscopy (pump and probe experiment) is a powerful technique for probing and characterizing the electronic and structural properties of target molecules' short-lifetime excited states. These states are accessed by the absorption of photons and essentially represent higher energy forms of the molecule, differing from the ground state in the distribution of electrons and / or nuclear geometry. Transient spectroscopy based on femtosecond lasers has been widely used in the study of the early reaction dynamics of photo-excited molecules in the gas phase,[32] in solution,[33]

and in biological environments[34] since last decades.

1.2.1 Pump-probe experiment

In a pump–probe measurement, the system is composed of two pulses, the pump pulse and probe pulse with a time-delay, as shown in Fig1.1. Under the radiation of the ultrashort pump pulse, the electrons of the molecule (sample) are excited from the ground state to the excited states. As a result, the absorbance (A) of the probe pulse will be different between the cases with and without the pump beam, and the difference (ΔA) can be detected with a detector. The difference is due to physical processes for induced in the excited states by internal and / or external molecular processes, such as, radiative / radiationless transition, vibrational relaxation, energy transfer, and electron transfer.[38] By varying the time delay between the pump and probe pulses, it is possible to assemble these responses as a function of the delay time t_D.

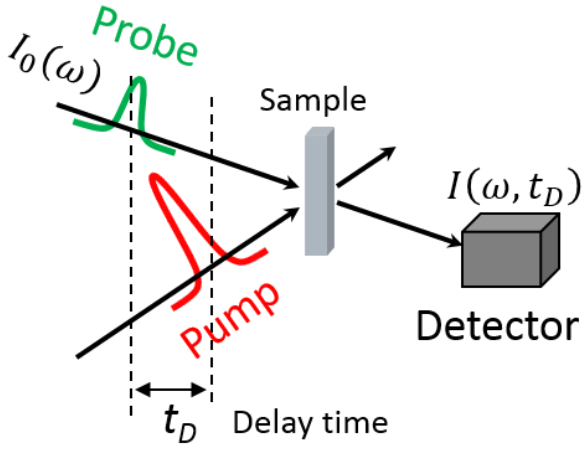

Fig.1.1 Typical pump-probe experimental setup (transmission measurement). The delay time t_D is the arrival time difference between pump and probe pulse.

The absorbance difference ΔA is defined as following equation:

$$\Delta A = -\log\big(I(\omega, t_D)/I_0(\omega)\big). \tag{1.1}$$

Here, ω is the angular frequency of probe light, $I_0(\omega)$ is the initial intensity of probe pulse, $I(\omega, t_D)$ is the detected probe pulse intensity after the sample. With

ultrashort pulses, the probe spectrum will have broadband spectral feature to cover the interest photon energy range. The pulse with duration shorter than the vibrational period under investigation could induce impulsively the vibrational coherence in both the ground state and excited state.[39]

1.2.2 The advantages of ultrafast pump-probe spectroscopy

The ultrafast pump-probe spectroscopy for studies of molecular structures and dynamics in molecules is considered to be the time-domain analog of resonance Raman spectroscopy. However, it has the following characteristic advantages over such conventional vibrational spectroscopy such as ordinary spontaneous Raman scattering:

(1) Resonance Raman signals are frequently submerged in fluorescence signals, especially in highly fluorescent molecules case. In contrast, spontaneous fluorescence interference can be avoided effectively in real-time vibrational spectroscopy because the probe beam is much more intense than the spontaneous fluorescence. The former is more efficiently collected by a detector because of the high directionality due to the coherence in the wave vector space.

(2) Low-frequency modes are difficult to be detected by Raman scattering because of the intense Rayleigh scattering. However, it can easily be studied by pump-probe spectroscopy. The low frequency mode can be detected with the laser spectrum covering a few quanta of the vibrational modes. This requirement can be satisfied by utilizing the nearly Fourier transform-limited ultrashort pulse which has a broad spectrum with constant phase. This condition can be replaced by the way that the pulse duration shorter than the vibrational period of the modes of interest.

(3) As a real-time-domain technique, the pump-probe spectroscopy enables direct observation of vibronic dynamics including time-dependent instantaneous frequencies. Furthermore, small change in frequency shifting in the real-time domain could also be detected. This real-time spectroscopy can also provide information on the vibrational

phase, which is inaccessible with conventional Raman and IR spectroscopy.[40,41]

1.2.3 Incoherent and coherent processes in time-resolved spectroscopy

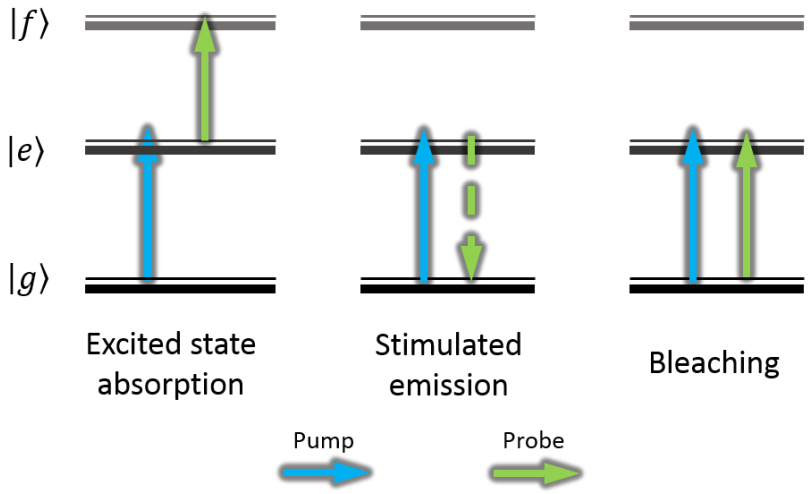

Fig.1.2 Energy diagram for the sequential incoherent pathways of transient absorption.

For the description of a typical transient absorption experiment, we employ a model of three-electronic states composed of the ground state $|g\rangle$, excited states $|e\rangle$ and final states $|f\rangle$. The transient absorption signals are illustrated in the Fig.1.2 with several pathways in energy diagrams. For simplification, the sequences start from the lowest vibrational level in the ground state. This can be satisfied in the case of frequency mode lower than 500 cm^{-1}. The pathways can be classified into three different types after the photon-excitation by the pump pulse. For the bleaching process (BL), the pump pulse reduces the population in the ground electronic state. The probe pulse detect the reduction of the $|e\rangle \leftarrow |g\rangle$ transition intensity due to the depletion population reduction. Other processes involve the feeding of the population to the excited state. The probe light then probes the $|f\rangle \leftarrow |e\rangle$ and the $|e\rangle \rightarrow |g\rangle$ transition, corresponding to the excited-state absorption (ESA) and the stimulated emission (SE), respectively. Paths ESA and SE provide the population dynamics and spectroscopic features of the excited states. On the other hand, BL reflects the amount of reduction of population from the fully equilibrated electronic ground state. It is

considered to have the spectral shape with recovered ground-state absorption spectrum of this homogeneously broadened.

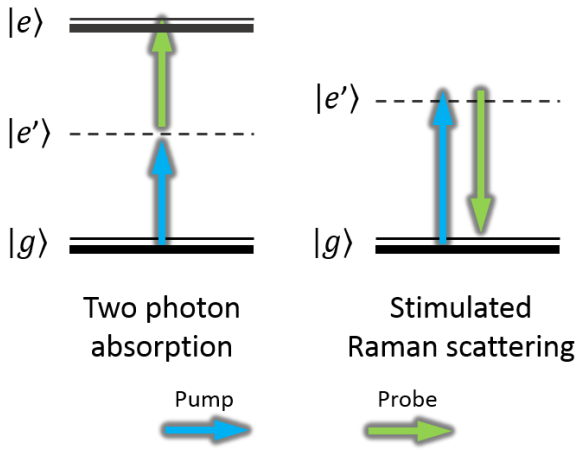

Fig.1.3 Energy diagrams for the coherent pathways of transient absorption.

Furthermore, some other coherent processes may also take place in such transient absorption experiment. In relation with the previous state model shown in Fig.1.2, we employ a virtual intermediate state $|e'\rangle$ into the system shown in Fig1.3. With pump pulse and probe pulse temporally overlap, two transition processes can occur within the coherence time of the polarization, resulting in two photon absorption (TPA) and stimulated Raman scattering (SRS). With the pump photon energy lower than the first excited state $|e\rangle$, one photon absorption will not occur. However, with an intermediate state$|e'\rangle$, TPA may take place, with one pump photon and one probe photon absorbed with the transition $|g\rangle \rightarrow |e'\rangle \rightarrow |e\rangle$. SRS, including Stokes and anti-Stokes scattering, is corresponding to the absorption of a pump photon and subsequent emission of a probe photon via an intermediate state $|e'\rangle$ of a material.[42] SRS and TPA are both third-order nonlinear-optical effect with a real and imaginary susceptibility.[43]

A time dependent transient absorption can be concluded with: $\Delta A(\omega_2, t) = \Delta A_S(\omega_2, t) + \Delta A_C(\omega_2, t)$; here ω_2 is the angular frequency of probe photon, and t is the delay time between pump and probe. The first part on the right of the equation $\Delta A_S(\omega_2, t)$ contains the contributions of BL, ESA, and SE which occur after the excited state already excited by the pump pulse. We call the time within the incoherent range

"positive time". The second part $\Delta A_C(\omega_2, t)$, which contains the contributions from the coherent effects appearing in the "negative time" delay, includes both electronic and vibrational coherence. For TPA, SRS and perturbed free induction decay (PFID), "coherent spike" signal appears during the cross-correlation time between the pump and probe pulses around "zero time" delay. By the measurement of transient absorption in the full time range, plenty of information could be experimentally obtained. Positive time and zero time information are both focused in the two major subjects of this work.

1.3 Research motivation

The main purpose of the researches in this dissertation is to apply our newly developed ultrafast laser systems[21-30] to do some useful studies in chemistry and biology. The spectra of our homemade ultrafast laser systems can cover a range from deep ultra-violet (DUV, 200 ~ 300 nm) to near infrared range, and the pulse duration are all shorter than 10 fs. They are powerful tools for ultrafast time-resolved spectroscopy researches. The reasons for choosing the samples of DNA / RNA nucleobases and laser dyes are shown as follows.

DNA (deoxyribonucleic acid) and RNA (ribonucleic acid) are among the most important substances in the world because they carry the gene information for living creatures. After the identification and isolation of DNA for the first time by F. Miescher in 1869,[44] it is well known that DNA is composed of simpler units called nucleotides. There are four kinds of nucleotide molecules: cytosine (C), guanine (G), adenine (A), and thymine (T). RNA has a single-stranded form instead of the double-stranded form for DNA. RNA also has four base molecules which are a little bit different from DNA, and the four base molecules for RNA are C, G, A, and uracil (U). The five base molecules for DNA and RNA have similar absorption properties in DUV range. Previous researches are focused on the high photostability of these molecular, because it is of supreme importance for the stability of genetic information. The high photostability commonly attributed to efficient radiationless deactivation processes

after excitation to the excited state by absorbing a DUV photon.[45] The photostability is due to two extremely fast decay channels of the excited state. The process is composed of two processes of which decay times one shorter than 100 fs and the other is several picosecond.[46,47] The values of both time constants reported are highly scattering. The dispersed values of the short lifetime (<100 fs) are considered to be due to the laser pulses used in experiments having 100 fs range. To obtain more precise information for the short lifetime, DUV pulses with even shorter duration are necessary. A stable, microjoule-level, sub-10 fs DUV laser pulse has been constructed in Kobayashi group,[48] and it provides capability to study the sub-100 fs dynamics of the DNA and RNA base molecules with high enough resolution and accuracy. In this dissertation, the ultrafast dynamics in U and T are investigated with our homemade 9.6 fs DUV laser system, and clear dynamic of the relaxation processes are observed and the detailed mechanism of the ultrafast relaxation in the system is proposed.

Organic laser dyes can be characterized in solid, liquid, or gas phase with an intense absorption band in the visible spectral range. Among the three phases, the liquid solutions of dyes are the most convenient one for the dye laser research because of their high optical quality. Laser dyes were the most commonly used laser media for ultrafast lasers in the past decades. However, it gradually faded out our sight after the appearance of solid state lasers and fiber lasers these days. Although laser dyes are still widely used in some other fields, such as in biological microscopy as the fluorescent labels. For example, rhodamine 123 can be used to determine membrane potential in mitochondria and a variety of other cells including bacteria and murine leukemia cells;[49] Nile red can be used in the detection and quantification of intracellular lipid droplets in various biological system including algae, yeasts and filamentous fungi.[50] Two photon excitation microscopy (TPEM) is a widely used imaging technology in these days.[51] This imaging technique utilizes the TPA phenomena with the advantages of deeper detection depth and lower photon damage effects by using the low excitation photon energy. One of the most important key points in TPEM is to choose the best suited fluorescent labels for the samples. Many elements should be considered during

the selection, such as TPA cross section, laser damage threshold, photon bleaching, and fluorescence quantum efficiency. Laser dyes show high potential to be used in TPEM because of their high laser damage threshold, high quantum efficiency and high threshold for the photon bleaching. It is known that some laser dyes have large TPA cross sections and have been used for TPEM.[52,53] However, the detected TPA spectral shapes and values of cross section of most laser dyes are still unknown. The TPA cross sections for even most commonly used fluorescent labels are measured with only several discrete wavelengths, and it is difficult to find the a wide range of continuously plotted TPA spectrum in the records. In this dissertation, a broadband non-degenerate TPA cross section measurement method based on pump-probe experiment is demonstrated, and it is used in the investigation on TPA features for several commonly used laser dyes for the first time. The method also can be used to calibrate the TPA features of other fluorescent labels such as fluorescent proteins and quantum dots, and even of some molecules without fluorescent emission.

1.4 Organization of the dissertation

This dissertation is organized as follows:

In Chapter 2, the generation of supercontinuum and DUV pulses are introduced. They will be used as the light sources for pump-probe experiments in this dissertation. The pump-probe experimental setup based on the home-made DUV laser system is demonstrated with the combination of the high precision multi-channel lock-in amplifier detection system. Furthermore, for the feasibility of pump-probe experiment application, the optimization of DUV laser system is made with the stability improved to less than 2% in RMS noise.

In Chapter 3, the sub 10 fs DUV laser system is applied to the ultrafast pump-probe experiments for two selected DNA / RNA bases, T and U. With the ultrashort DUV pulse pump, two different probe pulses (DUV and supercontinuum) are proposed to be used. Within the electronic decay analysis, probe photon energy dependent lifetime components are extracted from experimental results. The relaxation processes

of U and T are clarified and also discussed based on the probe photon energy dependent lifetimes.

In Chapter 4, the principle of the measurement of TPA cross section with non-degenerate pump-probe experiment is firstly introduced. A setup with the fundamental beam (directly from the Ti:sapphire amplifier) as the pump and white light supercontinuum beam as the probe is demonstrated for the measurement of TPA cross section spectrum. Compared with other ordinary methods, this method has the advantages on broadband detection, simplified system structure and less systematic error. The TPA cross sections for several laser dyes are measured with this method. A comparison is given for our results and some reported results. The influence of the stimulated Raman scattering of solvent is also discussed in this Chapter.

References:

1. T.H. Maiman, Nature, **187**, 493 (1960).
2. A. Einstein, Phys. Z, **18**, 121 (1917).
3. F.J. McClung, R.W. Hellwarth, Journal of Applied Physics, **33**, 3, 828 (1962).
4. W. E. Lamb Jr., Phys. Rev. **134** (6A), A1429 (1964).
5. R. L Fork, B. I. Greene and C. V Shank, Appl. Phys. Lett., **38**, 671 (1981).
6. D.E. Spence, P. N. Kean, and W. Sibbett, Opt. Lett., **16**, 42 (1991).
7. R. Ell, U. Morgner, F. X. Kärtner, J. G. Fujimoto, E. P. Ippen, V. Scheuer, G. Angelow, and T. Tschudi, Opt. Lett., **26**, 373 (2001).
8. H. M. Crespo, J. R. Birge, E. L. Falcão-Filho, M. Y. Sander, A. Benedick, and F. X. Kärtner, Opt. Lett., **33**, 833 (2008).
9. K. Dharmadhikari, F. A. Rajgara, and D. Mathur, Appl. Phys. B, **80**, 61 (2004).
10. C. Rolland, and P. B. Corkum, J. Opt. Soc. Am. B, **5**, 641 (1988).
11. A. Baltuška, Z. Wei, M. Pshenichnikov, and D. A. Wiersma, Opt. Lett., **22**, 102 (1997).

12. M. Nisoli, S. De Silvestri, and O. Svelto, Appl. Phys. Lett., **68**, 2793 (1996).

13. M. Nisoli, S. Stagira, S. De Silvestri, O. Svelto, S. Sartania, Z. Cheng, M. Lenzner, Ch. Spielmann, and F. Krausz, Appl. Phys. B, **65**, 189 (1997).

14. P. Hauri, W. Kornelis, F. W. Helbing, A. Heinrich, A. Couairon, A. Mysyrowicz, J. Biegert, and U. Keller, Appl. Phys. B, **79**, 673 (2004).

15. G. E. Cook, IEEE Proc. IRE **48**, 310 (1960).

16. M. Li, B. Zhang, Y. Dai, and T. Wang, J. Opt. Soc. Am. B 27, 1534-1542 (2010).

17. N.D. Spencer, J.H. Moore, Encyclopedia of Chemical Physics and Physical Chemistry: Fundamentals, (Taylor & Francis, 2001).

18. X. Yang, K. Liu, Modern Trends in Chemical Reaction Dynamics: Part I: Experiment and Theory (World Scientific, 2004).

19. R. A. Baumgartner and R. L. Byer, IEEE J. Quantum Electron. QE-15 (6), 432 (1979).

20. R. L. Byer and A. Piskarskas (eds.), JOSA B 9, 1656–1791 (1993) and 10, 2148–2243 (1993).

21. A. Shirakawa, I. Sakane, M. Takasaka, and T. Kobayashi, Appl. Phys. Lett., **74**, 2268 (1999).

22. A. Shirakawa, H. W. Mao, and T. Kobayashi, Teq. Rep. IEICE LQW94-60 35-40 (1994).

23. A. Shirakawa, H. W. Mao, and T. Kobayashi, Opt. Commun. **123** 21-128 (1996).

24. A. Shirakawa and T. Kobayashi, Appl. Phys. Lett. **72** (2) 147-149 (1998).

25. A. Shirakawa and T. Kobayashi, IEICE Trans. Electron **81**-C 2246-253 (1998).

26. A. Shirakawa, I. Sakane, and T. Kobayashi, Opt. Lett. **23** 16 1292-1294 (1998).

27. A. Baltuška, T. Fuji, T. Kobayashi, Opt. Lett., **27**, 306 (2002).

28. K. Okamura and T. Kobayashi Opt. Lett. **36** (2) 226-228 (2011).

29. T. Kobayashi, J. Du, W. Feng, K. Yoshino, Phys. Rev. Lett., **101,** 037402 (2008).

30. I. Iwakura, A. Yabushita, and T. Kobayashi, J. Am. Chem. Soc. **131**, 688 (2008).

31. M. D. Perry, D. Pennington, B. C. Stuart, G. Tietbohl, J. A. Britten, C. Brown, S. Herman, B. Golick, M. Kartz, J. Miller, H. T. Powell, M. Vergino, and V. Yanovsky, Opt. Lett., **24**, 160 (1999).

32. M. Castillejo, S. Couris, E. Koudoumas, and M. Martin, Chem. Phys. Lett., **308**, 373. (1999).

33. E.G. Gamaly, S. Juodkazis, K. Nishimura, H. Misawa, B. Luther-Davies, L. Hallo, P. Nicolai, and V.T. Tikhonchuk, Phys. Rev. B, **73**, 214101 (2006).

34. A.M.D. Lee, "Chemical Reaction Dynamics and Coincidence Imaging Spectroscopy", dissertation, Department of Chemistry in Queen's University, Canada (2007).

35. H. Zewail. Femtochemistry: Atomic-scale dynamics of the chemical bond using ultrafast lasers (nobel lecture). Angew. Chem. Int. Ed., 39:2586–2631, (2000).

36. J. Assmann, M. Kling, and B. Abel. Watching photoinduced chemistry and molecular energy flow in solution in real time. Angew. Chem.–Intern. Ed., 42:2226–2246, (2003).

37. V. Sundström. Femtobiology. Ann. Rev. Phys. Chem., **59**:53–77, (2008).

38. Brian Wardle, Principles and Applications of Photochemistry, 2009th ed. (Wiley, n.d.).

39. I. Iwakura, A. Yabushita and T. Kobayashi, Chem. Phys. Lett., **457**, 421 (2008).

40. I. Iwakura, A. Yabushita and T. Kobayashi, Phys. Rev. B, **76**, 052201 (2007).

41. W.T. Pollard, Soo-Y. Lee, and R.A. Mathies, J. Chem. Phys., **92**, 4012 (1990).

42. A.M. Weiner, D.E. Leaird, Gary P. Wiederrecht, and K.A. Nelson JOSA B, **8**, 1264-1275 (1991).

43. Y.R. Shen, The Principles of Nonlinear Optics (J. Wiley, New York, 1984) p.203.

44. F. Miescher, Medicinisch-chemische Untersuchungen, **4**, 441–460 (1871).

45. N.K. Schwalb and F. Temps, Science **322**, 243 (2008).

46. C.E. Crespo-Hernandez, B. Cohen, and B. Kohler, Nature **436**, 1141 (2005).

47. W.J. Schreier, T.E. Schrader, F.O. Koller, P. Gilch, C.E. Crespo-Hernández, V.N. Swaminathan, T. Carell, W. Zinth, and B. Kohler, Science **315**, 625 (2007).

48. Y. Kida, J. Liu, and T. Kobayashi, Appl. Phys. B **105**, 675 (2011).

49. D. Lloyd, Flow Cytometry in Microbiology: Technology and Applications (Caister Academic Press, 2013) p.70.

50. I.R. Sitepu, L. Ignatia, A.K. Franz, D.M. Wong, S.A. Faulina, M. Tsui, A. Kanti, K. Boundy-Mills, J. Microbiol. Methods, **91**, 21-328 (2012).

51. F. Helmchen, W. Denk, Nat Methods., **2**, 932-40 (2005).

52. J. Fölling, V. Belov, D. Riedel, A. Schönle, A. Egner, C. Eggeling, M. Bossi, and S.W. Hell, Chem. Phys. Chem., **9**, 321–326 (2008).

53. G. Moneron, S.W. Hell, Opt. Express, **17**(17), 14567 (2009).

Chaptor 2: Supercontinuum and ultrafast deep ultraviolet laser system

2.1 Introduction

As described in Chapter 1, Sub-10fs pulses in NIR, visible, and UV can be generated with OPA, especially NOPA system. These pulses also have been already used in the pump-probe experiments.[1-5] It is still of great importance to extend the wavelength range of the ultrashort pulses. Some other nonlinear processes can be used to generate other wavelengths, such as DUV pulse generation with four-wave mixing (FWM) process and supercontinuum white light generated with self-phase modulation (SPM) and some other nonlinear processes. In this section, we will focus on the generation of supercontinuum white light and DUV pulses. Since the spectral range and stability of the generated pulses are very important for the applications in pump-probe experiments, we also have tested different parameters to obtain the most suitable spectral range and the most stable pulses.

2.2 White light supercontinuum generation

Supercontinuum generation is firstly reported by Alfano and Shapiro in bulk glass[8] in 1970, and then a wide variety of nonlinear media, including bulk materials, liquids, gases, and waveguides, are proved to be suitable for supercontinuum generation. The mechanism of the supercontinuum generation is very complicated, since many nonlinear processes and linear processes are involved. However, experimental and theoretical studies[9] has been carried on for the mechanism over decades. Among all the linear and nonlinear processes, the laser filamentation is thought to be the key process in the supercontinuum generation, especially for case of pump pulse with a duration in femtosecond range.

During the laser filamentation, many linear and nonlinear optical processes are involved, such as diffraction, space-time defocusing, group velocity dispersion (GVD), self-focusing (SF), self-phase modulation (SPM), Raman induced Kerr effect, self-

steepening, photo-ionization, plasma defocusing. Filamentation usually leads to extensive spectral broadening, in which the optical Kerr effect plays a key role, and the plasma generation also will induce the blue shift of the spectrum. The spectral broadening during the filamentation can be described by the following equations.[10]

$$\omega(t) = -\frac{\partial \phi}{\partial t} \sim \omega_0 + \frac{\omega_0 z}{c}\left(-n_2 \frac{\partial I(r,t)}{\partial t} + \frac{1}{2n_0 \rho} \frac{\partial \rho(r,t)}{\partial t} \right) \tag{2.1}$$

$$\frac{\partial \rho}{\partial t} = \sigma_K I^K \rho_{at} \tag{2.2}$$

$$n = n_0 + n_2 I(r,t) \tag{2.3}$$

Here ϕ is temporal phase of the pulse, z is the propagation distance, ω_0 is the fundamental frequency of the pulse, $\partial I / \partial t$ is the temporal slope of the pulse, n is the refraction index of the medium, ρ is the time dependent plasma density, and the quantity σ_K denotes the coefficient of the multiphoton ionization rate $W_{MPI} = \sigma_K I^K$ involving K photons, where $K \equiv \langle U_i / \hbar\omega_0 + 1 \rangle$, U_i denotes the ionization potential of the medium and ρ_{at}, the density of neutral atoms. In Eq. (2.1) we can see the new frequency is generated by competition between SPM and plasma defocusing effect, which correspond to the two parts in the brackets at the end of the equation. For white light supercontinuum (WLSC) generation in positive nonlinearity media, the wavelength of commonly used pulse laser is near IR, while the WLSC is more effectively using on the blue shifting of the source spectrum. Then the maximum broadening scales as $\Delta\omega_{\max} \propto I_{\max}^K$, where $I_{\max}^K$ is the clamping intensity in the filament. Thus the chromatic dispersion of the nonlinear medium is important for spectral broadening. In a short conclusion, propagation distance, incident pulse condition, and nonlinear medium properties, these three features mainly determines the characteristic of the generated WLSC.

In this work, WLSC is used as idler beam for ultrafast DUV pulse generation and as one of the probe beams in the research of ultrafast dynamics in DNA bases in

Chapter 3; and also be used as probe beam in the measurement of non-degenerate two-photon absorption spectrum in Chapter 4. Two kinds of the transparent medium are used for WLSC generation with different application purposes, the detailed configurations will be discussed in the following two subsections.

2.2.1 White light supercontinuum generation in nonlinear crystals

With the simplest configuration, the nonlinear crystal is more usually used for the generation of white light supercontinuum (WLSC). By simply focusing the pump fundamental beam into the transparent crystal with pump power adjusted properly, the WLSC is obtained easily. As an example, sapphire plate is introduced for the seed beam preparation in the sub-10-femtosecond NOPA laser system in the group of Kobayashi.[1-4] In the present study, the WLSC generated in a nonlinear crystal provides extremely useful broadband visible probe light pulse.

By using the WLSC as probe beam, stabilities of intensity and shapes of its broadband spectrum are considered to be the most important parameters. Especially for the stability, there are mainly two concerns of short-time (few seconds) and long-time (longer than one hour) features. For the short-time stability, even though the noise could be large reduced by introducing the multi-channel lock-in amplifier (MLA) detector, higher stability will still helpful to acquire more reliable results. On the other hand, for the time-resolved spectroscopy, the typical measurement time for acquiring full delay time span from -200 fs to 2000 fs is required for one to two hours. Therefore, the long-time stability of the light source is of vital importance in every pump-probe experiment.

In Fig.2.1 (a) the generated WLSC spectrums are illustrated with a comparison by using different nonlinear mediums. They are one 2-mm thick YAG crystal plate and a 2-mm thick sapphire plate. The pump power is adjusted to maximize the output beam intensity under the condition with no indication of the multi-filament, respectively. In the spectral shape, the two medium shows similar properties. However from the intensity stability features shown in Fig.2.1 (b), the sapphire plate shows

much better short-time and long-time stabilities, compared to the YAG crystal. During even longer time tests within one to two hours, the intensity of WLSC generated by YAG crystal is continuously reducing. The reason could be explained as the effects of thermal damage. Relatively, the sapphire plate has a better performance. Therefore, we concluded that the 2-mm sapphire plate is the better nonlinear materials for the WLSC generation, and it is used for generating broadband visible probe beam in this dissertation.

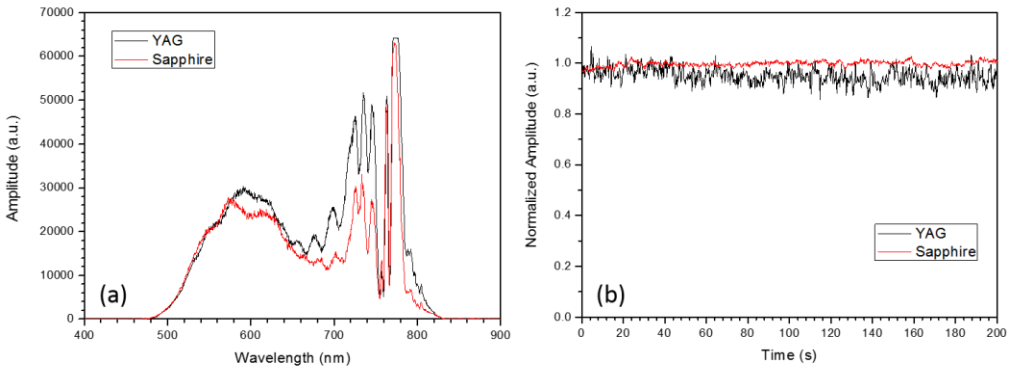

Fig.2.1 (a) White light supercontinuum spectrum generated by sapphire plate and YAG crystal plate. (b) The intensity of the two species of generated white light supercontinuum, compared by the integrated spectral range of 480 ~ 830 nm.

2.2.2 White light supercontinuum generation in noble gas filled hollow fibers

Sometimes higher output energy is required for the WLSC generation. In this case, the bulk mediums are not suitable anymore, even though the setup is simple and convenient. Because the multi-filamentation phenomenon is taking place when high input beam power is introduced, which is harmful for the WLSC stability. Instead, with the advantage of high threshold, a hollow fiber filled with noble gas is more frequently used. Another advantage for this method is that, the broadened spectrum could be easily controlled by changing the pressures of filled noble gas. In Fig.2.2, the spectral broadening features are measured by different argon gas pressures filled in the hollow fiber. As we can see, the spectral width is increased with the increasing of gas pressure. For the purpose of generating a broadband DUV pulses with higher output energy in

this dissertation, high energy and controllable spectral of the WLSC are needed. Therefore, the WLSC generation in the hollow fiber would be the only choice. In the actual operation, the gas pressure is optimized with consideration of the tradeoff between the chirping control and the output intensity for the DUV beam (details will be discussed in the next subsection).

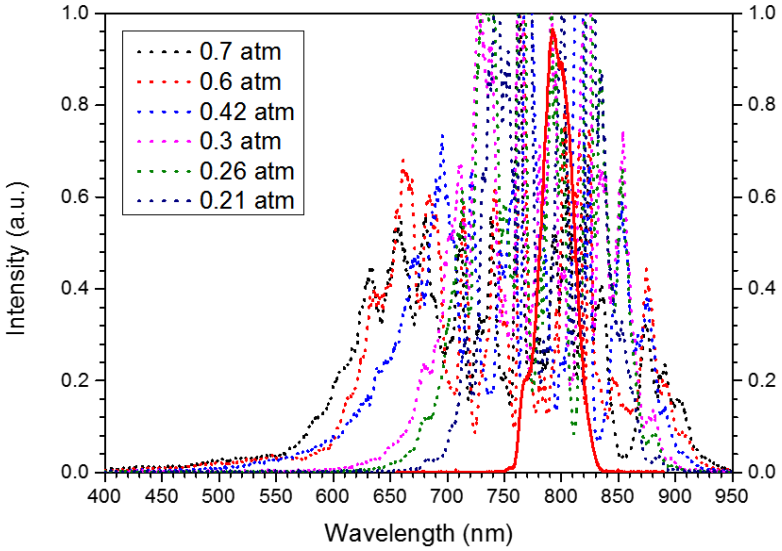

Fig.2.2 Spectral broaden status by different gas pressure in hollow fiber.

2.3 Ultrafast deep-ultraviolet (DUV) laser system

Based on the well-developed Ti: sapphire lase system, deep ultraviolet (DUV) pulse is generated by the third harmonic generation via sum frequency mixing of the fundamental and the second harmonic, or the four wave mixing through nonlinear materials.[9-12] Typically, by these methods, the pulse durations are limited in hundreds of femtosecond. Several systems for sub-10 fs DUV pulse generation were reported previously, but it has not yet well applied to the real time spectroscopy application yet because of the following difficulties. For the spectroscopy purpose, a proper clean structure with free chirp pulse is strongly demanded in a common. When the DUV pulse transmitted in the air, the effect of group velocity dispersion (GVD) is much more severe than in the visible case, which always leads to substantial pulse broadening. And during the pulse compensation by using prism or grating compressor, satellite

pulses are always generated by high order nonlinear effects, resulting a distortion between the pump and probe pulse in the pump-probe experiment. These reasons causes the difficulties of ultrashort pulse compensation in DUV range.

2.3.1 Chirped-pulse four wave mixing

In this work, we generate ultrashort DUV pulses by introducing a new method called "chirped-pulse four wave mixing",[13,14] which based on four wave mixing (FWM) process. By this method, the generated DUV pulses could be chirping controlled by the initial pulses condition. Without additional compressor introducing sub pulses after the generation, the chirping problem of DUV pulses could be automatically cancelled when propagating in the air.

The basic FWM energy conservation in the can be expressed by:

$$\omega_{pump} + \omega_{pump} - \omega_{idler} = \omega_{signal} \tag{2.1}$$

Here ω_{pump}, ω_{idler}, and ω_{signal} refers to the pump, idler, and signal angular frequencies, respectively. In chirped-pulse four wave mixing, the pump and idler pulses are given with linear chirp. The angular frequencies of the pump and idler pulses can be given in the following equation:

$$\omega_{pump}(t) = 2\omega_0 + \beta_{pump}t \tag{2.2}$$

$$\omega_{idler}(t) = \omega_0 + \beta_{idler}t \tag{2.3}$$

Here, ω_0 is the center angular frequency of the idler, and β_{pump} and β_{idler} are the chirp rates of the pump and idler pulses, respectively. Then by Eq. (2.1) the DUV signal pulse frequency could be given by:

$$\omega_{signal}(t) = 3\omega_0 + (2\beta_{pump} - \beta_{idler})t \tag{2.4}$$

In Eq. (2.4), the chirping condition of the signal beam is relied to the second part of the right side of the equation. Therefore the chirp of signal beam could be controlled by the initial chirp rates of idler and pump pulses. With this method, ideal zero chirp DUV pulse after propagating a certain distance (at the sample point) can be obtained

by controlling the chirp of incident idler and pump beam, respectively. In the present work, chirp rates of idler beam are adjusted by a pair of chirp mirrors, and the pump pulses are frequency chirped by a pair of gratings (details are shown in the next subsection).

2.3.2 DUV laser system setup

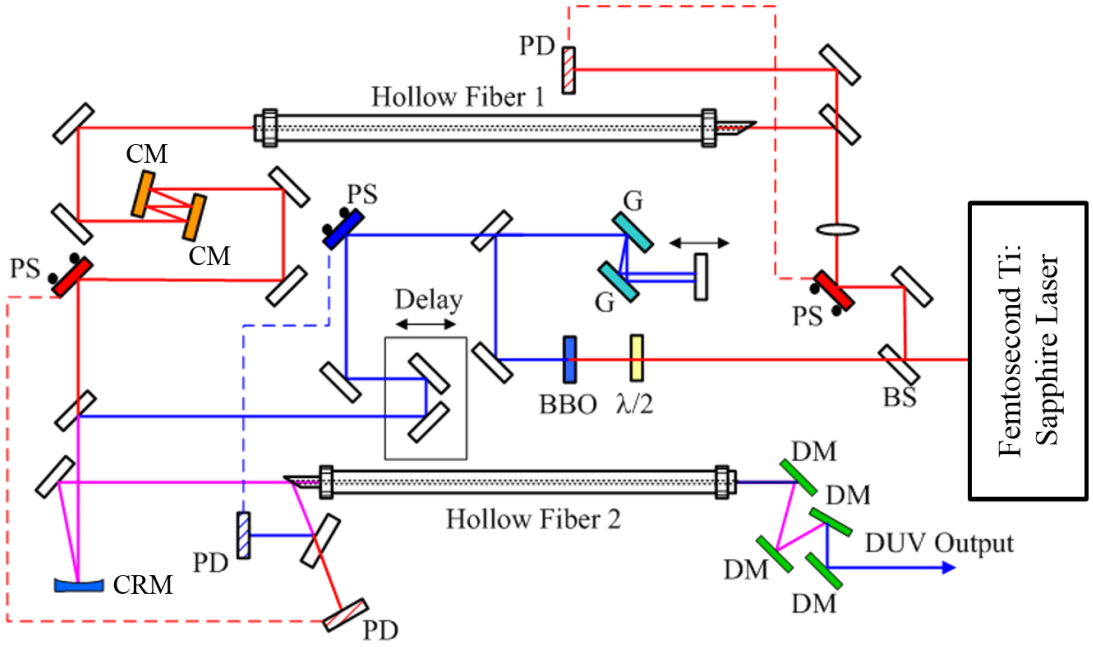

Fig.2.3 DUV system setup scheme. BS, beam splitter; PS, beam pointing stabilizer; PD, detector for beam pointing stabilization; G, grating; CM, chirp mirror; CRM, concave reflection mirror, DM, dichroic mirror.

In order to obtain suitable DUV pulses for ultrafast spectroscopy, a chirp-controlled DUV laser system is demonstrated by using chirped-pulse four-wave mixing method (CFWM).[13,14] The system scheme is depicted in Fig.2.3. The laser source is Spitfire Ace from Spectra Physics. The specifications of the laser are as follows: 50 femtosecond pulse duration with 1-kHz repetition rate, center wavelength is 798 nm, FWHM of the spectrum is 20 nm, total output power is 5 W. Generally, a near UV (NUV) pulse is first generated by using the second harmonic (SH) generation from the fundamental pulse. The laser power before the BBO crystal is 600 mW. After the dichroic mirror by removing the fundamental beam, the NUV is negatively chirped by a double-passed grating pair. Another fundamental pulse is focused into a hollow-core

fiber (250 μm core diameter, 60 cm length) filled with krypton gas (0.7 atmospheric pressure) to obtain supercontinuum with broadband spectrum in NIR. The NIR is automatically positively chirped during the spectrum broadening. Furthermore, the chirp is modified by introducing a pair of chirp mirrors. Then the positively chirped NIR pulse and negatively chirped NUV pulse are spatially and temporally overlapped into another hollow core fiber (140 μm core diameter, 60 cm length) filled with argon gas (0.1 atmospheric pressure). In this second hollow-core fiber, by CFWM processing, a broadband and negative chirp DUV pulse is generated.

After the second hollow fiber, the negative chirped output pulse experience positive GVD in the air. Then a clean and well-compressed DUV pulse can be obtained at an appropriate distance just after this second hollow fiber. After collimation of the output beam, the NIR and NUV pulses are removed by four dichroic mirrors (DMs) one after the other.

2.3.3 Pulse duration measurement of DUV laser

For ultrafast DUV pulse duration measurement, self-diffraction frequency-resolved optical gating (SD-FROG) method is very widely used for many years since it was first reported in 1993[15]. The setup of SD-FROG measurement is show in Fig.2.4, which is designed to be easily used either in the pump probe experiment. After passing through several dichroic mirror filters to remove the unwanted pump light components of FWM, the output DUV beam is first spatially separated by a half aluminum mirror. One is used as pump beam in the later work, another is attempted to be the probe beam. In the pump-probe experiment, the intensity ratio between pump and probe is adjusted to be about 8:1. This means that the probe beam intensity should be properly reduced from the ratio 1:1 after the half mirror. Here we utilize the reflection reduction of the medium surface, the inclined plane of a 90-degree prism is used as a reflection mirror on a motor-driven delay stage. This setup achieved the probe beam intensity reduced without passing through any optical medium. Avoiding the transmission through any optical component in this way is very important in such ultrashort laser

system. The total energy of the DUV pulse from the DUV system after the dichroic mirrors are 300-nJ. After the pump probe configuration, the pump and probe pulses are adjusted to be 12-nJ and 100-nJ, respectively.

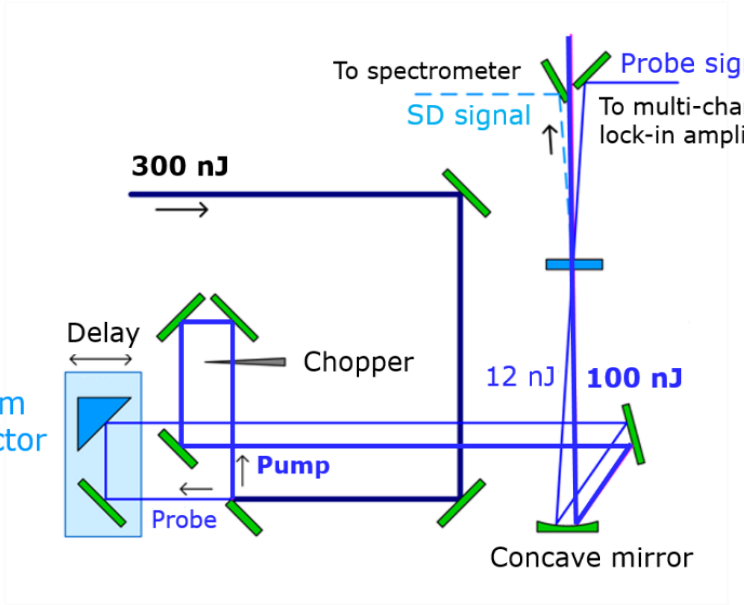

Fig.2.4 SD-FROG setup for DUV pulse measurement.

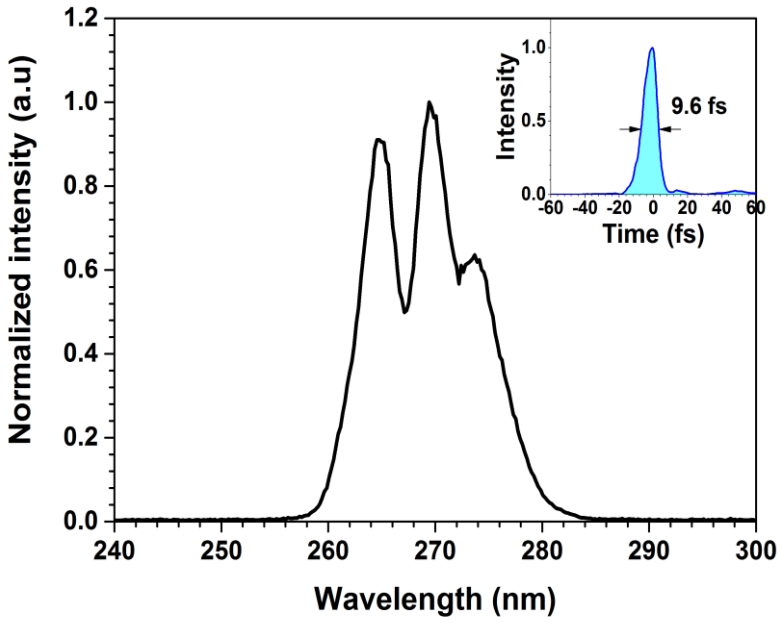

Fig.2.5 DUV laser spectrum and temporal shape of the pulse.

The characterization is performed by SD-FROG measurement with a 0.2-mm thickness CaF_2 plate as the medium. The spectrum and temporal shape of the well-

compressed DUV pulse at the sample point are shown in Fig.2.5. The spectrum is covering from 260 nm to 285 nm, with the full width at half maximum (FWHM) be about 12.8 nm. Shortest temporal FWHM of the pulse is measured to be 9.6 fs, nearly close to the transform limit, which is calculated to be 8.5 fs. Especially, to compensate the cell glass chirp which used in the actual experiment, a same thickness plate is pre-placed in front of the medium for FROG measurement. By these setup, a well-compensated pulse could be ensured for the pump-probe experiment.

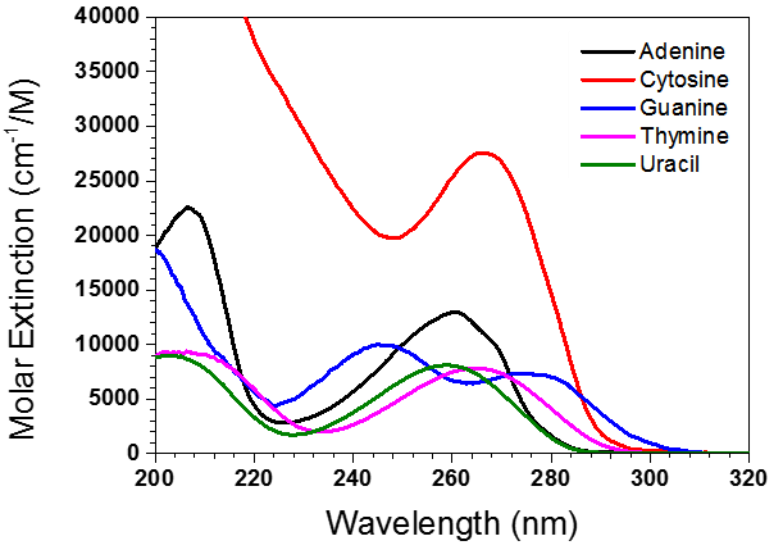

Fig.2.6 Linear absorption properties for DNA / RNA nucleobases.

With the ultra-short DUV pulses, interesting study can be performed to investigate fast dynamics in biological samples, such as DNA and RNA. Bases of DNA and RNA have strong ground-state absorption in the range of 200 ~ 300 nm (see in Fig.2.6) with an ultrashort lifetime less than 100 fs. Ultrashort DUV laser is powerful to clarify the dynamics in such systems by directly probing the dynamics after ultra-short DUV pulse excitation.

2.3.4 Stability control for the DUV laser system

Since the typical measurement time in the pump-probe experiment for time-resolved spectroscopy application is about 100 minutes, the short-time scale (several seconds) and the long-time scale (few hours) intensity stability of the laser spectrum

are both of vital importance to obtain reliable experimental data. However, the laser pulse stability in both intensity and spectrum shape factors after the propagation through a hollow fiber structure is usually not good enough for the real-time spectroscopy experiment.[16-19] Since two hollow fibers are used in this work with very small core diameter (250 μm and 140 μm), there are more sources than in a single hollow fiber case, while any kinds of fluctuation along the optical paths including the filters and optical components. The stability situation become even worse.

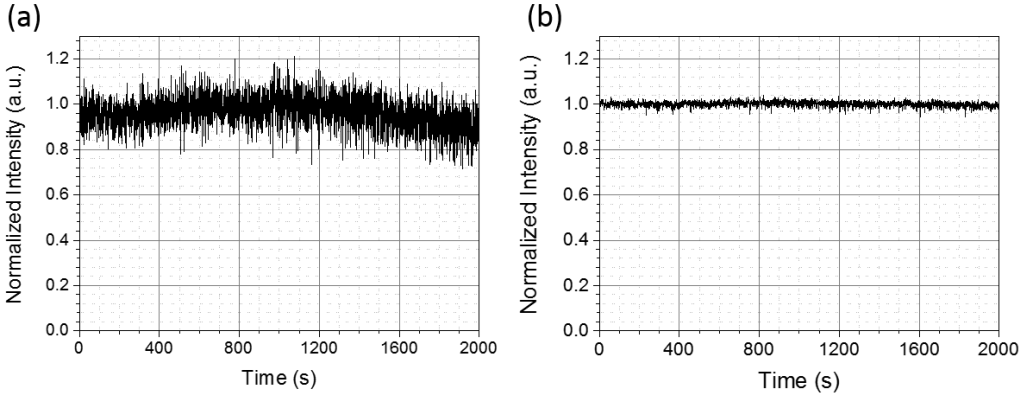

Fig. 2.7. DUV laser long-time intensity stability performance before (a) and after (b) optimization.

The most effective method to improve DUV laser stability is found to be the beam pointing stabilization. It is because that the fluctuations of laser beam pointing before the hollow fiber induce substantial variations in pulse duration, spectrum, and energy of the output pulse. By using a pointing detector for each incident beam, a feed-back signal is transmitted to the piezo controlled reflection mirror before the hollow fiber. With this feed-back signal, the beam pointing before the hollow fiber could be stabilized. To maintain the stability of the DUV pulse, three setups of the beam-pointing stabilizer are used for each input beam before focused into the hollow fiber. Details could be seen in the Fig.2.3. In the Fig.2.7 (a), the DUV output intensity is measured for more than 30 minutes without beam pointing stabilization system. The RMS noise is over 10% which is not acceptable for the pump-probe experiment application. As shown in Fig.2.7 (b), after the stabilization with feed-back signal, the DUV laser output is improved to 1.04% RMS noise level during the 30 minutes operating time.

Furthermore, the system environment is also important to the stability. Because the DUV pulse has absorption in the air which lead to the group velocity dispersion, even small air flow will give the disturbance to the output stability. Hence all the system is covered with a home-made cases to prevent air flow, especially in the area where DUV pulse propagating. The lab room temperature and humidity, are controlled to be at 20 ±0.5° C and 30 ±2 % to make sure the laser source have stable performance.

References:

1. T. Kobayashi, T. Saito, and H. Ohtani, Nature **414**(6863), 531–534 (2001).
2. T. Kobayashi, Y. Wang, Z. Wang, and I. Iwakura, Chem. Phys. Lett. **466**(1–3), 50–55 (2008).
3. T. Saito and T. Kobayashi, J. Phys. Chem. A **106**(41), 9436–9441 (2002).
4. T. Kobayashi and A. Shirakawa, J. Lumin. **87–89**(0), 119–120 (2000).
5. J. Liu, Y. Kida, T. Teramoto, and T. Kobayashi, Opt. Express **18**(5), 4664–4672 (2010).
6. R. R. Alfano and S. L. Shapiro, Phys. Rev. Lett. **24**, 584 (1970).
7. A. Couairon, A. Mysyrowicz, Physics Reports **441**, 47-189 (2007).
8. M. Kolesik, E. M. Wright, and J. V. Moloney, Optics Letters **32**(19), 2816-2818 (2007).
9. S. Backus, J. Peatross, Z. Zeek, A. Rundquist, G. Taft, M.M. Murnane, and H.C. Kapteyn, Opt. Lett. **21**, 665 (1996).
10. P. Baum, S. Lochbrunner, and E. Riedle, Appl. Phys. B: Lasers Opt. **79**, 1027 (2004).
11. F. Reiter, U. Graf, M. Schultze, W. Schweinberger, H. Schröder, N. Karpowicz, A.M. Azzeer, R. Kienberger, F. Krausz, and E. Goulielmakis, Opt. Lett. **35**, 2248 (2010).
12. H. Shen, S. Adachi, T. Horio, and T. Suzuki, Opt. Express **19**, 22637 (2011).
13. Y. Kida, J. Liu, T. Teramoto, and T. Kobayashi, Opt. Lett. **35**(11), 1807–1809 (2010).
14. T. Kobayashi and Y. Kida, Phys. Chem. Chem. Phys. **14**(18), 6200–6210 (2012).
15. K. W. Delong, R. Trebino, D. J. Kane, J. Opt. Soc. Am. B **11**(9), 1595 (1993).

16. C. E. Crespo-Hernandez, B. Cohen, and B. Kohler, Nature **436**(7054), 1141–1144 (2005).

17. P. Baum, S. Lochbrunner, and E. Riedle, Appl. Phys. B **79**(8), 1027–1032 (2004).

18. U. Graf, M. Fieß, M. Schultze, R. Kienberger, F. Krausz, and E. Goulielmakis, Opt. Express **16**(23), 18956–18963 (2008).

19. T. Kanai, A. Suda, S. Bohman, M. Kaku, S. Yamaguchi, and K. Midorikawa, Appl. Phys. Lett. **92**(6), 061106 (2008).

Chaptor 3: Deep ultraviolet pump ultrafast dynamics for uracil and thymine in aqueous

3.1 Introduction

DNA and RNA and their bases absorb deep-ultraviolet (DUV) spectrum in the sun light which may lead to photodamage.[1-5] The photo-stability of DNA under such situation is attributed to the ultrafast non-radiative relaxation dynamics of its nucleobases and the building blocks.[6] The time scale of this relaxation is known in the sub-picosecond regime resulting in the robustness of the excited state and a low fluorescence quantum yield.

Sub-picosecond electronic decays for DNA and RNA and their nucleobases have been experimentally investigated by mainly two spectroscopic methods: femtosecond pump-probe spectroscopy and fluorescence up-conversion spectroscopy.[1-10] Ultrafast photochemical dynamics, especially for thymine and uracil, have been extensively studied in recent decades.[4,7-16] In the pioneering works of Kohler's group, pump-probe experiments have been performed with a 150 fs pump pulse at 267 nm. And the probe pulses are limited within a number of wavelengths.[10,17] After the study, there have been extensive studies but the time resolution of the spectroscopy is limited by the duration of the excitation and probe pulses. Particularly in both experimental[1-10] and relevant theoretical studies[11,18], the duration of the DUV excitation pulse is about several tens of femtoseconds at the shortest, and the data obtained are very much scattered, ranging from several tens to a few hundred-fs. It has been generally understood that the main process in uracil, thymine and other bases after ultrashort pulse excitation is the internal conversion from the lowest ππ* ($^1(\pi\pi^*)$) state to the forbidden (dark) nπ* ($^1(n\pi^*)$) state. However, since the relaxation dynamics from the $^1(\pi\pi^*)$ state to the $^1(n\pi^*)$ state and then to the ground (S_0) state are so fast and the observed decay constants are scattered diversely, it is still far from the real understanding of the relaxation process. Thus, the experiments with numerous repetitions over many spectral data points after DUV pulse excitation are highly

required.

Sub-10-fs pulses in the visible spectral range can now be readily obtained, and the ultrafast dynamics in various molecules have been probed with femtosecond time resolution.[24-29] The extension of sub-10-fs spectroscopy to the DUV region is expected to help clarify the photochemical dynamics of DNA bases, as elucidated in the present study. Time resolution of better than 10-fs would also enable resolution of ultrafast electronic excited-state dynamics, which occur much faster than 100 fs, and would even provide information on real-time vibrational dynamics. Spectroscopy with sub-10-fs DUV pulses, however, has not been reported except in one paper[30] from our group, even though approaches for generating such pulses with sub 10-fs duration in DUV have been reported by several other groups.[31-36]

Recently, although experimental and theoretical research papers agree that the decay is characterized mainly by two short lifetime components that exist during the relaxation process, models of the dynamics are not consistent. It is generally agreed that the primary process in uracil, thymine, and other bases after ultrashort pulse excitation is mainly that of internal conversion from the strongly allowed lowest ππ* ($^1(\pi\pi^*)$) state to the forbidden (dark) state of the nπ* ($^1(n\pi^*)$) character. In Kohler's theory, the dynamics are explained in terms of relaxation from the $^1(\pi\pi^*)$ to the $^1(n\pi^*)$ state. Then, the subsequent relaxation is classified to be from the $^1(n\pi^*)$ state to the ground state. The short-life component shorter than 1 ps is attributed to absorption from the $^1(n\pi^*)$ state (see in Fig.3.1). In this dissertation we call this relaxation process as Model 1. More recently, several theoretical reports[19,20,21] have claimed a new model (Model 2). They discussed the possibility for relaxation from the $^1(\pi\pi^*)$ state directly to the ground state by modifying the process as follows: after photon excitation, the first relaxation path is from the $^1(\pi\pi^*)$ state to the $^1(n\pi^*)$ state. Then differently the following relaxation path to the ground state is not from the $^1(n\pi^*)$ state but directly from the $^1(\pi\pi^*)$ state. We provide a consistent description of this model in this study. Recently, Nakayama *et al.* pointed out another possibility (Model 3).[22,23] According to their theoretical calculations, the $^1(n\pi^*)$ state locates higher energy than the

$^1(\pi\pi^*)$state in aqueous solution, which indicates that the $^1(n\pi^*)$ state is not involved during the relaxation process when the $^1(\pi\pi^*)$ state is excited. The relaxation paths are assigned through two different conical intersections (CIs) from the $^1(\pi\pi^*)$ state to the ground state. However, the theoretical calculations are not yet convincing because of the difficulty in the appropriate introduction of water molecules with the base molecules into an aqueous solution. Because the evidence of two time constants relating to two CIs in the same $^1(\pi\pi^*)$ state is not yet sufficiently convincing, unless barriers exist in the $^1(\pi\pi^*)$ state to separate the two CIs, only a single time constant behavior can be indicated.

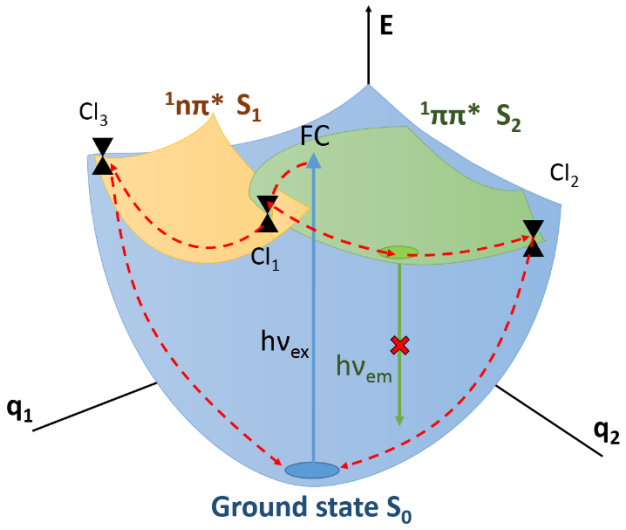

Fig.3.1 Schemes of the nonradiative decay passways of uracil and thymine.

In the last decades sub-10-fs visible pulses in the visible spectral range can be readily obtained and the ultrafast dynamics in various molecules have been probed with femtosecond time resolution.[23-28] Extending the sub-10-fs spectroscopy to the DUV region is expected to clarify the photochemical dynamics of DNA bases as elucidated in the present study. With the time resolution better than 10-fs, we would also be enable to increase the resolution of ultrafast electronic excited state dynamics. Which occurs faster than 100-fs and even provides the information on real-time vibrational dynamics. Before this work, spectroscopy with sub-10-fs DUV pulses has only reported in one paper[29] from our group, even though approaches for generating

such pulses with sub 10-fs duration in DUV have been reported from several groups.[30-35]

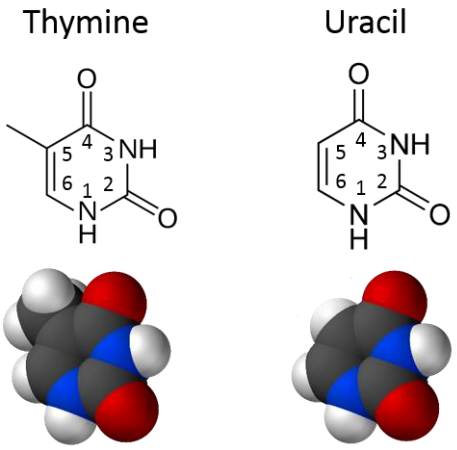

Fig.3.2 Molecule structure for thymine and uracil.

We select the two fundamental DNA / RNA nucleobases of thymine and uracil as the research targets. Thymine and uracil has very similar molecular structure (see in Fig.3.2) and be only contained in DNA and RNA respectively. The only difference in molecule structure is with or without a methyl group on the position of C_5. They are expected to have similar chemical and photochemical properties. But, it is well known that the thymine and uracil dinucleotide form different products, whereas DNA is known to have double-pair mechanisms for photodimers and other damage, only one repair mechanism has been found for RNA thus far. These results suggests that the structural difference of this single methyl group might be much more important than previously thought.[41] In the present work, an 9.6 fs DUV pulse[36,37] is taken into the application of transient absorption spectroscopy with a resolution in sub-10-fs range. Sub-10 fs time-resolved spectrum and the time dependence of the difference absorption due to relaxation of electronic transition and vibrational dynamics are obtained enabling detailed discussion on the ultrafast relaxation in aqueous solutions of uracil and thymine for the first time. The decay dynamics of the excited states and the vibrational dynamics can be investigated at the same time. Vibrational modes with frequencies up to 2500 cm^{-1} can be probed with such short pulse simultaneously.

3.2 DUV pump and DUV probe experiment

3.2.1 Experimental setup

After the DUV pulse is generated and purified by the dichroic mirrors, the polarization of the DUV pulse is horizontal. In the pump-probe experiment, the full energy pulse is going to split into pump and probe pulse for two different spread direction. In order to avoid to bring dispersion difference between the two pulses, ordinary beam splitter is not appropriate to be used here. In this work, a D-shape half mirror is used for spatial separating the input beam in horizontal plane. Therefore, the DUV beam is changed to vertical polarization by a periscope composed of aluminum mirrors first. Hereafter, the setup is made to be similar to the configuration of self-diffraction (SD) frequency-resolved-optical gating (SD-FROG) tracing, which is used to measure the characterization of the pulse shape. By optimizing the optical path length between the hollow fiber and the sample point in air, the pulse duration of the DUV pulse is compressed to be the shortest.

The transmitted probe pulse after the sample point is focused into a multi-mode fiber and guided to the detection system. Which is the combination of a multi-channel spectrometer with a multi-channel lock-in amplifier system (Signal Recovery, Model 7210, 128-channels).[19] The probe pulse is optical delayed by a pair of reflection mirrors on a motor-controlled stage (FS-1020PX, Sigma-Tech). The pump pulse is modulated with the half frequency (500 Hz) of the laser source by a mechanical chopper for the lock-in frequency reference. The pulse energies of the pump and probe are adjusted (details has been already described in Chapter 2) to be 100 nJ and 12 nJ, respectively. The absorbance change spectra are measured with a delay time step size of 0.2 fs, over the range from -200 fs to 1800 fs. After each measurement, the sample inside the cell is careful cleaned with distilled water for several times before new sample is injected, and then same procedure repeat for each measurement. All the experiments are performed at a room temperature (293 K).

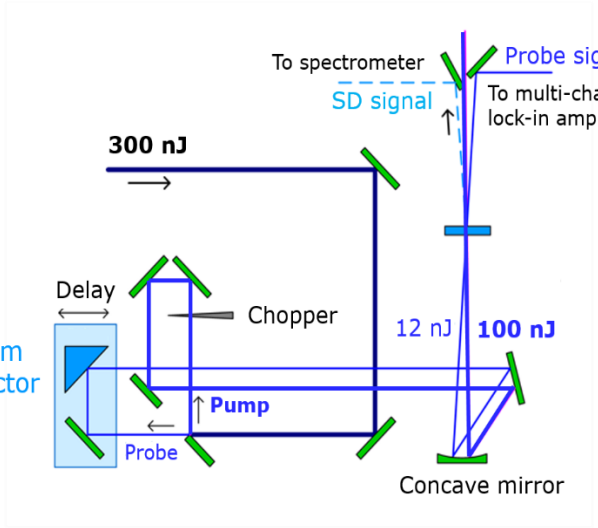

Fig.3.3 DUV pump-probe experiment setup

The pump-probe experimental setup is illustrated in Fig.3.3. The setup is compatible with SD-FROG method for pulse measurement, as the detail features described in the last Chapter. The chirped-pulse four-wave mixing (CFWM) method is more effective to compressed the DUV pulse with broadband spectrum and pulse duration down to a sub-10-fs without the introducing of an additional pulse compressor.[32,33]

3.2.2 Sample preparation

Uracil and thymine (5-methyluracil) powder (reagent grade) without further purification are purchased from Sigma Aldrich. Uracil and thymine are dissolved in distilled water with a molar concentration of 4 mM and 2 mM, respectively. The concentration of samples are prepared in this experiment by considering with two facts: First, the higher concentration simply indicated with the stronger signal which gives by the larger amount of the photon involved molecules. On the other hand, because the pump and probe laser spectrum is both located at the absorption range for these samples, higher concentration will induce weaker transmitted probe light. The lowest detectable probe intensity is limited by the resolution abilities of detection system, even though high resolution already provided by multi-channel lock-in amplifier (MLA) detection system. These two facts show different optimization directions, which need

us to find a best compromise.

The aqueous solution is circulated by a home-made sandwich-type flow cell with a peristaltic pump continuously. The flow cell is composed of two 0.2-mm-thick CaF_2 windows and an interlayer with the optical length of 0.2 mm. This short optical length could guarantee the group velocity delay effect is small for DUV pulse propagating through the sample. The pulse duration is maintained to be ultrashort. Because of the high photon energy in UV range, sample damage is easily happened, cycle system for the sample is always needed especially in the DUV range. Thin cell will introduce the unwelcoming inhomogeneous of the flowing condition due to the viscosity of solvent sample which is also relative to the sample's concentration. By the multiple considerations and experimental confirmation, current parameters are selected for the best experimental results.

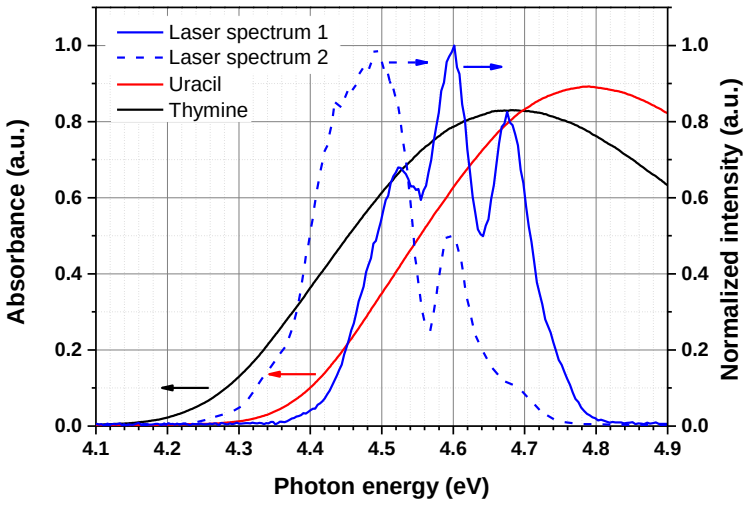

Fig.3.4 Ground state absorption for thymine and uracil with laser spectrum.

In Fig.3.4, the ground state absorption for thymine and uracil is illustrated and compared with laser spectrums. It also shows the laser spectra with two different energy distributions. These two laser spectrums are used to check out whether the pump wavelength-dependent effect exists. The excitation ranges of the former and the latter are 4.25 ~ 4.73 eV and 4.35 ~ 4.80 eV, respectively. And it is clarified from the

result that no such effect exist. The absorption spectra of uracil and thymine have peaks at 4.79 and 4.68 eV, respectively. The spectrum of the DUV pulse overlaps well with the absorption spectra of the samples in the photon energy range below 4.80 eV.

3.2.3 Experimental results

Here we would like to show the time-resolved experimental results for uracil and thymine aqueous solution by using DUV pump probe pulses, respectively. A two-dimensional time-resolved difference absorption (2DTR-ΔA) spectrum of uracil and thymine are shown in Fig.3.3 and Fig.3.4, respectively. The x-axis is the probe photon energy covered from 4.35 eV to 4.75 eV. The y-axis is the delay time between pump and probe pulses, which start from -200 fs to 1800 fs. The spectral resolution achieved by the detect system could reach to 0.3 nm, meanwhile the delay time step is accurate to 0.2 fs. The intensities of absorbance difference (ΔA) are plotted as different color with the scale bar on the right side of each figure. ΔA is a no unit parameter present the ratio of absorption change during probe beam propagation through the sample, which is already described in the Chapter 1. It is from -0.012 to 0.008 for uracil, and from -0.009 to 0.004 for thymine, while such small values are detected by the benefit of introducing multi-channel lock-in amplifier for detection. In the 2DTR-ΔA figures (we'd like to call it ΔA map also), the black lines are plotted where the ΔA equal zero. Fig.3.7 shows the 2DTR-ΔA spectrum of blank test for solvent distilled water only, it is used to check if any background signal appears in the same condition as the nucleic base samples. From Fig.3.7, it can be concluded that the distilled water sample does not have any observable positive or negative ΔA signals, except in the negative time range and at around zero delay times.

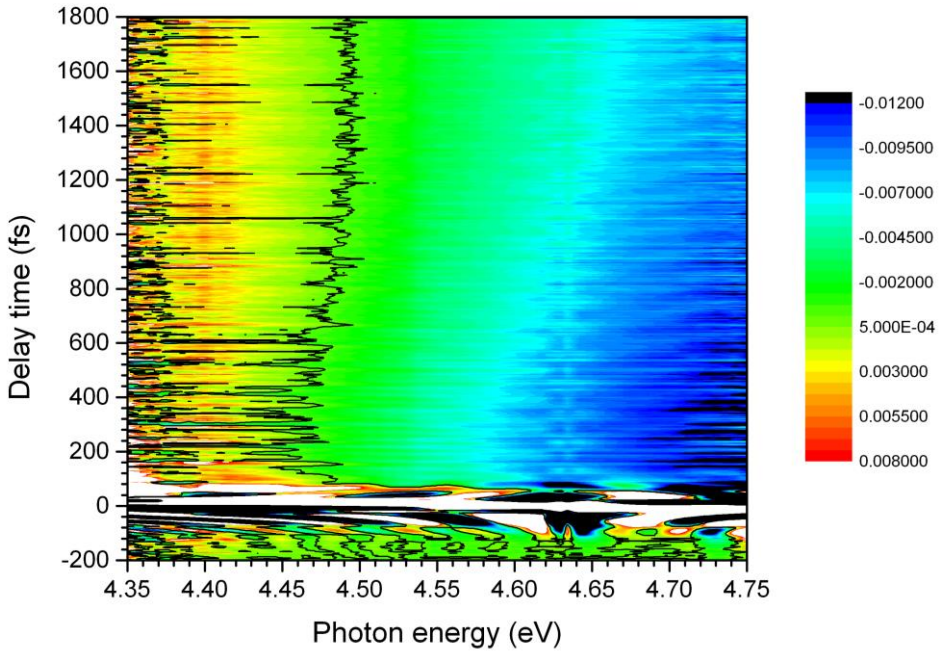

Fig.3.5 Two dimensional absorbance difference of uracil in aqueous.

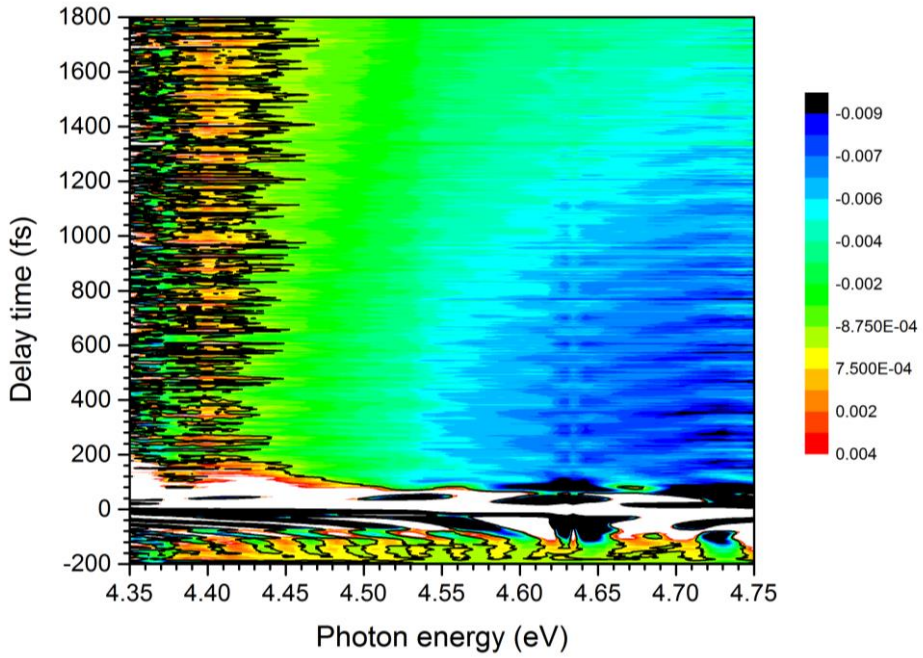

Fig.3.6 Two dimensional absorbance difference of thymine in aqueous.

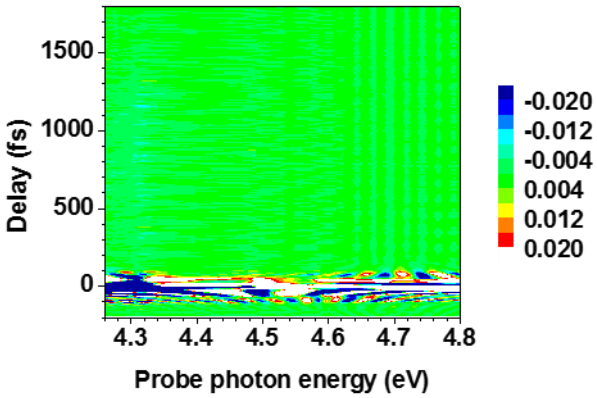

Fig.3.7 Two dimensional ΔA for distilled water sample as the blank test.

In Fig.3.8 (a), the time-resolved ΔA decay traces for uracil solvent sample are plotted by several selected probe photon energies. The large various signals at delay times of around 0 fs are observed and could also be seen for the thymine solvent and water samples, which can be seen more clearly in a difference absorbance trace obtained after averaging the whole probe photon energy range. Specifically, there are intense oscillatory structures in the delay time range between -100 fs and -60 fs, with similar structures appears for both uracil and thymine solvent samples in this delay time range. Therefore, this intense oscillatory structure is not attributable to molecules of uracil and thymine, but is considered to be mainly due to a coherent artefact, perturbed free induction decay, and interference between the scattered pump light and probe diffracted in the direction of the probe. In the range of positive delay time, ΔA signals are gradually changed along the delay time increasing. In some certain probe photon energy, small oscillations could be observed. The ΔA values are mainly negative in higher photon energy ranges and relatively increased to positive when probe photon energy is lower than 4.36 eV. The signals locate at positive delay time range apparently due to the target molecules, uracil and thymine. In the next several sections in this dissertation, the electronic decay analysis based on these observed experimental data will be made first.

And the Fast-Fourier Transformed (FFT) frequency information of ΔA (shown in Fig.3.8 (a)) for each relative probe photon energies are shown in Fig.3.8 (b). There are

several strong frequency model located at around 300 cm^{-1}, 800 cm^{-1} and 1200 cm^{-1}, which are due to the vibrational properties of uracil. These results have good agreements with the vibrations in Raman spectrum of uracil. More detailed analysis of vibrational dynamics is made later, which will be discussed in the section 3.3.4.

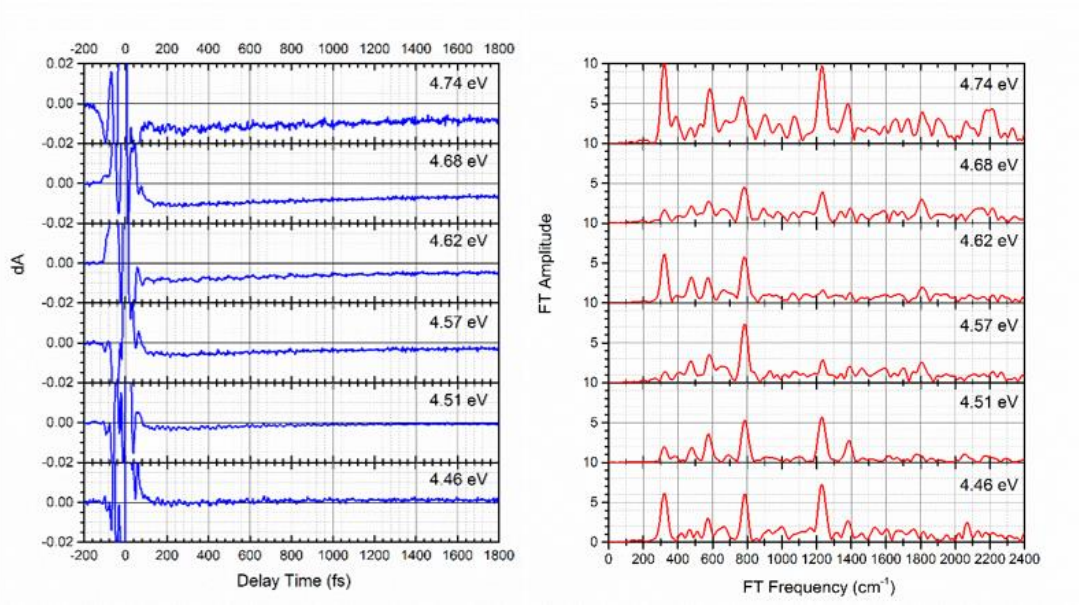

Fig.3.8 Time resolved absorbance change and the FFT frequency distribution for uracil in selected probe photon energy.

3.3 Deep ultraviolet dynamics of DNA base: uracil and thymine

Figs.3.9 (a) and (b) depict the bird-eye views of the two-dimensional time-resolved difference absorption (2DTR-ΔA) spectra of uracil (U) and thymine (T) in aqueous solutions, respectively, in the time range of 100 fs-1800 fs. They are from the same data shown in Fig.3.5 and Fig.3.6. As can be seen in the figures, the time resolved difference absorption spectra $\Delta A(\omega, t)$ for both U and T are dominated by negative values in the full spectral range of probing. The laser spectrum here used as pump and probe is mainly covering the lower energy ranges of absorption spectra of the nucleobases. Fig.3.10 (a) and (b) show relevant 2D Fourier transformed amplitude spectra the 2D-ΔA data in Fig.3.9 (a) and (b), respectively, calculated from the delay time range of 60-1800 fs. Gives a comprehensive and intuitive vibrational information about the excited state in uracil and thymine, respectively. Detail discussions are made in the following

sections.

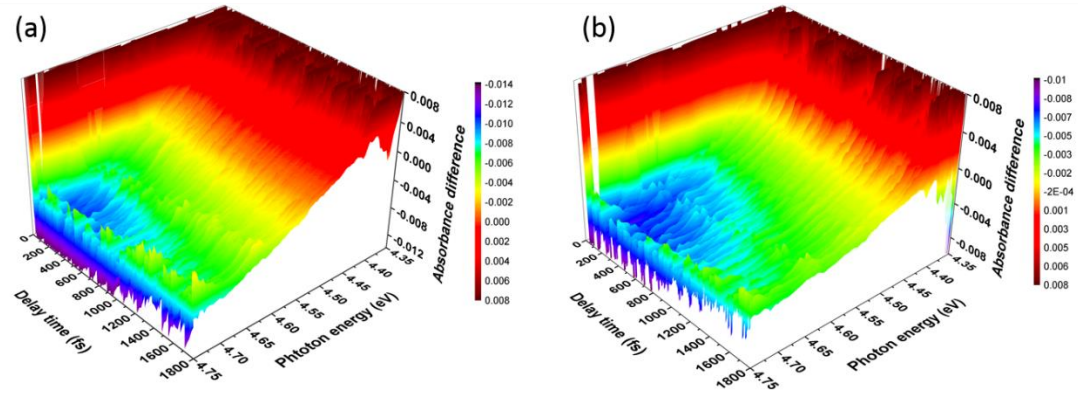

Fig.3.9 3D display of ΔA of uracil (a) and thymine (b) aqueous solutions

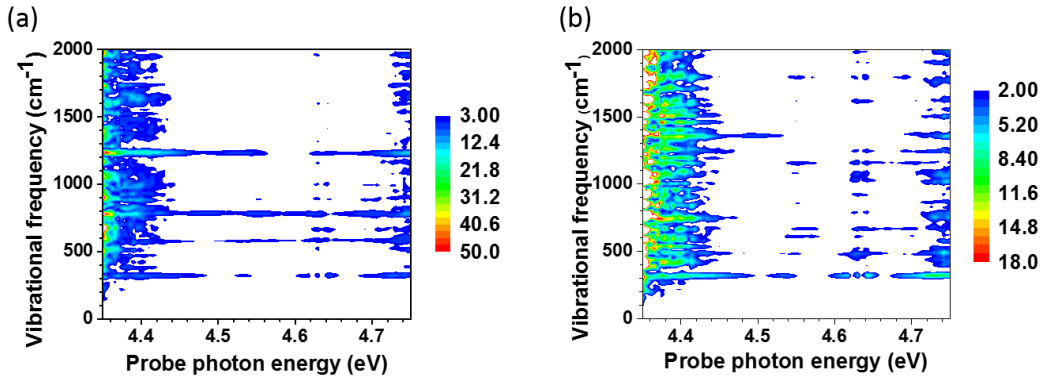

Fig.3.10 Fourier spectra of uracil (a) and thymine (b), respectively, calculated from the traces in Fig.3.9 (a) and (b), over the time range of 60-1800 fs.

3.3.1 Assignment of the difference absorption spectra

First, we discuss the main global feature of the time-resolved spectra of uracil and thymine shown in Fig.3.11 (a) and (b), respectively. They are plotted for the delay time range between 100 fs and 1800 fs with a 100 fs step. The spectra are obtained by averaging the ΔA values over ± 50 fs around the center delay times from the 2D-ΔA data for uracil and thymine, respectively. Because the inhomogeneous broadening is considered to be small in the absorption spectra of the molecules in solution, the spectral shift in the time-resolved difference absorption spectrum $\Delta A(\omega, t)$ is considered not to be mainly due to the relaxation among inhomogeneous broadening groups. Another feature of the time-resolved spectra in Fig.3.11 (a) and (b) is that the zero crossing point is shifting during all of the probe delay times from 60 fs to 1800 fs.

The isosbestic point is also absent in both uracil and thymine, whereas both the induced absorption (ΔA>0) and the bleaching (BL) (ΔA<0) and stimulated emission (SE) (ΔA<0) are contributing to the signals.

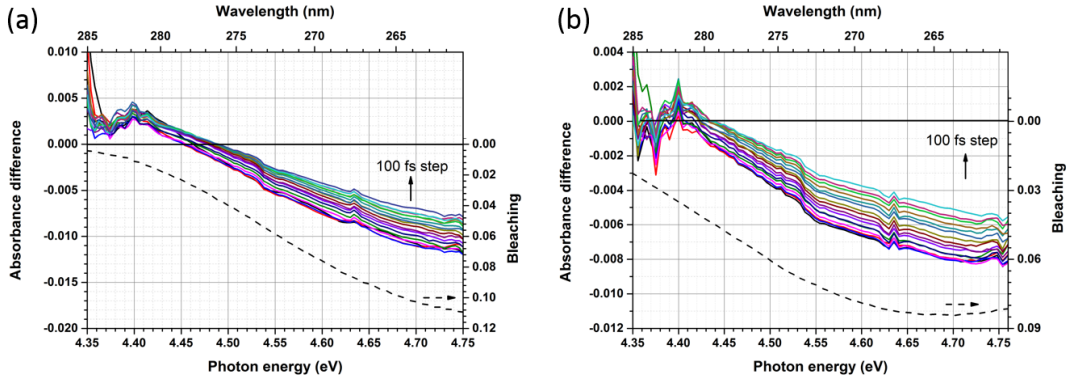

Fig.3.11 The time resolved difference absorbance spectra for the uracil (a) and thymine (b) samples.

The absence of the isosbestic point and the zero-point shift means that at least one of the positive and negative signals of ΔA are shifting in energy during the decay because for the time-resolved spectra, even in the shorter time range below 100 fs, there is no clear hole in the spectrum with a structured ΔA corresponding to the DUV laser spectral structure. This also indicates a homogeneous width of the systems that is larger than the structural features of the laser spectrum, which is estimated as 50 meV from Fig3.4. The BL spectra are broad and featureless, reproducing the shape of the absorption spectra in the smaller energy range below 4.45 eV in both uracil and thymine. Therefore, it can be considered that the shift in the BL spectra is not sufficient to explain the probe photon energy dependence of the shortest and the second shortest lifetime components. From this discussion, we conclude that the spectral changes in Fig.3.11 (a) and (b) are not due to the change in the BL spectra. Furthermore, the spectral shift is in the direction of a blue shift. Induced emission is always expected to shift to red because the population in the ground state corresponds to the Franck-Condon state, and the emission is always red-shifted from the absorption and relaxation taking place in the excited state, which always results in a further red shift. From the above discussion, the spectral shift observed is concluded not to be due

to the shift of the BL spectrum of absorption or to that of SE, but is due to the shift of the induced absorption spectrum.

On the other hand, the fluorescence spectra of uracil and thymine cannot be directly measured by conventional fluorimeter due to their extremely low efficiencies induced by an ultrashort lifetime. Because the molecular extinction coefficients of the $^1(\pi\pi^*)$ state are relatively large (1235 and 1359 M^{-1} cm^{-1} for the absorption peak in uracil and thymine, respectively), the peaks of the SE are expected to be located at the minor image positions within the absorption spectra. Assuming the location of the 0-0 transition to be at 4.40 eV, it is expected that the SE will appear in the photon energy range of 4.4 ~ 3.8 eV for uracil and 4.3 ~ 3.7 eV for thymine. Then, the probe spectrum seems not to overlap with the fluorescence spectra. Therefore, the difference absorption is mainly due to BL induced by the ground state depletion and not due to the SE in the observed spectral range of the negative ΔA signal. By comparing the stationary absorption spectrum of uracil and the pump laser spectrum, it is known that the pump laser excitation is covering a 0 - 0 transition. The amount of depletion of the ground state is estimated from the overlap between the distribution of the pump laser intensity spectrum and the absorbance spectrum of the uracil. The fraction of species in the excited state by the pump is calculated to be 17 ~ 20% of the total ground state population. Using this value including the errors, we calculate the induced absorption spectrum and the BL spectrum as shown in Fig.3.11.

3.3.2 Probe photon energy dependence of lifetimes

The lifetime information can be extracted from the 2DTR difference absorption spectra $\Delta A(\omega, t)$, by global fitting the traces at all the probe photon energy points with the following fitting function. This in principle allows for three separated species, $\Delta A_1(\omega)$, $\Delta A_2(\omega)$, and $\Delta A_3(\omega)$, and two corresponding time constants, τ_1 and τ_2 (where $\tau_1 < \tau_2$) to $\Delta A_1(\omega)$ and $\Delta A_2(\omega)$. $\Delta A_3(\omega)$ component is assumed to have much longer decay time than the delay range (from -200 fs to 1.8 ps).

$$\Delta A(\omega, t) = \Delta A_1(\omega) \exp(-t/\tau_1) + \Delta A_2(\omega) \exp(-t/\tau_2) + \Delta A_3(\omega) \quad (3.1)$$

Here ω is the angular frequency of the spectral component in the probe pulse. In this equation, the assignment of the exponential coefficients is depend on whether the sequential model or parallel model is used, which is discussed as below. The above equation is based on a parallel decay scheme after fast relaxation. If the relaxation is in the scheme of serial mechanism, then the coefficients, $\Delta A_1(\omega)$, $\Delta A_2(\omega)$, and $\Delta A_3(\omega)$ are to be used to get the spectral information of the sequential species. The lifetimes are determined for uracil and thymine and shown in Figs.3.12 (a) and (b), respectively. The lifetimes are not constant but are sensitively dependent on the probe photon energy (ω) for both the short and long lifetimes for uracil and thymine. Even though the lifetime components are nominated short- and long-life species, the lifetime (< 1.64 ps for uracil and < 2.51 ps for thymine) of the longer one is still much shorter than that of many other organic molecules. The lifetimes for both uracil and thymine are called hereafter the shortest $\tau_1(\hbar\omega)$ and second shortest $\tau_2(\hbar\omega)$ components obtained by the two-exponential fitting with a residual much longer life component are determined. These highly probe-photon energy dependent short decay times can possibly be the reason of the highly scattering values of the previously reported data.[1-10]

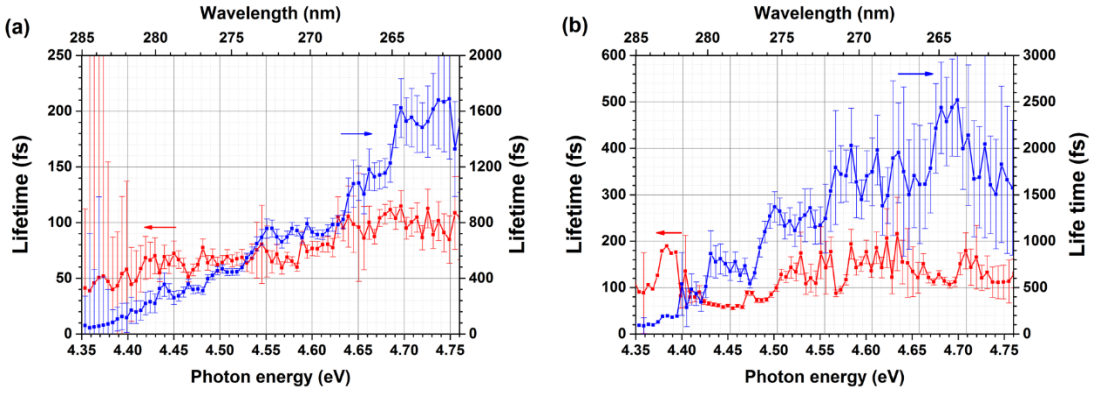

Fig.3.12 The probe photon energy dependence of decay times of τ_1 and τ_2 of the time-resolved absorbance changes for uracil (a) and thymine (b) sample solutions in aqueous solutions.

The excitation with the sub-10-fs DUV pulse instantaneously depletes the ground-state population by excitation of molecules in the ground state selectively to the second lowest excited singlet state with $\pi\pi^*$ character due to the highly allowed transition probability as it has been well established in most of the recent papers that the initially

excited state is the $^1(\pi\pi^*)$ state from which relaxation takes place to decay to the $^1(n\pi^*)$ state.[10,17] The time-resolved spectrum shows strong BL just after the excitation, and it relaxes rapidly with a non-constant lifetime. The shortest decay time $\tau_1(\hbar\omega)$ is dependent on the probe photon energy and varies from about 54 fs to 128 fs in uracil and from about 68 fs to 151 fs in thymine in the probe range of 4.35 ~ 4.76 eV. The second shortest decay time is also highly dependent on the probe photon energy extending from 110 fs to 1640 fs in uracil and 130 fs to 2210 fs in thymine in the same energy range. The decay rates of the longer-life components thus decrease by the factors of 14.7 in uracil and 17.2 in thymine when the probe photon energy is increased from 4.35 eV to 4.76 eV. This observation can explain the even longer time "constant" of the widely scattered values of lifetimes τ_1 and τ_2 reported in the literature[3,7,9,17] because it is not meaningful to refer to a "time constant" in a system in which spectral shifting is taking place. The differences among the lifetimes varying widely in the literature are strongly suggested to be due to variations in the pump and/or probe photon energy. It has been well known from a decade ago[4,8,10,14] that the lifetimes of both τ_1 and τ_2 are unusually short, in the range of 100 fs to a few picoseconds. They are much shorter than common aromatic molecules with lifetimes of nanoseconds, and the surprisingly short lifetime τ_1 in both uracil and thymine and also in other nucleobases has attracted the attention of many scientists and has been argued extensively.[2]

In such a system with widely changing lifetimes, it can be concluded that the simple model of these states molds with the static lifetime of the shortest (τ_1), the second shortest (τ_2), and the long component (which is much longer than the 2 ps of the probe delay time range in the present experiment) and is inadequate to describe the decay dynamics properly. A wide range of wavelength-dependent lifetimes has also been observed for nucleic acids in many previous studies.[1-10,17] However, in all of those studies, the number of probe wavelengths was very limited. The highly probe photon energy-dependent short decay times we observed may be the reason for the largely scattered and sometimes inconsistent values of the lifetimes among these works.[1-10,17]

Hereafter, we refer to the plot of the lifetime of probe photon energy dependence

as a lifetime spectrum. In the lifetime spectrum of uracil, the two lifetimes $\tau_1(\hbar\omega)$ and $\tau_2(\hbar\omega)$ both increase nearly monotonically as the probe photon energy increases from 4.35 eV to 4.75 eV. The most supported mechanism of the very short lifetime in uracil and other base molecules in aqueous solution is that of the conical interaction (CI). In the following subsection, the peculiar features of the probe photon energy of the lifetimes are discussed in terms of the CI relaxation mechanism.

3.3.3 Relaxation processes though the conical intersection

The shortest value of lifetime in the $\tau_1(\hbar\omega)$ spectrum is about 50 fs, which is much shorter than the vibrational relaxation and internal conversion in an ordinary molecule, and it is 54 ± 9 fs in the lower photon energy region of 4.35 ~ 4.45 eV in uracil and 68 ± 10 fs in the 4.40 ~ 4.47 eV range in thymine. In the most accepted theoretical model, after leaving the Franck-Condon state, the strongly allowed $^1(\pi\pi^*)$ state (S_2) is considered to be very close to the CI and relaxes rapidly through the CI to the $^1(n\pi^*)$ state (S_1), the CI here is marked as CI(S_2-S_1).

Because the pump laser excites the energy range of the 0-0 transition of the lowest allowed transition and the Franck-Condon peak, the following relaxation dynamics are expected to take place (following the Model 2 which described in section 3.1). If there is no contribution from the nπ* state, then the dynamics observed in the shortest time scale of several tens of femtoseconds is considered purely due to CI(S_2-S_1) in the S_2 state, which could have ultrafast population dynamics, but is not due to that in the ground state. Therefore, the ultrafast relaxation of 50 fs is the time required for the internal conversion passing through the CI(S_2-S_1) point. Then, the higher energy range signal corresponding to the population above the CI(S_2-S_1) point relaxes by vibronic coupling and vibrational relaxation impeded by the loss of population through the CI(S_2-S_1) leaky hole. The dynamics having probe photon energy-dependent decay times corresponding to the different initial positions on the potential curve.

The second shortest lifetime component $\tau_2(\hbar\omega)$ is dependent on the probe photon energy in the ranges of 110 ~ 1640 fs for uracil and 130 ~ 2210 fs for thymine.

Previously, this slightly faster decay rate is considered to be due to the combined (larger) contribution of thermal relaxation and the (effectively smaller) contribution of the very efficient CI process.[1,4,10,17] However, the observed probe photon energy dependence of $\tau_2(\hbar\omega)$ is difficult to explain in terms of thermal relaxation for the following reasons.

(1) The difference between about 110 fs and 1.6 ps of the decay probed at 4.35 eV and 4.76 eV, respectively, is too large.

(2) The relaxation time range of 0.11~1.6 ps is too short for it to be assigned to the thermalization process.

Usually, thermalization in organic materials is a condensed phase that takes place in the time range of 5 ~ 10 ps. Kohler and others explained the short lifetime corresponding to τ_2 in terms of energy release to the solvent water through hydrogen bonding (Model 1).[1,4,10,17] However, this is not the case here because the lifetimes in the gas phase lacking the hydrogen bond are also very short. Also, the lifetimes for other molecules with nitrogen in the hexagonal ring in water solution are not expected to be shorter than 2 ps.

Therefore in this work, this second shortest lifetime $\tau_2(\hbar\omega)$ is considered to be mainly due to ultrafast relaxation through CI from the $^1(\pi\pi^*)$ to the ground state (Model 2) before thermalization, which is considered to take place in the range of longer than a nanosecond[39,40] in many aza-aromatic molecules. The depopulation of the $^1(\pi\pi^*)$ state after photo-induced population starts to take place by leakage of population to the $^1(n\pi^*)$ state. Because the molecular structure in both uracil and thymine is deformed after excitation to the $^1(\pi\pi^*)$ state by the ring puckering and / or C_5=C_6 bond twisting,[18-22] the stabilization is expected to be large enough for the $^1(\pi\pi^*)$ state to be lower than the $^1(n\pi^*)$ state. Then the transition probability from the ground state to the initially allowed $^1(\pi\pi^*)$ state is reduced, which is substantially due to the very large reduction of the Franck-Condon factor. We call this the deformed state (S_{2d}) after the geometrical relaxation along the coordinate, and the relative CI is marked as CI(S_{2d}-

S_0). As described before, the negative signal ΔA of the pump probe experiment is considered to be mainly due to the depletion of the ground state. This depletion is not recovered until 2-ps decay time. Therefore, the decay dynamics are purely due to the ground state population dynamic induced by the depopulation and recovery of the state. The repopulation takes place at first in the high energy range of the ground-state thermal population because the relaxation is expected to proceed via a vibrational ladder descending in the ground state. Then around 1.6 ps after excitation (uracil case), the full repopulation comes closer to the equilibrium population distribution even though full thermalization may take place at a time longer than 3 ~ 5 ps, as is the case in ordinary aromatic molecules of similar size to that of uracil and thymine. The reasons for the faster increase in lifetime explained in terms of rate (= 1 / lifetime) are as follows.

(1) The rate of $(200\ fs)^{-1}$ decreases by half to $(400\ fs)^{-1}$ from 4.35 eV to 4.50 eV (0.15 eV energy difference), then decreases to $(800\ fs)^{-1}$ at 4.65 eV (the same 0.15 eV difference), and further decreases to $(1600\ fs)^{-1}$ at 4.76 eV (about the similar difference of 0.11 eV).

(2) The even smaller wavelength dependence of the rate at longer delay is because as it comes closer to equilibrium, the contribution of a spectral-diffusion-type diffusive process, which includes reversal of direction, begins to be involved, resulting in the effective slower rate.

Here we would like use the scheme shown in Fig.3.13. After being excited from the S_0 state to the S_2 $^1(\pi\pi^*)$ state, ultrafast decay through CI(S_2-S_1) to the S_1 $^1(n\pi^*)$ state. Then the rest population in the deformed S_{2d} state fast decay through CI(S_{2d}-S_0) to the S_0 state. The shapes of potential carves of S_2 and S_1 are assumed to be parabolic, along a local coordinate *q*. This coordinate couples most strongly between the ground state S_0 and S_2 state.

$$E_{\pi\pi^*}(q) = a_2\left(q - q_2\right)^2 + E_{\pi\pi^*(\min)} \tag{3.3}$$

$$E_{n\pi^*}(q) = a_1(q - q_1)^2 + E_{n\pi^*(\min)} \tag{3.4}$$

$$E_{(\pi\pi^*)^d}(q) = a_{2d}(q - q_{2d})^2 + E_{(\pi\pi^*)^d(\min)} \tag{3.5}$$

$$E_g(q) = a_0(q - q_0)^2 + E_{g(\min)} \tag{3.6}$$

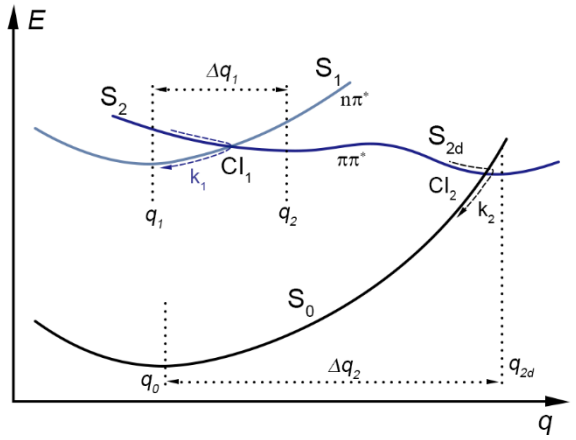

Fig.3.13 The scheme of relaxation process through CIs.

We focus on the relaxation through CI(S_2-S_1) first. In general, the relaxation from S_2 to S_1 is assumed to take place mainly along the coordinate q. The assumption is that the relaxation is very fast (< 100 fs), so the time of vibrational mode coupling does not have time to substantially proceed. Therefore, the coordinate in Eq. (3.3) is same as that in Eq. (3.4). In this case we can assume that the a_1 and a_2 corresponding to the spring constants do not change much because of they belong to the same mode. Then, at the crossing point CI, the energy difference between the two potential curves will be given as follows using $a_1 \approx a_2 = a$.

$$\Delta E = \left|E_{\pi\pi^*}(q) - E_{n\pi^*}(q)\right| = \left|-a\Delta q_1(2q - q_1 - q_2) + E_c\right| \tag{3.7}$$

Here E_c is the energy deference of potential curve minimum to ground state between S_2 and S_1, which is a static parameter. In Eq. (3.7), all the parameters are static except q when the specific environment is determined. Therefore, the energy difference around CI is determined by the coordinate factor. We define the photon energy dependent leakage rate $k(E)$ through the CI, with expectation to satisfy the following equation by the mechanism of tunneling,

$$k(E) = k(_{E=E_0})e^{-\left|\frac{E-E_0}{\Delta E}\right|} \equiv k_0 e^{-\left|\frac{E-E_0}{\Delta E}\right|} \quad (3.8)$$

Here E is the probe photon energy, E_0 means the central energy of CI position, and the ΔE is the half width at 1/e of energy separation function between the relevant two potential curves around the CI. From the lifetime spectra the tunneling rate through the CI(S_2-S_1) point in both uracil and thymine can be estimated to be of the order of 1 × 10^{13} s^{-1}. By global fitting with function Eq. (3.8) to the decay rate data shown in Fig.3.14 (a), we obtain the values of E_0 and ΔE to be 4.33 eV and 0.21 eV for uracil, respectively. To our knowledge, this is the first time to obtain CI location and width experimentally.

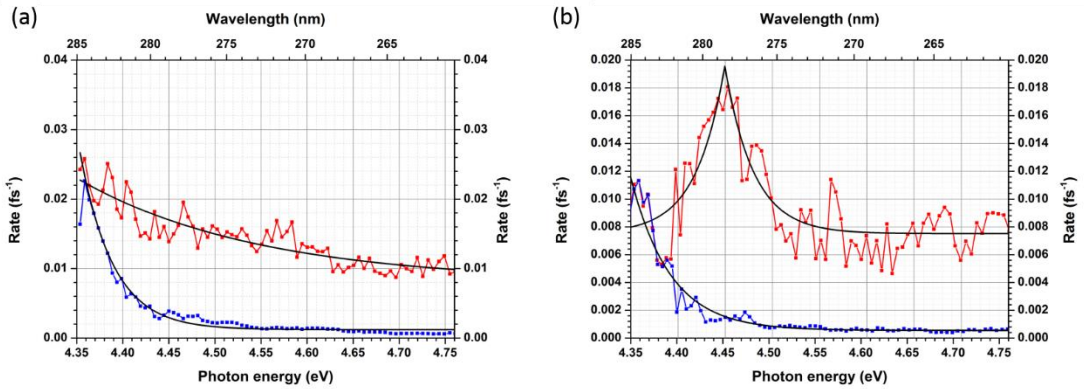

Fig.3.14 The fitted CI potential from experimental results for uracil (a) and thymine (b).

Noticeable from this result, the CI central point is considered to be lower but close the 0-0 transition. Considering the limited lowest probe energy is 4.35 eV, it is difficult to assert the CI is located at such position. But the roughly position still be confirmable with confidence. Therefore the location of lowest CI(S_2-S_1) is around and a little be lower than the 0-0 transition at 4.40 eV with the width be 0.21 eV. In the same way, we could also locate the CI in thymine molecule for the first time. Similarly to uracil, the CI(S_2-S_1) in thymine is indicated to be at 4.45 eV in Fig.3.14 (b), and it is clearly narrower (0.05 eV width) than uracil case.

Similarly, the CI(S_{2d}-S_0) position is obtained to have a center at ≤4.36 eV with width of 0.038 eV from the second shortest lifetime spectrum of uracil, and ≤4.36 eV, 0.031 eV, respectively, for thymine. In Table I, we compared the theoretical

calculation[20,21] and our experimental results with the expectation values of the potential surfaces crossing angles around CIs. Table I describes the slope difference (SD) between S_2 and S_1, and between S_2d and S_0 around corresponding CI, obtained from the paper Ref. 21 for U and T, from Ref. 20 for U. Although the absolute values varies for different calculations, but the ratio between CIs from same calculation condition could be comparable. The calculated data for SD(S_2-S_1) are larger than that for SD(S_{2d}-S_0) in both U and T. Noticeably, our experiment results are consistent with the theoretical results in Ref. 21 by the ratio being larger for uracil than thymine as in Table I. Which indicate that the model of CIs locating from $^1(\pi\pi^*)$ state to $^1(n\pi^*)$ state and ground state respectively may be more reliable, compared to the Nakayama's[21,22] model mentioned in the introduction section. In case of the model, the slope difference as large as 2 is involved. However as far as the information obtained from the calculation results in their paper, there is no proper explanation for the large slope difference between CIs, which involved in the same two states.

Table I. Comparison of theoretical calculation[20, 21] and experimental result in this work with the expectation values of potential surface crossing angles around CI.

Potential profiles along LICC path (U / T)	SD $_{(S2-S1)}$ (eV / bohr· amu$^{1/2}$)[a]	SD$_{(S2d-S0)}$ (eV / bohr· amu$^{1/2}$)[a]	R= SD $_{(S2-S1)}$ /SD$_{(S2d-S0)}$	R(U)/R(T)
Ref. 19[b] (U)	0.799	0.685	1.166	4.74
Ref. 19[c] (U)	0.670	0.717	0.934	3.80
Ref. 20[d] (U)	0.351	1.186	0.296	1.20
Ref. 20[d] (T)	0.153	0.621	0.246	1
ΔE (U)	0.21/(q/2)	0.038/(q/2)	5.526	3.43
ΔE (T)	0.05/(q/2)	0.031/(q/2)	1.613	1

[a]: SD (Slope difference around CI); [b, c, d]: Calculation method of CASSCF(10,8), MRCI-SD(6,5), MS-CASPT2(12,9), respectively.

The above assignments of the electronic states are also supported by the time-resolved vibrational information obtained from the real-time vibrational spectroscopy performed for the first time in the present study. Details of the vibrational information are discussed later.

3.3.4 Vibrational dynamics in the DNA bases

As described before, the decay times $\tau_1(\hbar\omega)$ and $\tau_2(\hbar\omega)$ are considered to correspond to the relaxation processes from the second lowest singlet $^1(\pi\pi^*)$ excited (S_2) state to the lowest $^1(n\pi^*)$ excited (S_1) state and the following relaxation process from the deformed $^1(\pi\pi^*)$ state to the ground (S_0) state. The apparent "lifetime" is a phenomenological time "constant," which includes both the spectral shift (see Fig.3.11 (a) and (b)) and the population decay of the relevant excited state. This can also be clearly seen from the time dependence of the spectral first moments of the time-resolved difference absorption spectra integrated over 4.51 eV and 4.75 eV, respectively, for uracil and thymine (Fig.3.15 (a)).

Fig.3.15 (a) and (b) shows the first moments E_{mom} of the transition spectra calculated for uracil and thymine, by using the following fitting equation, the relaxation time of the moment is determined as 918 ± 72 fs for uracil and 1226 ± 29 fs for thymine, which agrees with the electron decay time τ_2 as previously mentioned.

$$E_{mom}(t_d) = (E_{mom}(0) - E_{mom}(\infty))\exp(-t_d/\tau_{ele}) + E_{mom}(\infty) \tag{3.9}$$

Here $E_{mom}(0)$ is the initial at zero gate delay time t_d for the Fourier integration, $E_{mom}(\infty)$ is the final first moment at the longest delay time. They are showing the following relaxation due to electronic relaxation and dynamics coupled modulation due to the molecular vibration.

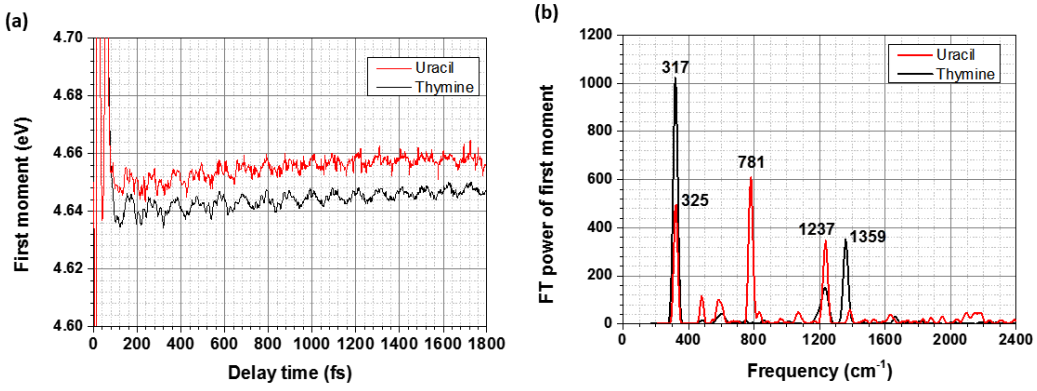

Fig.3.15 First moment from 4.51 to 4.75 eV and the FFT spectrum of it for the uracil and thymine.

The frequencies of vibrational modes coupled to the electronic relaxation within relaxation process in uracil and thymine are obtained by the fast Fourier transform after subtracting the electronic first moment is subtracted and they are shown in Fig.3.15 (b).

To investigate the more detailed vibrational dynamics, the obtained difference absorbance traces are analyzed by spectrogram analysis (details of the spectrogram calculation see in Appendix I).[22,42,43] The gating time window used here is a Blackman function window with a full width of 600 fs (FWHM width is 240 fs), which is selected based on the consideration of tradeoff the frequency resolutions and the time resolution. Therefore, the window is selected to be the longest duration as possible, but be limited by avoiding the loss of the information on the instantaneous frequency change.

3.3.4.1 Spectrogram for Uracil

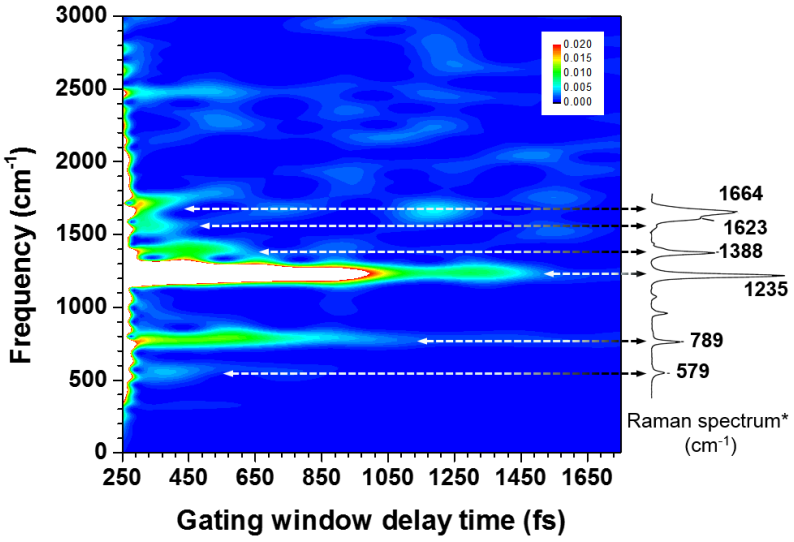

Fig.3.16 Spectrogram for uracil in the range from 4.45eV to 4.54eV

In case of the measurement signal noise ratio in uracil sample is much better than thymine. We would like to use the data of uracil as the analysis source. In Fig.3.16 shows the spectrogram calculated from the integrated real-time traces of ΔA in the probe photon energy range from 4.45 to 4.54 eV of uracil 2DTR-ΔA data. In the right

part of the figure, there is a compared resonance Raman spectrum from the literature.[44] As we can see, the agreement is obviously both in frequency and intensity. The most intense vibration is 1235 cm^{-1}, the second one is 789 cm^{-1}. Beside the above feature, spectrogram analysis provide the vibration dephasing information from the result. From spectrogram result, the most intense two modes have large lifetime about 1.2 ps. Compared to other un-intense mode, the dephasing lifetime is shorter than 400 fs. Because the gate window here used is 600 fs, the real vibrational dephasing time of these modes could be estimated as around 100 fs. More detailed value is determined in the next subsection in a further. These short vibrational dephasing times are corresponding to the shortest electronic decay lifetime component discussed in the last sections.

3.3.4.2 Spectrogram simulation for uracil on vibration around 1200 cm^{-1}

To understand more accurate values of dephasing times for each vibrational frequencies, the spectrogram analysis are applied to the experimental result and two simulated ΔA real time traces based on two different models (Model A and B). The Model A is the assumption when vibration models are independently decaying; and for Model B is the assumption of one vibrational frequency continuously chirping to another frequency during the dephasing decay. In the Fig.3.15, three spectrogram results of experimental, Model A and Model B are shown in (a), (b), (c) respectively. The gate function used here is still the Blackman window with the full width of 600 fs, this time we mainly focus on the vibrational frequencies around the most intense 1235 cm^{-1} mode. For the precisely simulations of Model A, the vibrated ΔA time traces with dephasing lifetime (τ_i) dependences of the different frequency components ω_i around 1380 cm^{-1} (i = 1), 1235 cm^{-1} (i = 2), and 1100 cm^{-1} (i = 3) are constructed with the following equation.

$$\Delta A = A_1 e^{-t/\tau_1}\cos(\omega_1 t + \varphi_1) + A_2(e^{-t/\tau_{2d}} - e^{-t/\tau_{2u}})\cos(\omega_2 t + \varphi_2) + A_3 e^{-t/\tau_3}\cos(\omega_3 t + \varphi_3) \quad (3.10)$$

Here the A_i and φ_i are the amplitudes and initial phases of each vibrational frequency. Especially for the 1235 cm^{-1} mode, there are two parameter of time rely to the rising (τ_{2u}) and decaying (τ_{2d}) behaviors. Because of the absent of 1235 cm^{-1} mode from the initial gating time, the intensity of this mode is risen at first and decayed (seen in the Fig.3.17 (a)).

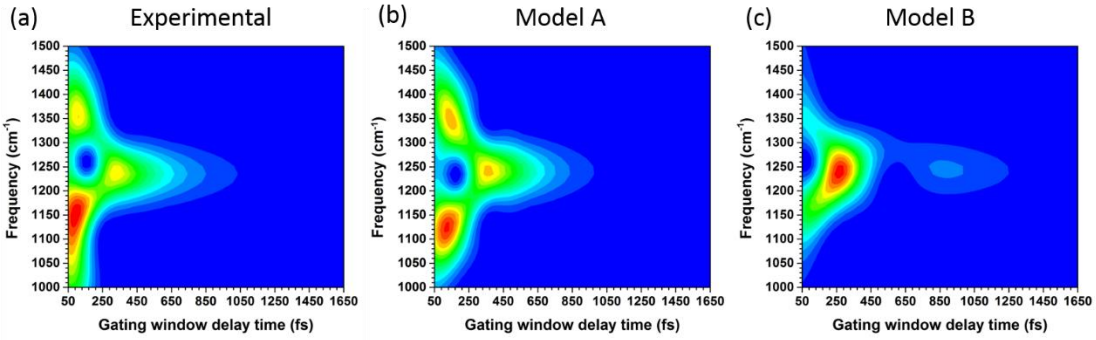

Fig.3.17 Spectrogram analysis for experimental data and simulated ΔA traces by using Model A and B.

And for the simulation Model B, the feature of 1235 cm^{-1} mode is considered to be due to the vibrational frequency shifting from the 1380 cm^{-1} or 1100 cm^{-1} modes. Therefore, moreover complicate vibrational chirping conditions are included with the new parameters (chirping time τ_{ci}), details are shown in the following:

$$\Delta A = A_1 e^{-\frac{t}{\tau_1}} \cos\left((\omega_1 \pm \Delta\omega_{12} e^{-\frac{t}{\tau_{c1}}})t + \varphi_1\right) + A_3 e^{-\frac{t}{\tau_3}} \cos\left((\omega_3 \pm \Delta\omega_{23} e^{-\frac{t}{\tau_{c3}}})t + \varphi_3\right) \quad (3.11)$$

By selecting appropriate values for the relative parameters, the best fitting of each Model A and B are shown in Fig.3.17. Compared to experimental result, it clearly shows the vibrational change can be explained by the Model A, representing the better result of spectrogram calculation than using Model B.

From simulated spectrogram of Model A, a good agreement could be made when the fitting parameters are set to be 50 fs (50 fs, 530 fs for the 1235 cm^{-1} mode) in the fitting equations. Therefore, the decay time constant of τ_{vib} = 50 fs is considered to be the vibrational phase relaxation time. This lifetime is nearly in agreement with the first electronic population decay time of S_2 state. Since the vibrational population of

the vibrational levels of the mode coupled to the electronic state S_2 disappear in accordance with the electronic population decreases. The phase decay rate is sum of the vibrational population decay rate and pure dephasing rate. The contribution of the inhomogeneous dephasing is very small (<100 fs) in such molecules in water solution while it is several picoseconds in ordinary molecules. Therefore, the acquired vibrational phase relaxation time is mainly controlled by the electronic decay of S_2 $^1(\pi\pi^*)$ state. The vibrational decay rate $(T_2^{vib})^{-1}$ is given by the sum of the vibrational population decay $(T_1^{vib})^{-1}$ which is equal to the electronic population decay of $(50\ fs)^{-1}$.

3.3.5 An attempt for DUV pump and visible probe experiment

As the degenerate pump probe experiment, the acquired information is limited by the probe photon spectrum range. And the results are mainly dominated by the negative ΔA which may rely to the combination efforts of stimulate emission and bleaching. However, more information may be obtained by extending the probe range into visible with the white light super continuum (WLSC) beam. The WLSC probe beam have lower photon energies, the difference absorption are only rely to the positive ΔA, which is only determined by the excited state absorption process. This could provide some more details about the potential curves in the excited states directly, without the interferences from the other incoherent processes.

Then the experimental setup is constructed for this attempt, which is shown in Fig. 3.18. To generate the WLSC, we introduced another beam path from the same laser source. After the optimized long distance optical time delay which relative to the optical length of the DUV pulse generation, the new beam is focused on 2 mm-thick sapphire plate. As the discussion has been made in Chapter 2, the sapphire plate could provide the best stability performance of the WLSC beam among the nonlinear mediums we have. After the WLSC is generated and flittered the fundamental part, it is guided as the probe beam to the pump-probe experiment setup. In this setup, some modification of the propagation of DUV beam is applied: The former separated DUV beam is not divided by half mirror any more. Instead, the total energy of 300-nJ is pass

through the time delay stage as pump beam. And the prism reflector is also changed with the aluminum mirror to make the pump power be stronger. Considering the focus length for the DUV pump and WLSC probe beam is different, another concave mirror is set for the focusing of WLSC probe beam. The other components are used as usual setup.

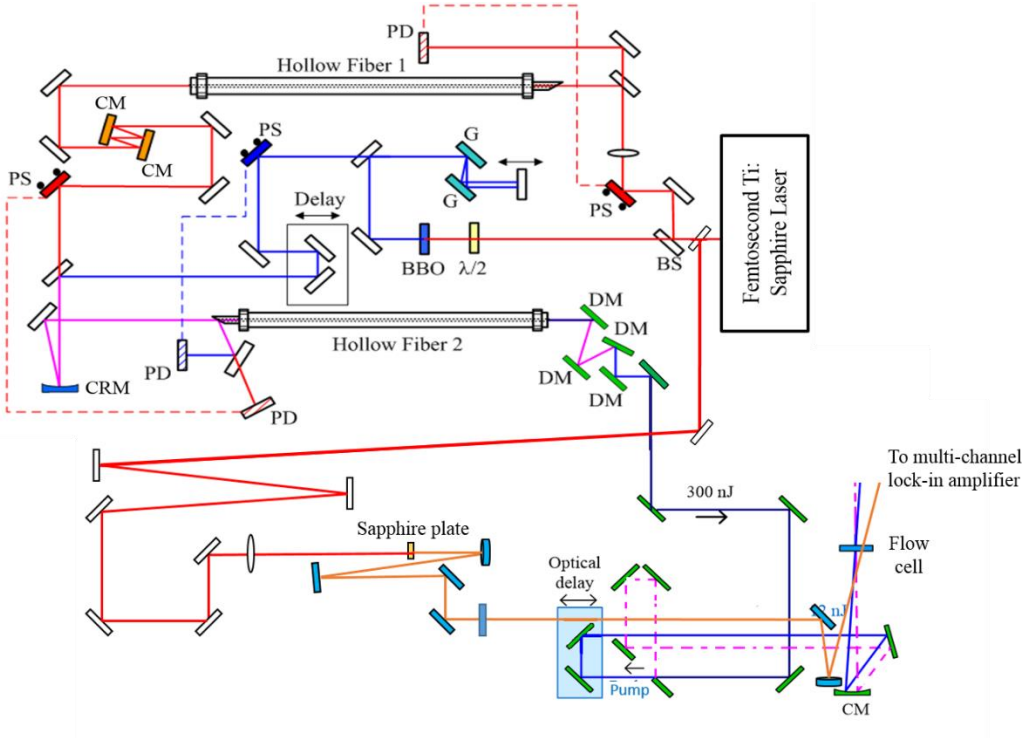

Fig.3.18 System scheme of the DUV pump WLSC probe laser system. BS: beam splitter; CM: concave mirror.

The absorbance difference raw data for thymine in aqueous solution is shown in Fig.3.19 (a), acquired by WLSC probing. It is easily to find the chirping effect is occurred in the 2DTR-ΔA, which is due to the uncompressed WLSC pulse. Later, the chirping cancelled ΔA map is obtained by manual modified the zero delay from the raw data,[17] which is shown in Fig.3.19 (b).

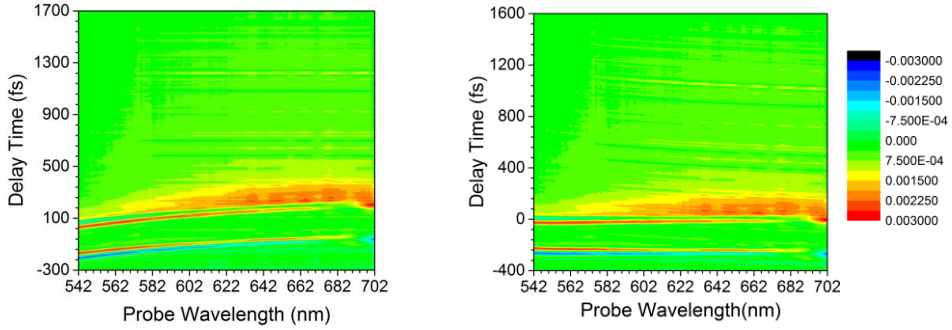

Fig.3.19 (a) Two dimensional absorbance difference of thymine in aqueous by WLSC probing. (b) Chirping cancelled two dimensional absorbance difference

From the data shown in Fig.3.19 (b), simple evaluation could be done first which is shown in Fig.3.20.

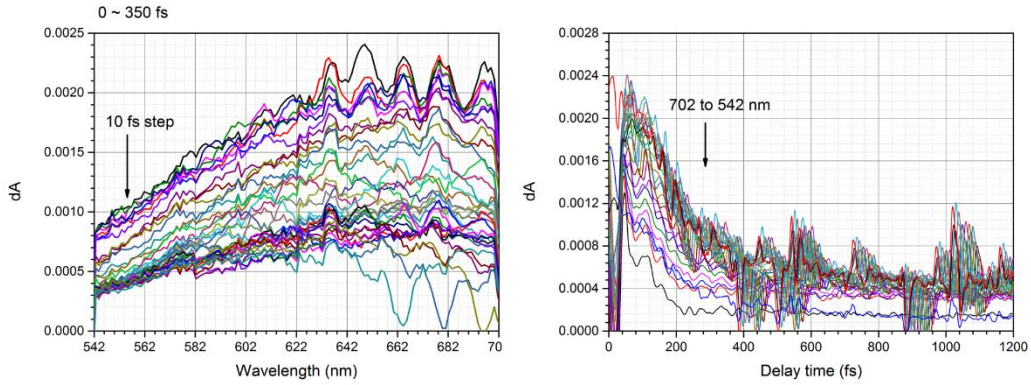

Fig.3.20 (a) Absorbance change spectrum of thymine in aqueous by WLSC probing. (b) Time resolved absorbance change of Thymine in Aqueous.

In the Fig.3.20 (b), it is easily to realize that the lifetimes are shorter than 200 fs within the visible probe photon range from the ΔA time traces, generally. Which is a simply agreement with the shortest lifetime component τ_1 in the DUV probe case. But, because of the extremely low level signals and the large noise which brought by the WLSC, especially from 642 nm to 700 nm range in Fig.3.20 (a), some fluctuation appeared in the time-resolved spectrum. This is considered to be due to the spectral shifting occurred during the WLSC probe beam is generated. And also in Fig.3.20 (b), at some peculiar delay time, large noise vibration occurred. Which is due to the intensity fluctuation of probe beam. From the above reasons, it is difficult to obtain more confident information from the present WLSC probe experiment. In the future

work, by solving the instability problem for the WLSC, we may get more discussible information for the DNA molecules.

3.4 Conclusion

In summary, sub-10-fs single DUV laser pulses have been applied to ultrafast spectroscopy on DNA bases in the DUV wavelength range. The short DUV pulses are generated by a chirped-pulse four-wave mixing technique. The electronic excited-state relaxation and vibrational dynamics of uracil and thymine in aqueous solution are simultaneously probed with a time resolution of a few femtoseconds. Two probe photon-energy dependent time constants are extracted from the difference absorption spectra measured in the time range of up to 1800 fs. From the lifetime spectrum, the relaxation process through CI is clearly understood. The shortest time constant of less than 100 fs can be assigned to the relaxation through CI from the first excited S_2 $^1(\pi\pi^*)$ state to the S_1 $^1(n\pi^*)$ state. The second shortest time constant of about 1 ps can be assigned to relaxation from the deformed S_{2d} $^1(\pi\pi^*)$ state to the S_0 ground state through CI. Especially, the locations of CI(S_2-S_1) and CI(S_{2d}-S_0) are experimentally clarified at 4.33 eV and 4.36 eV for uracil, 4.45 eV and 4.36 for thymine, respectively, and the widths are 0.21 eV and 0.038 eV for uracil, 0.05 eV and 0.031 eV for thymine, respectively. This assignment is made based on the information of electronic dynamics, obtained for the first time in the present work. The electronic decay strongly coupled vibrational dephasing is also understood with due to the fast decay population on the excited state.

Appendix I

1. Moment calculation

The moment is a quantitative measure of the shape of a set of points in mathematics. The *n*th moment is generally defined as:

$$\mu_n = \int_{-\infty}^{\infty}(x-c)^n f(x)dx \quad \text{(A.1)}$$

For the spectroscopic analysis, zeroth and first moment is usually used, which are defined as here:

$$M_0 = \frac{\int_{\omega_1}^{\omega_2}\Delta A(\omega)d\omega}{\omega_2-\omega_1} \quad \text{(A.2)}$$

$$M_1 = \frac{\int_{\omega_1}^{\omega_2}\omega\Delta A(\omega)d\omega}{\int_{\omega_1}^{\omega_2}\Delta A(\omega)d\omega} \quad \text{(A.3)}$$

Here, ω is the probe frequency and $\Delta A(\omega)$ is the difference absorption spectrum due to induced absorption, stimulated emission, and bleaching. There are three advantages for this moment method. The first is that the moment calculation is insensitive to the noise in the signal. The second advantage is due to the separation between the apparent transition energy and transition amplitude modulations. The third is the elimination of the contributions of the Raman and Raman-like interactions from wave packets in the ground and excited states. They do not contribute to the first moment if an appropriate integration range is selected, because the Raman contributions are determined by the zeroth moment.

The zeroth moment gives the strength of energy exchange between the pump / Stokes or pump / anti-Stokes pulses mediated by the coherent molecular vibration via vibronic coupling. It can be the corresponding coupling strength in case spectral distribution is appropriate for the interaction between the pump and Stokes pulses or the pump and anti-Stokes pulses. Therefore the values and spectral shape are relevant to the imaginary value and spectrum of the third-order nonlinear susceptibility of the stimulated Raman process. The first moment is related to the change of the refractive index induced by the molecular vibration.

2. Spectrogram calculation

The Fourier transform analysis of the oscillating ΔA signal over the delay time range offers more information of the averaged vibrational frequency over the range of the wave-packet motions. It is of greater interest to study the time evolution of the matching condition. One of the most advantageous approach is a spectrogram calculation,[50,51] which is used to study of the revivals of wave-packet motions in an harmonic systems in the gas-phase molecules such as Br_2[50] and K_2[51].

Generally, the spectrogram calculation is using the Short Time Fourier transform (STFT) method (see Fig. A.1), which defined as:

$$S(\omega,t)=\left|\int_{-\infty}^{+\infty}\Delta A_{OSC}(\omega,t)W_H(t-\tau)e^{i\omega t}dt\right| \quad (A.4)$$

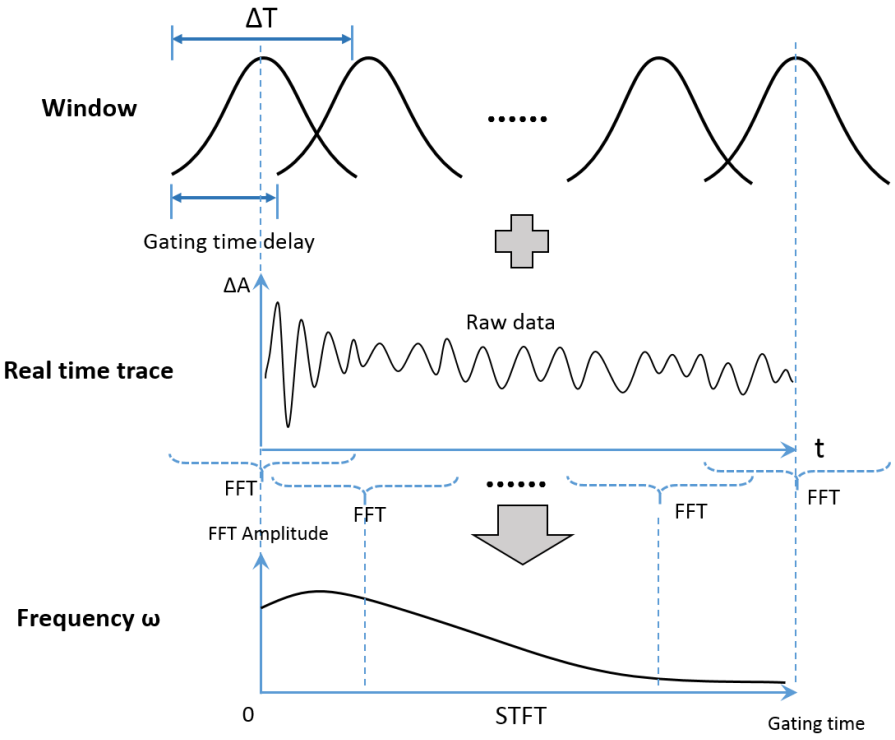

Fig. A.1 Scheme for spectrogram calculation

Where $S(\omega,t)$ is the short time range modified ΔA signal, $W_H(t)$ is a sliding window function applied on the raw data. In the previous analysis, a Blackman-type window functions has been proved for the best frequency responding in spectrogram analysis, which is defined as:

$$W_H(t) = 0.42 - 0.5\cos\left(\frac{2\pi t}{\Delta T}\right) + 0.08\cos\left(\frac{4\pi t}{\Delta T}\right) \quad \text{(A.5)}$$

Where ΔT is the variable full width of the window, and the FWHM of the Blackman window is equal to $0.4\Delta T$. Noticeably, if the window is sliding out of the raw data, zero will be automatically added for the FFT calculation. After the Fourier transform, the result shows as a two dimensions map for vibrational frequency versus gating delay time, which could provide the vibration decay information for the test samples. Considering the window width, for wider case, the frequency response will be more precisely, but for the time scale will loss accuracy. For shorter window case, responded performance will be just opposite and also the calculation will take more resources. The selection for proper window width would be in deep consideration.

References:

1. Crespo-Hernández, C. E.; Cohen, B.; Hare, P. M.; Kohler, B. Chem. Rev. 2004, 104, 1977–2020.
2. Kohler, B. J. Phys. Chem. Lett. 2010, 1, 2047–2053.
3. Schreier, W. J.; Schrader, T. E.; Koller, F. O.; Gilch, P.; Crespo-Hernández, C. E.; Swaminathan, V. N.; Carell, T.; Zinth, W.; Kohler, B. Science 2007, 315, 625–629.
4. Crespo-Hernandez, C. E.; Cohen, B.; Kohler, B. Nature 2005, 436, 1141–1144.
5. Schwalb, N. K.; Temps, F. Science 2008, 322, 243–245.
6. Gustavsson, T.; Improta, R.; Markovitsi, D. J. Phys. Chem. Lett. 2010, 1, 2025–2030.
7. Reuther, A.; Nikogosyan, D. N.; Laubereau, A. J. Phys. Chem. 1996, 100, 5570–5577.
8. Kwok, W.-M.; Ma, C.; Phillips, D. L. J. Am. Chem. Soc. 2008, 130, 5131–5139.
9. Reuther, A.; Iglev, H.; Laenen, R.; Laubereau, A. Chem. Phys. Lett. 2000, 325, 360–368.
10. Hare, P. M.; Crespo-Hernández, C. E.; Kohler, B. Proc. Natl. Acad. Sci. U.S.A. 2007, 104, 435–440.
11. Gustavsson, T.; Banyasz, A.; Improta, R.; Markovitsi, D. J. Phys. Conference Series 2011, 261, 012009.
12. Gustavsson, T.; Bányász, Á.; Lazzarotto, E.; Markovitsi, D.; Scalmani, G.; Frisch, M. J.; Barone, V.; Improta, R. J. Am. Chem. Soc. 2005, 128, 607–619.
13. Krummel, A. T.; Zanni, M. T. J. Phys. Chem. B 2006, 110, 13991–14000.

14. Dwyer, J. R.; Szyc, Ł.; Nibbering, E. T. J.; Elsaesser, T. J. Phys. Chem. B 2008, 112, 11194–11197.

15. Towrie, M.; Doorley, G. W.; George, M. W.; Parker, A. W.; Quinn, S. J.; Kelly, J. M. Analyst 2009, 134, 1265–1273.

16. Szyc, Ł.; Yang, M.; Nibbering, E. T. J.; Elsaesser, T. Angewandte Chemie International Edition 2010, 49, 3598–3610.

17. Pecourt, J.-M. L.; Peon, J.; Kohler, B. J. Am. Chem. Soc. 2001, 123, 10370–10378.

18. Lan, Z.; Fabiano, E.; Thiel, W. J. Phys. Chem. B 2009, 113, 3548–3555.

19. Mercier, Y.; Santoro, F.; Reguero, M.; Improta, R. J. Phys. Chem. B 112, 10769 (2008).

20. Nachtigallová, D.; Aquino, A. J. A.; Szymczak, J. J.; Barbatti, M.; Hobza, P.; Lischka, H. J. Phys. Chem. A 2011, 115, 5247–5255.

21. Yamazaki, S.; Taketsugu, T. J. Phys. Chem. A 2012, 116, 491–503.

22. Nakayama, A.; Arai, G.; Yamazaki, S.; Taketsugu, T.; J. Chem. Phys. 2013, 139, 214304.

23. Buchner, F.; Nakayama, A.; Yamazaki, S.; Ritze, H.; Lübcke A. J. Am. Chem. Soc. 2015, 137, 2931–2938.

24. Kobayashi, T.; Saito, T.; Ohtani, H. Nature 2001, 414, 531–534.

25. Ishii, N.; Tokunaga, E.; Adachi, S.; Kimura, T.; Matsuda, H.; Kobayashi, T. Phys. Rev. A 2004, 70, 023811.

26. Polli, D.; Cerullo, G.; Lanzani, G.; De Silvestri, S.; Hashimoto, H.; Cogdell, R. J. Biophys. J. 2006, 90, 2486–2497.

27. Lüer, L.; Gadermaier, C.; Crochet, J.; Hertel, T.; Brida, D.; Lanzani, G. Phys. Rev. Lett. 2009, 102, 127401.

28. Iwakura, I.; Yabushita, A.; Kobayashi, T. J. Am. Chem. Soc. 2008, 131, 688–696.

29. Virgili, T.; Lüer, L.; Cerullo, G.; Lanzani, G.; Stagira, S.; Coles, D.; Meijer, A. J. H. M.; Lidzey, D. G. Phys. Rev. B 2010, 81, 125317.

30. Kobayashi, T.; Kida, Y. Phys. Chem. Chem. Phys. 2012, 14, 6200–6210.

31. Durfee, C. G., III; Backus, S.; Kapteyn, H. C.; Murnane, M. M. Opt. Lett. 1999, 24, 697–699.

32. Baum, P.; Lochbrunner, S.; Riedle, E. Appl. Phys. B: Lasers Opt. 2004, 79, 1027–1032.

33. Fuji, T.; Horio, T.; Suzuki, T. Opt. Lett. 2007, 32, 2481–2483.

34. Trushin, S. A.; Kosma, K.; s, W. F.; Schmid, W. E. Opt. Lett. 2007, 32, 2432–2434.

35. Graf, U.; Fieβ M.; Schultze, M.; Kienberger, R.; Krausz, F.; Goulielmakis, E. Opt. Express 2008, 16, 18956–18963.

36. Reiter, F.; Graf, U.; Schultze, M.; Schweinberger, W.; Schröder, H.; Karpowicz, N.; Azzeer, A. M.; Kienberger, R.; Krausz, F.; Goulielmakis, E. Opt. Lett. 2010, 35, 2248–2250.

37. Kida, Y.; Kobayashi, T. J. Opt. Soc. Am. B 2011, 28, 139–148.

38. Kida, Y.; Liu, J.; Teramoto, T.; Kobayashi, T. Opt. Lett. 2010, 35, 1807–1809.

39. Whitten, D. G.; Lee, Y. J. J. Am. Chem. Soc. 1971, 93 (4), 961–966.

40. Yang, N. C.; Elliott, S. P. J. Am. Chem. Soc. 1968, 90 (15), 4194–4195.

41. Russo, N.; Toscano, M.; Grand, A. J. Comput. Chem. 2000, 21 (14), 1243–1250.

42. Kobayashi, T.; Wang, Y.; Wang, Z.; Iwakura, I. Chem. Phys. Lett. 2008, 466, 50–55.

43. Kobayashi, T.; Du, J.; Feng, W.; Yoshino, K. Phys. Rev. Lett. 2008, 101, 037402.

44. Yarasi, S.; Billinghurst, B. E.; Loppnow, G. R. J. Raman Spectrosc. 2007, 38, 1117–1126.

45. Yarasi, S.; Ng, S.; Loppnow, G. R. J. Phys. Chem. B 2009, 113, 14336–14342.

46. Saito, T.; Kobayashi, T. J. Phys. Chem. A 2002, 106, 9436–9441.

47. Liu, J.; Okamura, K.; Kida, Y.; Teramoto, T.; Kobayashi, T. Opt. Express 2010, 18, 20645–20650.

48. Baltuška, A.; Fuji, T.; Kobayashi, T. Opt. Lett. 2002, 27, 306–308.

49. Backus, S.; Peatross, J.; Zeek, Z.; Rundquist, A.; Taft, G.; Murnane, M. M.; Kapteyn, H. C. Opt. Lett. 1996, 21, 665–667

50. Vrakking, M. J. J.; Villeneuve, D. M.; Stolow, A. Phys. Rev. A 1996, **54**(1), 37-40.

51. Claas, P.; Droppelmann, G.; Schulz, C. P.; Mudrich, M.; Stienkemeier, F.; J. Phys. B 2006, **39**(19), S1151.

Chaptor 4: Measurement of non-degenerate two-photon absorption spectrum by using super continuum beam

4.1 Introduction

Research activity on materials that exhibit high nonlinear optical ability had increased dramatically in the recent years. In particular, the two-photon absorption (TPA) was also exploited in several current technologies, including optical power limitier,[1] all-optical shutter,[2] two-photon fluorescence microscopy,[3,4,5] and others.[6] For the measurement of spectra and cross sections of TPA in the nonlinear materials, generally, the two-photon induced fluorescence (TPIF)[7,8,9] is most frequently used and while the Z-scan method[10,11] is less commonly employed. In order to acquire broaden TPA spectrum information, demand for wide tunable laser sources is needed, such as the optical parametric amplifier (OPA) or dye laser sources.[7,12,13] But, even with a tunable source, the measurement must be repeated for each selected wavelength. As it is often impossible to maintain the experimental conditions throughout the time required to perform the measurement for each wavelength across the full spectral range, experimental errors are introduced. The instability in the peak intensity of the laser pulses also inevitably induces large experimental errors into this time-consuming measurement, a problem that is further enhanced by the nonlinearity of the process. Furthermore, due to the diversification in the pulse duration during the pulse wavelength shifting, the pulse intensity changes for each measurement. In addition, these methods are indirect ways to measure the TPA spectrum, and thus may suffer from other systematic errors related to the intermediate parameters, such as the collection efficiency of emitted fluorescence, fluorescence quantum efficiency, and so on.[7] Finally, the degenerate detection's intensity squared dependence on the excitation beam intensity may lead to a large error during the square calculation. Such inaccuracies may affect the measurements and may explain the quite different TPA cross section values that have been reported when the same method is used to examine some well-known materials.[7,12,14,15] In 1999, Belfield, *et al.*, first reported the approach

to measure the nondegenerate TPA (shown in Fig.4.1) spectrum by utilizing a pump-probe two-beam configuration,[16] in which the strong pump was a monochromic IR laser beam and the weak probe was a white-light super-continuum (WLSC) beam. In this setup, a broad TPA spectrum can be directly measured in a single procedure by the spectral subtraction of the absorbed probe beam from the reference beam. The pump beam intensity has a linear dependence on the TPA cross section (as discussed later), which apparently induces a lower level of error than the intensity squared degenerate detection. However, the acquired spectrum difference is time dependent due to the overlapping time shift between pump and probe beams. This is due to the chirping effect occurring during the WLSC generation and the group-velocity dispersion (GVD) effect on the probe pulse propagation time. Kovalenko *et al.* proved that the chirp could be eliminated by using time-correction procedure when using a supercontinuum probe.[17] However, since the publication of the work by Belfield *et al.*, there have only been a few reports using this setup for a limited number of direct-gap semiconductors and semiconductor quantum dots.[18,19]

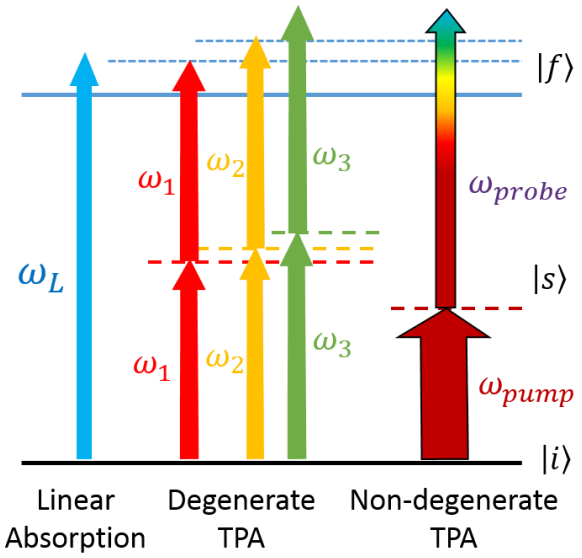

Fig.4.1 Energy schemes for photon absorptions. $|i\rangle$, $|s\rangle$, $|f\rangle$ are corresponding to the initial, intermediate, final state, respectively.

In this study, we improve this method in several ways. First, compress the WLSC pulses by chirp-mirror pairs before propagation to the sample. Since it is extremely

difficult for the chirp to be fully removed because of the complex WLSC generation process. It includes the self-phase modulation, plasma generation, and stimulated Raman processes and others. One step closer, a time-resolved two-dimensional induced absorption (ΔA) spectrum observed for the probe beam is acquired to help to identify the pump and probe pulse overlaps with each other for the determination of wavelength dependent zero-delay time of the probe continuum with respect to the pump pulse induced by the chirp. To achieve this, we introduce the combination of a polychromater equipped with a multi-channel lock-in amplifier (MLA) as the detector to replace the spectrometer in the Belfield's work.[16] The MLA not only causes a large improvement of the signal noise ratio (SNR), but also makes it possible to simultaneously and directly measure a broadband difference absorption spectrum with 128 spectral points and a spectral resolution of 0.83 nm. With this high performance equipment, the TPA profiles for several laser dyes. The TPA spectra thus obtained are confronted to theoretical predictions to further validate our approach.

4.2 Theory of non-degenerate two photon absorption (TPA)

In general the attenuation of a light beam passing through an optical medium along an axis designated here as z-axis can be generally expressed by the following phenomenological expression in case of including linear and nonlinear interactions:[20]

$$\frac{dI(z)}{dz} = -\alpha I(z) - \beta I^2(z) - \gamma I^3(z) - \cdots \tag{4.1}$$

Here $I(z)$ is the intensity of the incident light beam propagating along the z-axis and α, β, γ are the one-, two-, three-photon absorption coefficients of the transmitting medium, respectively. For the absorption induced by two photon process with negligible band width of the incident laser in comparison with the electronic bandwidths relevant to the two-photon transition including virtual states, we have:

$$\frac{dI(z)}{dz} = -\beta I^2 \tag{4.2}$$

In the case of the non-degenerate condition, in our situation for an intensity I_1 of the pump beam and I_2 for the WLSC probe beam, leads to:

$$\frac{dI_1(z)}{dz} = -\beta_1 I_1 I_2 \tag{4.3}$$

$$\frac{dI_2(z)}{dz} = -\beta_2 I_1 I_2 \tag{4.4}$$

Here the two photon absorption coefficients β is linear proportional to the imaginary part of the third-order nonlinear susceptibility as given by: [21]

$$\beta_{1,2} = \frac{8\pi^2 \omega_{1,2}}{c^2 \varepsilon_1^{1/2} \varepsilon_2^{1/2}} \operatorname{Im} \chi^{(3)} \tag{4.5}$$

$$\operatorname{Im} \chi^{(3)} = N\pi \left| M_{fi} \right|^2 g\left(\hbar\left(\omega_1 + \omega_2 - \omega_{fi}\right)\right)\left(\rho_i - \rho_f\right) \tag{4.6}$$

$$M_{fi} = \sum_s \left[\frac{\langle f | e\mathbf{r} \cdot \hat{e}_2 | s \rangle \langle s | e\mathbf{r} \cdot \hat{e}_1 | i \rangle}{\hbar(\omega_1 - \omega_{si})} + \frac{\langle f | e\mathbf{r} \cdot \hat{e}_1 | s \rangle \langle s | e\mathbf{r} \cdot \hat{e}_2 | i \rangle}{\hbar(\omega_2 - \omega_{si})} \right] \tag{4.7}$$

Here N is the density of molecules in the medium, ε_j and $\hat{e}_j$ denotes the dielectric constant and the field polarization vector at the angular frequency of ω_j for each incident light, ρ_i and ρ_f are the populations in initial state $|i\rangle$ and final state $|f\rangle$, and $|s\rangle$ is the intermediate state, finally $g(\hbar\Delta\omega)$ describing the line shape is the joint density of states of the TPA transition. Set I_{10} and I_{20} to be the beam intensities before the medium, and in the case of $I_{10} \gg I_{20}$, the Eqs.4.3 and 4.4 could be solved as:

$$I_1 \cong I_{10} \tag{4.8}$$

$$I_2 \cong e^{-\beta_2 I_{10} z} I_{20} \tag{4.9}$$

Then,

$$\beta_2 I_{10} z = -\ln \frac{I_2}{I_{20}} = -\frac{1}{\lg e} \lg \frac{I_2}{I_{20}} = \frac{1}{\lg e} \Delta A \tag{4.10}$$

From Eq.4.4, it is easy to find that, with an intense pump, the TPA coefficient is

linear proportion to the difference absorbance (ΔA) of WLSC probe beam. Since the relationship between TPA cross section σ_2 (in unit of cm^4/GW) and TPA coefficient (in unit of cm/GW) is given by: [17]

$$\beta_2 = \sigma_2 N_A c \times 10^{-3} \tag{4.11}$$

Here N_A is Avogadro constant, and c is the concentration of the sample (in unit of M (1 M = 1 mol/L)). From Eq. 4.10 and Eq. 4.11, we can easily get a conclusion that TPA cross section is proportional to the absorbance change($\sigma_2 \propto \Delta A$). As ΔA could be directly be acquired through pump probe experiment, the TPA cross section could be calculated from experimental data without further error sources introduced by intermediate method. Noteworthy, in this study, all spectra reporting TPA cross sections are based on the transformed TPA wavelength, which is the relative value calculated using ($2/\lambda_{TPA} = 1/\lambda_{pump} + 1/\lambda_{probe}$). And the unit of TPA cross section σ_2 is unified as GM (1 GM = 10^{-50} cm^4 s $photon^{-1}$).

4.3 Experimental setup for TPA spectral acquirement

We use some fractions of the output energy from the amplifier system (Spectra Physics, model Spitfire Ace) with pulse energy of about 180 μJ (1 kHz repetition rate, 798 nm central wavelengths). As shown in Fig.4.2, about 10% reflection from a beam splitter is used to be divided into two beams, then the reflected beam is used to generate the WLSC, and the transmitted one is used as a pump beam. For the WLSC beam generation, fundamental beam is focused on a 2-mm-thick sapphire plate surface. By transmitting through a 720 nm short-pass dichroic mirror, strong fundamental part is blocked. The WLSC spectrum range is covering from 500 nm to 730 nm. A pair of chirp mirrors (GVD, 470~810nm, -40 ± 20fs^2) are used to compress the WLSC beam by a triple-pass configuration. After this, the WLSC beam with time-delayed pump beam are both focused by an off-axis parabolic mirror and overlapped at the sample point. After passing through the sample, the beams are collimated by another off-axis parabolic mirror.

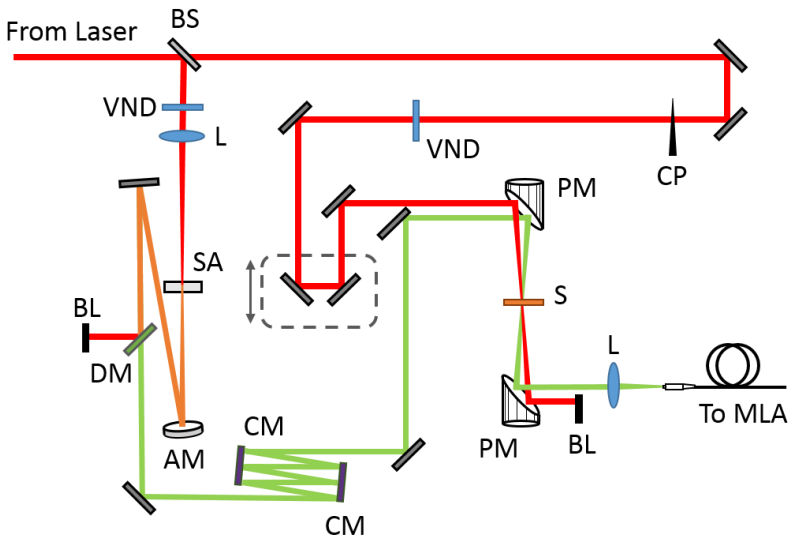

Fig.4.2. Schematic diagram for the TPA spectrum and cross section measurement system (BS: Beam splitter; VND: Variable neutral density filter; L: Lens; SA: Sapphire plate; AM: Concave Mirror; DM: Dichroic mirror; BL: Blocker; CM: Chirp Mirror; PM: Off-axis Parabolic Mirror; S: Sample; CP: Chopper.)

Pulse duration of this fundamental pump beam is measured to be 103 fs by the SHG-FROG method.[22] The spot size of the focused pump beam at the sample surface is measured by a CCD beam profiler (Thorlabs, BC106N-VIS) with 146.1 μm width on X-axis and 149.9 μm on Y-axis, see in Fig.4.3. For the data collection, the WLSC probe beam finally is focused into a multimode fiber later, which is guided to the polychrometer and the signal captured by the 128-channel lock-in amplifier (MLA). A synchronized chopper with a half of the laser repetition frequency is introduced in the fundamental beam path and provided the reference frequency signal for the MLA. And the pump beam power is controlled by a wheel gradient neutral density filter set in the pump path.

Noticeably, the pump beam intensity is quite critically important in the TPA cross section calculation. For a Gaussian shape laser pulse, the peak intensity is usually calculated by using the following function:

$$I_0 = \frac{2P_0}{\pi \Delta x \Delta y \tau g} \tag{4.12}$$

Here, P_0 is the average power of the pump laser beam, g is the repetition frequency of

the laser, τ is the pump pulse duration at FWHM, Δx and Δy is the beam spot width in two perpendicular directions. Usually the spot is circular and $\Delta x = \Delta y$. As an example for the experiment value, with the pump power be 400 μW, the peak intensity would be 11.3 GW/cm^2.

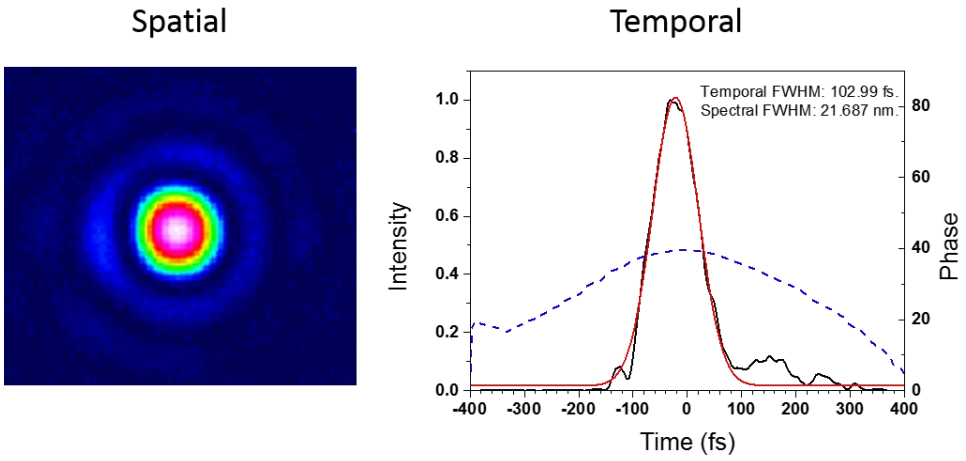

Fig.4.3 Spatial and temporal status of the pump beam on the sample point, measured by CCD camera and SHG-FROG measurement.

4.4 TPA spectral features of the laser dyes

Laser dyes are organic molecules which are usually used as laser medium in a dye laser. These organic molecules could be dissolved in many liquid solvent. Such as water, methanol, and chloroform. Basically, laser dyes contain the chromophore region which induces a visible spectrum. Visible light exposed to the chromophore can thus be absorbed by exciting an electron from its ground state into an excited state. Base on the chromophore, the laser dyes could be classified by the coumarins, xanthenes (rhodamines), oxazines, and so on. Usually coumarin emits in the green region of the spectrum while xanthenes are used for emission in the yellow-red. Laser dyes are also used to dope solid-state matrices, such as polymethyl methacrylate (PMMA), and ORMOSILs, to provide gain media for solid state dye lasers. As the linear absorption properties of these dyes are already well studied, nonlinear phenomena such as TPA are apparently of more interest. Even though such demand exists, due to limited method of measurement, seldom TPA spectrum with high spectral resolution are well

investigated in such large families of laser dyes. In this work, the TPA profiles of several laser dyes are investigated by using the nondegenerate TPA method mentioned before. They are two xanthene dyes, rhodamine 6G and rhodamine 123 ([6-amino-9-(2-methoxycarbonylphenyl)xanthen-3-ylidene]azanium chloride), dissolved in methanol; two coumarins dyes, coumarin 6 (3-(2-Benzothiazolyl)-7-diethylamino-coumarin) and coumarin 343 (2,3,6,7-Tetrahydro-11-oxo-1H,5H,11H-[1]benzopyrano[6,7,8-ij]quinolizine-10-carboxylic acid), dissolved in chloroform; and two oxazine dyes, Nile red (9-diethylamino-5-benzo[α]phenoxazinone) and Nile blue A (Basic blue 12), dissolved in chloroform. All of the dyes are purchased from Sigma-Aldrich and used without further purification.

4.4.1 TPA spectral features of coumarin 6 and rhodamine 6G in solvent

4.4.1.1 Coumarin 6

One typical result for the TPA spectrum measurement is shown in Fig.4.4, by using an organic fluorescent dye - Coumarin 6 (Sigma-Aldrich, reagent grade) which is dissolved in chloroform with the concentration of 23.7 mM without purification. The time-resolved two-dimensional spectra of difference absorbance (ΔA) calculated by using the WLSC probe is shown in Fig.4.4 (a). A large positive signal located at the center, around 560 nm, with a delay time of around zero, corresponds to the TPA effect. The black solid line is obtained by peak tracking for this ΔA map; it shows the zero time position where the pump and probe pulses overlap.[17] Because of the group velocity dispersion (GVD) in this solvent sample, this overlap maximum peak tracing line becomes curved with respect to the wavelength. From Fig.4.4 (a), with the ΔA values obtained from MLA detection, the TPA coefficients could be directly obtained from Eq. (4.10), results being shown in Fig.4.4 (b). It has a spectral resolution of about 10 nm, which is due to the FWHM of pump spectral shape. For coumarin 6, it has a TPA peak value at 652 nm with a cross section of 1015 ± 107 GM.

For the error evaluation of measurement results, we mainly consider two parts of the error sources: probe pulse error and pump pulse error. Probe pulse error is due to

the instability of probe beam and probe signal detection error. The detection error here could be negligibly small, because of the introduced high precision lock-in detection. Meanwhile the stabilities of probe beam in spectrum plays much more important roles. And for the pump pulse intensity error, it is relative to many measured parameters, such as beam power, spot size and pulse duration. The measurement error from those parameters will finally go to the TPA cross section results. Especially in the ordinary degenerate measurement, this pump error is squared and could not be avoided by the limitation of method. However the error from the pump pulse is affected to the full TPA spectrum without wavelength dependence while the probe error has wavelength dependence. The final total error is defined by the mean square root of all error sources and applied to all TPA results in this thesis.

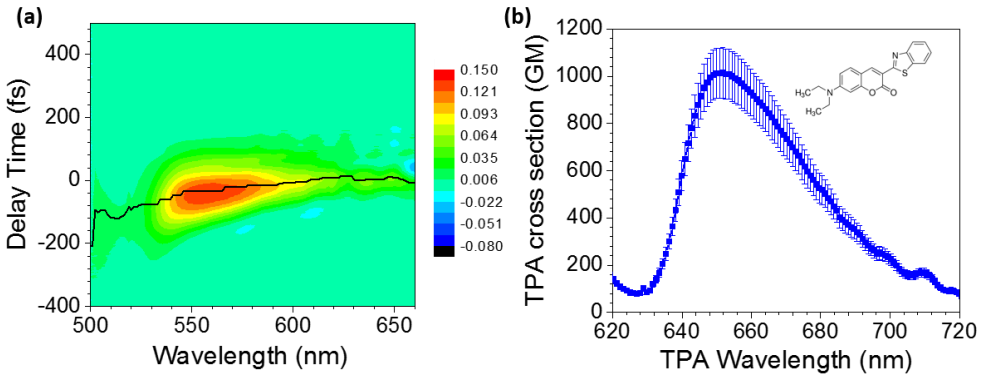

Fig.4.4 (a) two dimensional ΔA map for coumarin 6 in chloroform. (b) Measured TPA cross section spectrum for coumarin 6.

4.4.1.2 Rhodamine 6G

Rhodamine 6G (Sigma-Aldrich) dissolved in methanol (concentration: 16.2 mM) has also been measured, the two-dimensional ΔA map is shown in Fig.4.5. Due to the loss by the stationary absorption of the sample solution, the WLSC spectral probe range is limited to the lowest at 562 nm. In a similar phenomenon to the coumarin 6 sample, large positive ΔA is observed from 562 nm to 658 nm. Noticeably, in the same spectral range, some large negative signal appear at the positive delay time and the intensity decrease with the wavelength. This is confirmed to be due to the stimulated emission (SE) from Rhodamine 6G by comparing this negative spectrum with the

spontaneous fluorescent spectrum. The SE could also be observed in ΔA map coumarin 6 when narrowing the intensity scale, since the intensity is too weak to perceive in Fig.4.4 (a).

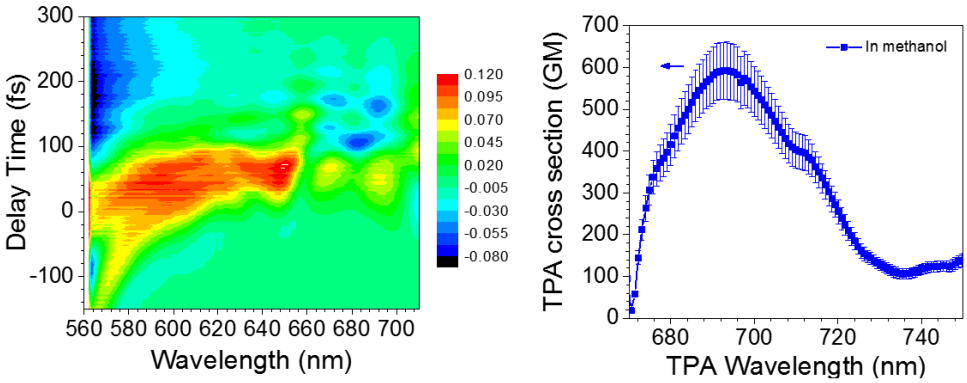

Fig.4.5 Rhodamine 6G's ΔA map and calculated TPA cross section.

4.4.2 Interference between resonant solute signal and non-resonant solvent signal

Two-photon absorption is one of the third-order nonlinear phenomena. Another third order nonlinear effect like stimulated Raman scattering is also possible to occur in this nondegenerate pump probe experiment. Strong stimulated Raman loss[22] (SRL) signal induced by the methanol is found in methanol solvent only as a blank test, the experimental result of two dimensional "time-resolved" SRL spectrum is shown in Fig.4.6 (a).

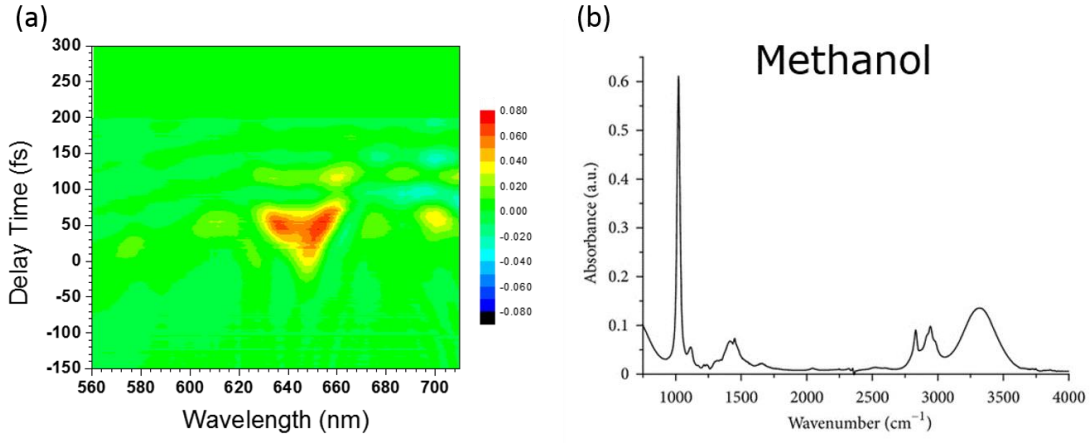

Fig.4.6 (a) Two dimensional ΔA map for methanol in blank test. (b) Raman spectrum of methanol

In the figure, an inverted triangle shape positive signal locate around 645 nm with a two-peak structure on intensity distribution. These two peaks are due to two modes with the Raman shift of 3000 cm^{-1} and 3300 cm^{-1}, shown in Fig.4.6 (b), which are corresponding to the -CH_3 asymmetric stretch and the -OH stretch. Many common solvents, such as ethanol, benzene, and water, have similar intense Raman loss signal. These signals must be carefully treated to obtain the TPA spectrum of the target material in solution. From preparatory experiment to search for solvents free from Raman loss disturbance, it is recommended to use carbon tetrachloride (CCl_4) or chloroform ($CHCl_3$), since these solvents do not have intense Raman loss signal around 3000 cm^{-1}. The 2D Raman loss spectrum are shown in Fig.4.7. All the results are acquired under the same experimental conditions of pump and probe pulses. Solvents are in a 1-mm thick quartz cell. The figures displays spectra in a normalized intensity with same scale bar. Ethanol shows the strongest Raman loss signal with center wavelength at 645 nm. Methanol, water, benzene, also show intense SRL signal in the same spectral range.

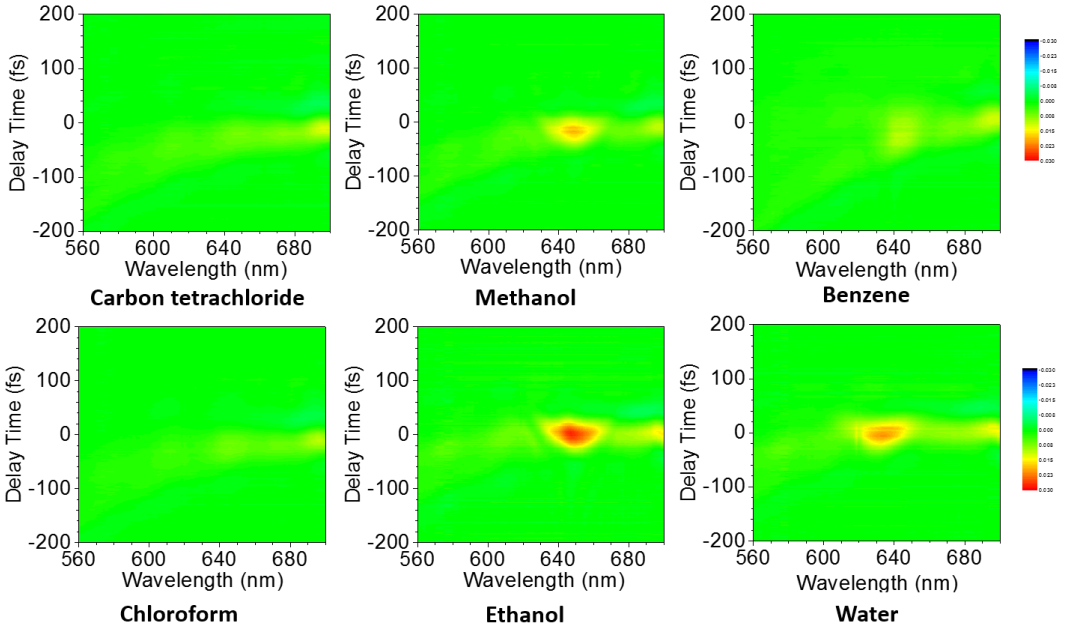

Fig.4.7 2D stimulated Raman loss ΔA map of some common solvents.

However, many common organic dyes such as xanthene dyes have poor solubility in these solvents. In such a case of using solvent with intense Raman signal,

appropriate elimination of the contribution of Raman loss signal due to solvent is needed to correctly acquire the TPA spectrum. By comparing the Fig.4.5 and Fig.4.6, the TPA signal accompanied with the solvent Raman loss signal is clearly recognized and marked with red dashed circles.

It is difficult to distinguish the SRL's contribution to the TPA signal when they are spectrally overlapping, as they are both two-photon processes belonging to the comparable third-order nonlinear effects.[17,22] The two incident beams (WLSC (ω_1) and 800 nm (ω_2)) can interact with each other in time overlapping conditions, and both the ω_1 photons and the ω_2 photons can be absorbed during a TPA process. In the same way, when associated with the ω_1 photons, the ω_2 photons can be absorbed (scattered) by the Stokes mechanism or can be amplified by the anti-Stokes mechanism if the vibrational difference level corresponding to the frequency difference ($\omega_1 - \omega_2$) is populated. The latter case is not fulfilled in this experiment. Furthermore, coupling between the TPA and Raman processes may occur if the solvent levels in the sample (including at the solvent molecule level) are coherently coupled.

The vibronic states of solvent molecules do not lead to strong coupling with the solute vibronic states due to the lack of strong interaction through the hydrogen bonding. Therefore, there is no "intrinsic" interference between the electronic polarization and the solute molecule coherence in the solvent system. However, an extrinsic interference is possible. For example, interference may occur if an amplified ω_2 photon created via a stimulated Raman scattering by ω_1 photons is used in the TPA together with ω_1. The Raman gain expected for a ω_2 photon when ω_1 photons exist can be estimated by the Raman correspondence of the solute molecule with a 24.7 M concentration. It is 5×10^{12} photons/cm^{2}sec when the number of ω_1 photons is 2×10^{16} photons/cm^{2}sec. The loss of the probe light through this process can be completely negligible, and the following equation can be used:

$$\Delta A(\omega) = \Delta A_{TPA}(\omega) + \Delta A_{SRL}(\omega) \quad . \tag{4.13}$$

Here, ΔA_{TPA} and ΔA_{SRL} refer to the TPA and Raman loss effect, respectively. For the

solvent sample, which is a mixture of the solute and solvent, the effect of both should be considered. Especially in this setup, it is expected that the TPA will not create interference, even in the neat solvents, as the absorption edge of the solvent molecules are located much higher (blue side) than the half of the shortest edge of the continuum spectrum. However, Raman scattering of the solute scarcely occurs in a relative Raman shift larger than 2000 cm^{-1}. Even if, due to the solute in the sample, the Raman signal makes a contribution, it is expected to have a negligibly low intensity as the concentration of the dyes molecules is lower than the concentration of solvent molecules by the factor of 10^{-3}. The concentrations of the solute and solvent in the experiment are calculated to be 24.7 M and 8.1×10^{-3} M, respectively. Therefore for the right part of the Eq. (4.13), it is concluded that ΔA_{TPA} is due to the solute only and ΔA_{SRL} is from solvent only.

4.4.3 TPA spectral features of rhodamine 6G in polymer

A polymethyl methacrylate (PMMA) thin film doped with rhodamine 6G is investigated with the expectation of directly removing the solvent interference. PMMA has a large molecular weight and is transparent in the visible and near IR light range; thus, it is expected to be an appropriate matrix to investigate TPA of organic molecules. The PMMA powder and rhodamine 6G are both dissolved in chloroform and mixed with each other; then the mixture is dried and spin-coated on a glass plate. After being stripped from the slide, the film is used for the measurement. The measured ΔA map in Fig.4.8 (a) shows that no large ΔA peak around 645 nm (red dashed circle mark) with this sample, which means the background effect is effectively minimized.

However, it is difficult to directly determine the TPA cross section with this doped PMMA film, because it is difficult to precisely determine the film thickness and the number of dissolved molecules, as the molecules in the polymer matrix sample are inhomogeneous. This is a serious problem in any kind of spectroscopic measurement of doped molecules in a polymer film. In spite of this, the relative values of the TPA cross section recorded at different wavelengths are reliable due to the broadband

measurement. This is verified with several scans. Fig.4.6 that, suggests that, for the probe range 580 nm to 600 nm, the distortion effect from the solvent is negligible. Then, by assuming that rhodamine 6G has the same TPA properties in methanol as in PMMA, we can reconstruct a more reliable TPA cross section spectrum by merging and scaling the result in PMMA to the methanol case, results being shown in Fig.4.8 (b). It shows that the measurement starts with the blue round line from 670 nm and transforms into the red open square line around 690 nm. The optimized TPA peak is located at 691 nm with a cross section of 596 ± 69 GM.

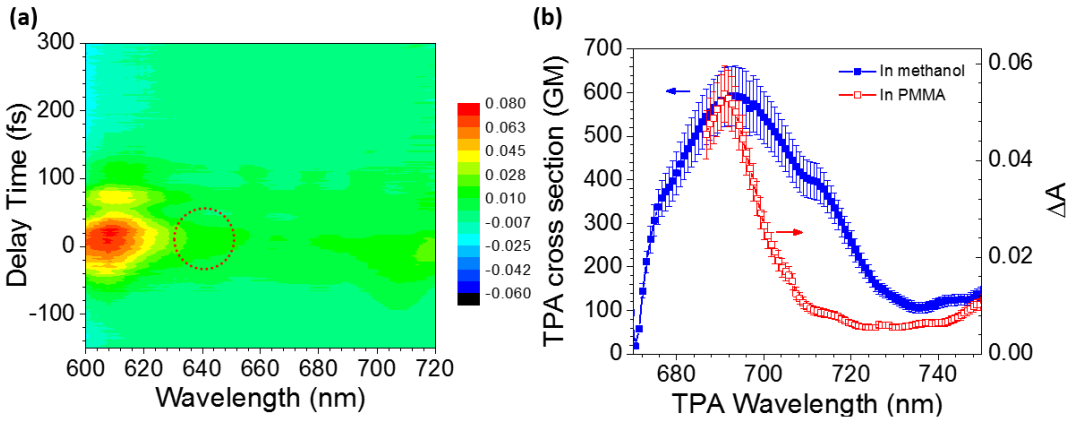

Fig.4.8 (a) Two-dimensional ΔA map for rhodamine 6G doped in PMMA film. (b) TPA cross section acquired from methanol solvent sample shown in blue dot curve; modified TPA cross section spectrum obtained in PMMA film shown in red square curve.

4.4.4 Dependence of the incident pump pulse intensity and sample concentration on the TPA spectra

The dependence of TPA spectra on the pump power and sample concentration are both investigated. Here we show the case of the sample of Rhodamine 6G in methanol. For pump power dependence, the sample concentration is fixed to be 16.2 mM. The pump power is adjusted between 40 μW and 840 μW by variable neutral density filter. For convenience, we select the ΔA peak value at 620 nm on each pump power ΔA map, which are shown as blue triangles in Fig.4.9. The linear fitting with nearly zero intercept shows a good agreement with Eq. (4.10). Nearly no saturated effect in absorption is observed in this pump power range. Also for the concentration dependence measurement, the pump power is fixed at 400 μW. Several samples with

different concentration are studied in the similar way: ΔA peak values at 600 nm and 620 nm for each concentration are marked with black circle and red round respectively in Fig.4.9. By the linear fitting for each group, 600 nm group ΔA data shows a nearly zero intercept, but 620 nm group obviously does not. This non-zero intercept present the indication of the solvent Raman loss interference mentioned in section 4.4.2. Only in the case of the zero intercept fitting line is verified that the signal is purely due to TPA process.

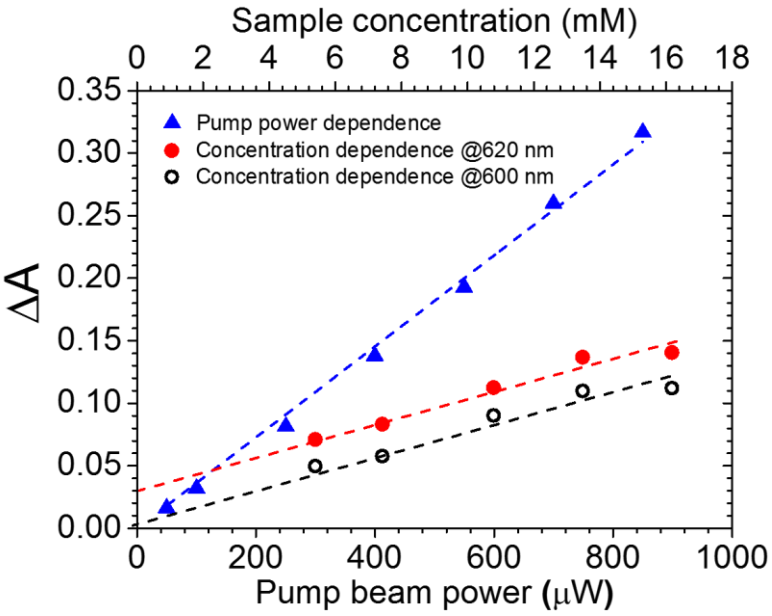

Fig.4.9 Pump power dependence and concentration dependence for nondegenerate TPA cross section measurement.

4.4.5 Enhanced phenomenon on non-degenerate TPA cross section

The TPA cross section of rhodamine 6G TPA measured in this work is compared with previous literature values in Table II. The results all agree that the position of the TPA peak is around 690 nm. Obviously, the NDTPA values in this work are larger than the DTPA values found in other reports which performed by using degenerate conditions. Noteworthy, ns pulses are known to overestimate TPA cross sections, especially due to excited state absorption (the TPA can be non-simultaneous). For those reported values, the TPA measurement is mainly based on two-photon induced fluorescence (TPIF) method which was first reported by Xu *et al.* in 1996,[7] which are

indirect measurements involved with several intermediate parameter, such as the collection efficiency of emitted fluorescence, fluorescence quantum efficiency, and so on.[7] Furthermore, in the degenerate TPA case, the signal is square dependence on the power of excitation pulse. Then the error in the pump intensity is enhanced in the squared value. The inaccuracies of these factors may result in, thus quite dispersed TPA cross section values in the reported papers even though experiments are performed by using same method.[5,12,17] However, in nondegenerate case, direct detection method avoid to add more error sources. Pump beam intensity has a linear dependence to the TPA cross section, which apparently induces lower level of the error. On the other hand, some literature also reported that the nondegenerate results usually show higher TPA cross section than the degenerate cases.[20,25] This phenomenon can be explained as an intermediate state resonance enhancement (ISRE); one of the photons can have an energy close to one of the molecular excitation energies, and will achieve intermediate state resonance.

Table II. Measured Rhodamine 6G TPA cross section compared with previous literature

Reference	Wavelength (nm)	TPA cross section (GM)	Method	Laser	Pulse duration
[14]	694	180 ± 20	NLT[a]	Ruby	15 ps
[15]	694	355 ± 170	TPIF[b]	Ruby	40 ns
[7]	690	120	TPIF	Ti:Sapphire	100 fs
	700	150			
	720	38			
[12]	680	55	TPIF	OPA	160 fs
	694	112 ± 12			
	710	94			
This work (include errors)	675.7	337 ± 40	NWLP[c]	WLSC	103 fs[d]
	683.4	486 ± 57			
	691.0	596 ± 69			
	699.3	324 ± 36			
	707.4	139 ± 15			

[a]NLT: nonlinear transmission.

[b]TPIF: two photon induced fluorescence.

[c]NWLP: nondegenerate white light probe.

[d]Pump pulse duration.

4.4.6 Other dyes

More dyes are investigated in this work. They are rhodamine 123 (4.2 mM) dissolved in methanol, coumarin 343 (27.3 mM), Nile red (0.75 mM), and Nile blue A (0.68 mM) in chloroform. The samples are dissolved in chloroform even though it has poor solubility for the solutes used in the present study. The reason of using the solvent is to minimize the Raman signal due to the solvent, which disturbs the two-photon absorption signal. The TPA cross section results are shown in Fig.4.10 - Fig.4.13. The rhodamine 123, coumarin 6, coumarin 343, Nile red and Nile blue A show efficient TPA peaks at 660 nm, 652 nm, 651 nm, 669 nm and 626 nm, respectively. The corresponded NDTPA cross sections are 776 GM, 1015 GM, 49 GM, 3270 GM and 1407 GM, respectively. The detail measured values are also shown in the Appendix II.

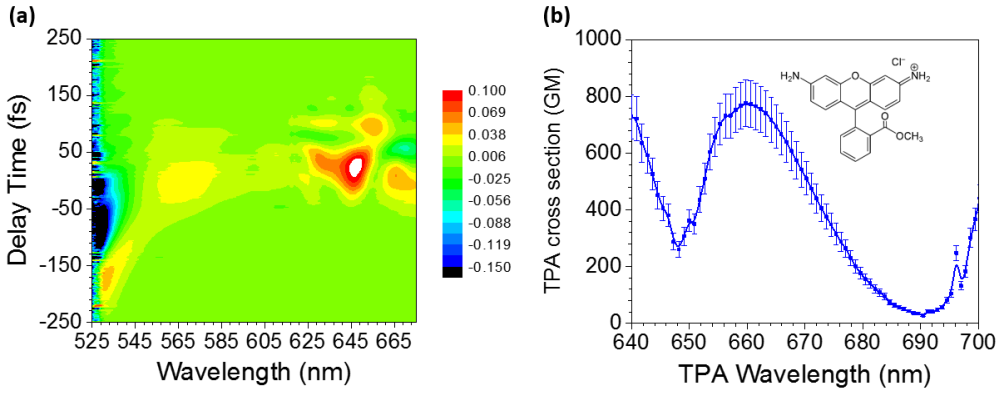

Fig.4.10 (a) Two-dimensional ΔA map for rhodamine 123 in methanol. (b) Measured TPA cross section spectrum for rhodamine 123.

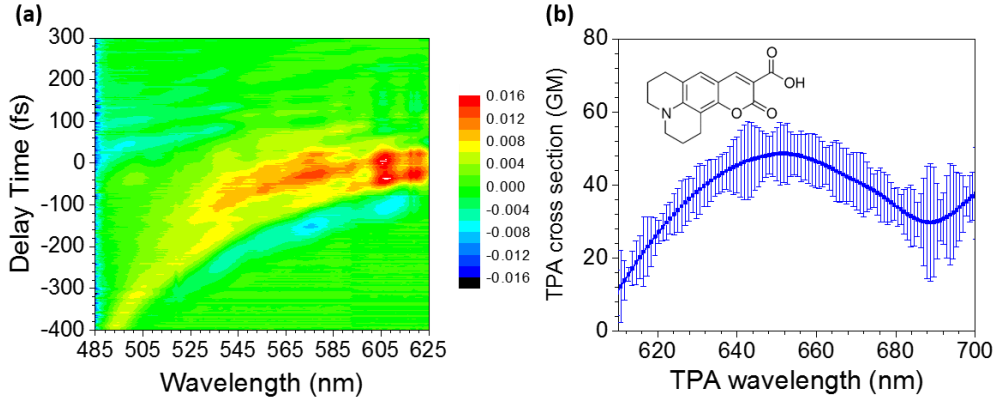

Fig.4.11 (a) Two-dimensional ΔA map for coumarin 343 in chloroform. (b) Measured TPA cross section spectrum for coumarin 343.

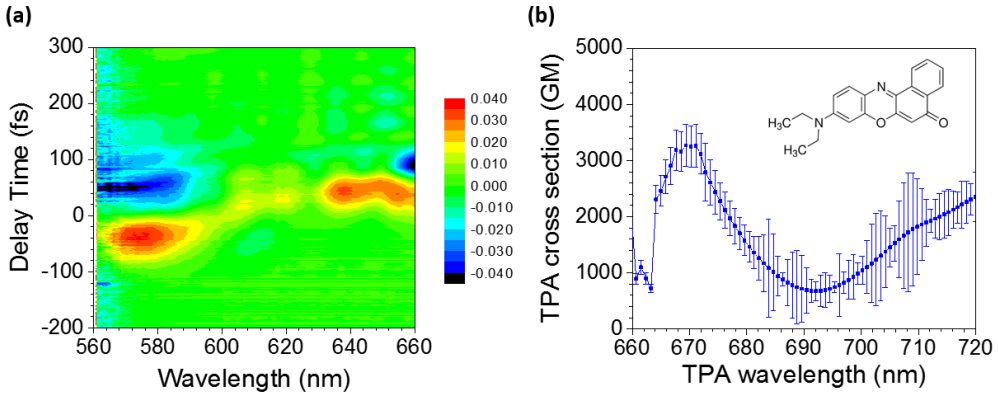

Fig.4.12 (a) Two-dimensional ΔA map for Nile red in chloroform. (b) Measured TPA cross section spectrum for Nile red.

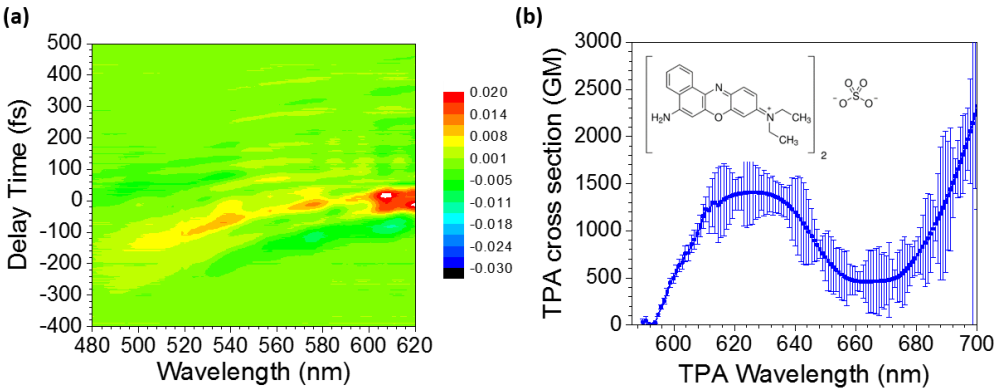

Fig.4.13 (a) two dimensional ΔA map for Nile blue A in chloroform. (b) Measured TPA cross section spectrum for Nile blue A.

4.5 Theoretical calculation conformation

To obtain theoretical investigation of our experimental results, we use quantum chemical few-state approaches to models both the linear and nonlinear optical responses of the chromophores of interest. This calculation is performed by our co-worker, C. Katan and J.A. Bjorgaard. To get theoretical confirmation of our experimental results, we have implemented quantum chemical and few states approaches for both linear and nonlinear optical responses of the chromophores of interest. We use density functional theory (DFT) and time-dependent (TD) DFT approaches, as implemented in the Gaussian 03 and 09 packages.[26,27] No simplifications are made for the chemical structures. The properties of interest are related to ground state geometry: that is, geometry optimization and one- and two-

photon absorption is related to the electronically excited states (ES). The polarizable continuum model (PCM) as implemented in Gaussian 09 and Gaussian 03 is used to simulate the solvent effects on geometries and optical spectra, respectively. No additional local field corrections are considered.[28] Optical spectra are obtained using the density matrix formalism for non-linear optical responses as proposed by Tretiak and Chernyak.[28,29] Absolute TPA amplitudes are derived using expression (38) of Ref. 28 for degenerate two-photon absorption (DTPA) considering both diagonal and non-diagonal contributions. For non-degenerate TPA, the TPA cross section is related to the imaginary part of the third-order polarizability $\gamma(-\omega_1; \omega_1,-\omega_2,\omega_2)$ and the frequency dependent prefactor ω_2 is replaced by $2\omega_1^2\,\omega_2 / (\omega_1+\omega_2)$ as in Ref. 23, where index 1 refers to the probe beam and index 2 refers to the pump beam. The calculated TPA spectra shown in Fig.4.14 are obtained at the TD-B3LYP/6-311+G*//B3LYP/6-311+G* level of theory in conventional quantum chemical notation "single point//optimization level" including up to 20 singlet ES. The damping factor introduced to simulate the finite line width Γ in the resonant spectra is fixed according to Table S1 in the Appendix III. The ES structure is further checked at the TD-ωB97xD/6-311+G*//B3LYP/6-311+G* level.

The calculated TPA cross sections are significantly larger than the experimental results shown in Fig.4.14. This may be attributed to a number of factors related to the level of theory in use. First, B3LYP, the most suitable exchange-correlation functional in Gaussian 03 for optical properties, is known to overestimate conjugation and thus reduce bond length alternation and overestimate transition dipole moments.[30] For example, if the TPA cross section scales as the fourth power of dipole moment matrix elements, 15% overestimation of the dipole moments may double the size of the TPA cross section. Next, the choice of a finite line width, which is set to be same for all ES, directly affects the TPA amplitudes. In fact, when the two-photon excited state is near resonance, the TPA amplitude scales as 1/Γ. In addition to local field corrections such as dynamic contributions,[28] other contributing factors include all of those currently considered in predictions of linear optical properties (band shape, amplitude and

position) of solvated chromophores.[31]

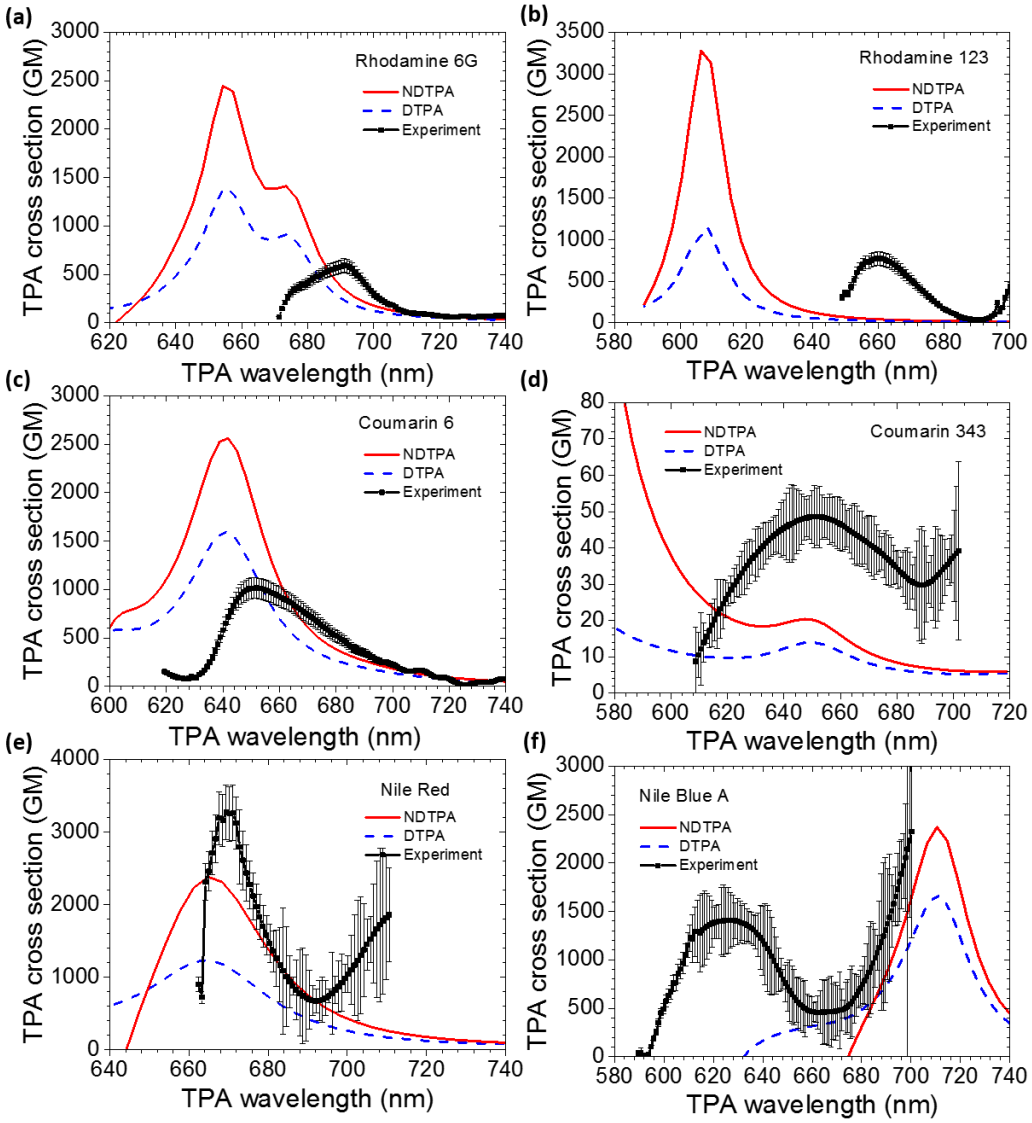

Fig.4.14 Measured and calculated TPA cross section for (a) rhodamine 6G, (b) rhodamine 123, (c) coumarin, 6 (d) coumarin 343 (e) Nile red and (f) Nile blue A. In each figure, black solid line with error bar are the measured experimental value; calculated DTPA and NDTPA spectrum (800 nm pump) are plotted in blue dash line and red solid line.

Specifically, the present solvation model is limited and does not account for state specific responses,[32] or for explicit solvent molecules or counter-ions. Furthermore, vibronic contributions[33] are not simulated. Despite all of these approximations, this level of theory has already proved efficient for rationalizing experimental TPA spectra.[28,32] The OPA spectra are systematically blue shifted compared to the experimental results. However, compared to the TD-B3LYP/6-31G(d)//HF/6-31G(d)

level of theory in a vacuum, both the solvent and a larger basis set bring the calculated and experimental spectra closer together.

Fig.4.14 shows the corresponding calculated TPA spectra for cases where the agreement between the calculated and experimental peak positions have been improved. However, some of the peak amplitudes are significantly overestimated (e.g., coumarin 6) due to the overestimation of dipole matrix elements within the B3LYP functional. Given the overall good agreement between the experimental and theoretical OPA band positions, NDTPA spectra are computed for the experimental pump wavelength only (1.55 eV/800nm). For most of the chromophores of interest, these TPA spectra reveal a TPA band that is close to that experimentally observed; the exception is Nile blue A, which has a TPA band close to 700 nm. These bands, which have significant magnitude, are related to one (or several) higher lying excited state(s) that could be, if necessary, identified from our calculations. The calculated spectra clearly demonstrate the intermediate state resonance enhancement, which depends on the excited state structure of the particular chromophore.

4.6 Conclusion

Compared with the broadly used method for TPA spectrum measurement, present method has the following several advantages: First, simplified system structure which less error sources. TPA coefficients could be directly calculated hence the data reliability could be highly confident. Second, a broadband TPA spectrum could be acquired in single measurement procedure. The error in the TPA spectral shape due to laser intensity fluctuation which is a serious problem of one-wavelength-to-the-other type experiment can be eliminated. However, this method has some points needed to be improved. First, many solvent contribute a strong Raman loss signal with Raman shift around 3000 cm^{-1} ~ 3300 cm^{-1}, such as water, methanol. This disturbance by the Raman loss effect must be minimized by selection of the solvent and the effect must be properly corrected. Second, the TPA spectrum detection range is very limited from 600 to 760 nm, while using 800 nm pumps in this work. To solve the problem,

choosing proper solvent like chloroform or changing pump beam wavelength to a variable range by OPA setup is a possible choice. Another feasible and easily available way is to use much wider WLSC, like generating with tapered fiber or photonic crystal fiber.[24]

The TPA spectrum for several types of the laser dyes are measured in this work, like xanthene dyes (rhodamine 6G and rhodamine 123), coumarin dyes (coumarin 6 and coumarin 343), oxazine dyes (Nile red and Nile blue A). By comparing the result of rhodamine 6G in this work to former degenerate measurements, enhancement for the TPA in non-degenerate case is also confirmed. The laser dyes (except rhodamine 6G and coumarin 6), up to our knowledge, are studied for the first time in the present work. By this method, the TPA spectrum measurement for materials have become much more convenient. It is useful for screening new TPA materials development. And this method has been already taken into the application with our collaborators, the groups of Prof. Abe in Hiroshima university.[35]

Appendix II

In this appendix, the measured data of non-degenerate TPA cross section for all the laser dyes investigated in this dissertation are summarized. As described in the section 4.4.1, the systematic wavelength resolution is considered to be about 10 nm due to the domination of pump pulse spectral width. However, with the high signal noise ratio and the fine wavelength resolution (less than 1 nm) provided by the MLA detection system, small spectral shift (less than 5 nm) could still be identified by this method. Therefore, all the measured results are summarized with an about 5 nm step resolution first, which are shown in the following.

Rhodamine 6G in methanol

λ (nm)	σ_2 (GM)	Error (GM)		λ (nm)	σ_2 (GM)	Error (GM)
673.1	197	23		714.6	92	10
677.4	370	44		718.6	78	9

681.7	452	53		722.5	63	7
686.0	530	62		726.3	65	7
690.2	581	67		730.2	62	7
694.3	522	60		734.0	66	8
698.5	359	40		737.8	71	8
702.6	234	26		741.5	74	8
706.6	161	18		745.2	90	9
710.6	106	11		748.9	112	13

Rhodamine 123 in methanol

λ (nm)	σ_2 (GM)	Error (GM)		λ (nm)	σ_2 (GM)	Error (GM)
650.9	393	41		677.9	232	27
655.3	685	73		682.1	124	15
659.8	767	82		686.3	57	7
664.2	715	79		690.4	36	4
668.5	575	65		694.5	108	12
672.8	409	48		698.6	285	32

Coumarin 6 in chloroform

λ (nm)	σ_2 (GM)	Error (GM)		λ (nm)	σ_2 (GM)	Error (GM)
622.2	112	12		674.5	638	74
626.9	85	9		678.8	545	64
631.6	120	13		683.0	467	55
636.3	310	34		687.1	381	44
640.9	647	70		691.3	325	38
645.5	910	97		695.4	262	30
650.0	1008	106		699.4	232	26
654.5	999	106		703.4	176	19
658.9	943	101		707.4	161	18
663.3	873	95		711.4	152	16
667.6	788	89		715.3	100	11

Coumarin 343 in chloroform

λ (nm)	σ_2 (GM)	Error (GM)		λ (nm)	σ_2 (GM)	Error (GM)
610.6	12	7		659.8	47	7
615.5	20	7		664.2	44	7
620.3	27	5		668.5	42	7
625.1	33	6		672.8	40	7
629.8	38	6		677.1	37	6
634.4	42	5		681.3	33	5
639.1	45	7		685.5	31	8

643.6	47	10		689.6	30	12
648.2	48	6		693.7	32	11
652.7	49	7		697.8	35	7
656.2	48	6		701.0	38	19

Nile red in chloroform

λ (nm)	σ_2 (GM)	Error (GM)		λ (nm)	σ_2 (GM)	Error (GM)
664.2	1821	201		689.6	722	491
668.5	3155	359		693.7	700	218
672.8	2844	409		697.8	879	336
677.1	1979	311		701.8	1170	609
681.3	1366	344		705.8	1522	585
685.5	949	489		567.5	1435	712

Nile blue A in chloroform

λ (nm)	σ_2 (GM)	Error (GM)		λ (nm)	σ_2 (GM)	Error (GM)
591.7	22	18		650.9	683	268
596.8	270	30		655.3	538	263
601.8	625	69		659.8	470	136
606.7	909	100		664.2	460	279
611.6	1237	218		668.5	468	312
616.5	1324	357		672.8	498	249
621.3	1389	218		677.1	606	271
626.0	1406	322		681.3	788	286
630.7	1389	205		685.5	1021	369
635.4	1326	163		689.6	1309	689
640.0	1193	354		693.7	1655	330
644.6	988	338		697.8	2058	873

As a form of recording, the raw data of the measured non-degenerated two photon absorption cross section for each investigated laser dyes are decided to be listed in the following pages. Fine wavelength resolution here is due to the benefaction by the multi-channel lock-in detection.

Rhodamine 6G in methanol (raw data)

λ (nm)	σ_2 (GM)	Error (GM)		λ (nm)	σ_2 (GM)	Error (GM)
671.4	58	7		713.0	96	10
672.2	145	17		713.8	94	10
673.1	212	25		714.6	93	10
674.0	263	31		715.4	91	9

674.8	307	36		716.2	88	9
675.7	338	40		717.0	86	9
676.6	357	42		717.8	82	9
677.4	372	44		718.6	77	9
678.3	383	45		719.3	73	8
679.1	398	47		720.1	71	8
680.0	415	49		720.9	67	8
680.9	436	51		721.7	64	7
681.7	454	53		722.5	63	7
682.6	471	55		723.2	61	7
683.4	486	57		724.0	61	7
684.3	501	59		724.8	61	6
685.1	518	60		725.6	61	6
686.0	533	62		726.3	67	7
686.8	545	63		727.1	67	7
687.6	555	64		727.9	67	7
688.5	566	66		728.7	66	7
689.3	573	66		729.4	61	6
690.2	582	67		730.2	61	6
691.0	596	69		731.0	62	7
691.8	586	67		731.7	62	7
692.7	574	66		732.5	64	7
693.5	555	64		733.2	65	8
694.3	525	60		734.0	66	8
695.2	494	56		734.8	68	8
696.0	460	52		735.5	69	8
696.8	425	47		736.3	70	8
697.6	395	44		737.0	72	8
698.5	357	40		737.8	72	8
699.3	324	36		738.5	71	8
700.1	295	33		739.3	71	8
700.9	272	30		740.0	72	8
701.7	251	28		740.8	72	8
702.6	234	26		741.5	73	8
703.4	215	24		742.3	75	8
704.2	198	22		743.0	78	8
705.0	189	21		743.7	81	8
705.8	181	20		744.5	85	9
706.6	166	19		745.2	89	9
707.4	139	15		746.0	95	10
708.2	128	14		746.7	100	11
709.0	118	13		747.4	104	11
709.8	109	12		748.2	108	12

710.6	105	11		748.9	113	13
711.4	100	11		749.6	114	13
712.2	99	10		750.4	123	14

Rhodamine 123 in methanol (raw data)

λ (nm)	σ_2 (GM)	Error (GM)		λ (nm)	σ_2 (GM)	Error (GM)
649.1	307	32		676.2	287	34
650.0	362	38		677.1	264	31
650.9	350	37		677.9	230	27
651.8	436	46		678.8	201	24
652.7	510	54		679.6	176	21
653.6	604	64		680.4	155	18
654.5	656	70		681.3	140	17
655.3	703	75		682.1	121	14
656.2	732	78		683.0	108	13
657.1	732	78		683.8	95	11
658.0	753	80		684.6	74	9
658.9	767	82		685.5	64	7
659.8	776	83		686.3	56	7
660.6	772	82		687.1	50	6
661.5	766	82		688.0	43	5
662.4	755	82		688.8	36	4
663.3	741	81		689.6	34	4
664.2	719	79		690.4	27	3
665.0	694	77		691.3	42	5
665.9	668	75		692.1	41	5
666.8	639	72		692.9	47	5
667.6	608	69		693.7	57	7
668.5	575	65		694.5	81	9
669.4	542	62		695.4	105	12
670.2	511	59		696.2	248	28
671.1	474	55		697.0	132	15
671.9	441	51		697.8	184	21
672.8	407	47		698.6	301	33
673.7	376	44		699.4	367	40
674.5	348	41		700.2	441	49
675.4	315	37				

Coumarin 6 in chloroform (raw data)

λ (nm)	σ_2 (GM)	Error (GM)		λ (nm)	σ_2 (GM)	Error (GM)
620.3	137	15		672.8	680	79

621.3	122	13		673.7	663	77
622.2	109	12		674.5	637	74
623.2	100	11		675.4	616	72
624.1	91	10		676.2	596	70
625.1	84	9		677.1	580	68
626.0	81	9		677.9	559	66
626.9	79	9		678.8	541	64
627.9	82	9		679.6	526	62
628.8	101	11		680.4	517	61
629.8	85	9		681.3	503	59
630.7	91	10		682.1	484	57
631.6	118	13		683.0	468	55
632.6	140	15		683.8	449	53
633.5	168	18		684.6	430	50
634.4	205	23		685.5	403	47
635.4	248	27		686.3	391	45
636.3	300	33		687.1	381	44
637.2	364	40		688.0	372	43
638.1	432	47		688.8	360	42
639.1	509	55		689.6	352	41
640.0	580	63		690.4	340	39
640.9	650	70		691.3	328	38
641.8	717	77		692.1	311	36
642.7	779	84		692.9	296	34
643.6	832	89		693.7	281	32
644.6	878	94		694.5	270	31
645.5	916	97		695.4	261	29
646.4	950	101		696.2	247	28
647.3	974	103		697.0	252	28
648.2	994	105		697.8	248	28
649.1	1006	106		698.6	241	27
650.0	1012	106		699.4	232	26
650.9	1014	106		700.2	224	25
651.8	1015	107		701.0	214	23
652.7	1010	106		701.8	199	22
653.6	1010	107		702.6	185	20
654.5	1000	106		703.4	173	19
655.3	991	105		704.2	163	18
656.2	983	105		705.0	158	18
657.1	969	103		705.8	155	17
658.0	956	102		706.6	157	17
658.9	944	101		707.4	160	18
659.8	931	100		708.2	166	18

660.6	917	98		709.0	168	18
661.5	902	97		709.8	168	18
662.4	888	96		710.6	164	17
663.3	875	95		711.4	155	16
664.2	860	95		712.2	143	15
665.0	842	93		712.9	131	14
665.9	824	92		713.7	116	12
666.8	806	91		714.5	105	11
667.6	788	89		715.3	96	10
668.5	769	88		716.1	93	10
669.4	751	86		716.8	90	10
670.2	733	84		717.6	95	10
671.1	717	83		718.4	91	10
671.9	700	81		719.2	85	10

Coumarin 343 in chloroform (raw data)

λ (nm)	σ_2 (GM)	Error (GM)		λ (nm)	σ_2 (GM)	Error (GM)
608.7	9	10		658.0	47	7
609.7	11	6		658.9	47	7
610.6	12	10		659.8	47	7
611.6	14	5		660.6	46	7
612.6	16	2		661.5	46	6
613.6	17	5		662.4	45	5
614.5	19	6		663.3	45	6
615.5	20	6		664.2	44	7
616.5	22	10		665.0	44	8
617.4	23	8		665.9	43	8
618.4	25	7		666.8	43	7
619.3	26	5		667.6	42	8
620.3	27	3		668.5	42	6
621.3	28	4		669.4	42	7
622.2	30	5		670.2	41	8
623.2	31	4		671.1	41	8
624.1	32	6		671.9	40	9
625.1	33	6		672.8	40	7
626.0	34	7		673.7	39	6
626.9	35	6		674.5	39	5
627.9	36	6		675.4	38	6
628.8	37	5		676.2	37	7
629.8	38	7		677.1	37	7
630.7	39	7		677.9	36	7
631.6	40	6		678.8	35	5

632.6	41	6		679.6	35	4
633.5	41	6		680.4	34	5
634.4	42	5		681.3	33	4
635.4	43	5		682.1	33	6
636.3	43	5		683.0	32	7
637.2	44	5		683.8	32	8
638.1	44	6		684.6	31	8
639.1	45	7		685.5	31	5
640.0	45	8		686.3	30	7
640.9	46	9		687.1	30	12
641.8	46	10		688.0	30	15
642.7	47	11		688.8	30	16
643.6	47	10		689.6	30	15
644.6	47	9		690.4	30	10
645.5	48	8		691.3	30	6
646.4	48	7		692.1	31	7
647.3	48	6		692.9	31	11
648.2	48	5		693.7	32	14
649.1	48	6		694.5	33	13
650.0	49	7		695.4	33	10
650.9	49	9		696.2	34	9
651.8	49	8		697.0	35	8
652.7	49	8		697.8	35	4
653.6	49	6		698.6	36	6
654.5	48	5		699.4	37	7
655.3	48	6		700.2	38	13
656.2	48	7		701.0	38	18
657.1	48	6		701.8	39	25

Fluorescein in methanol (raw data)

λ (nm)	σ_2 (GM)	Error (GM)		λ (nm)	σ_2 (GM)	Error (GM)
586.7	23	1		647.3	103	5
587.7	39	2		648.2	91	5
588.7	25	1		649.1	83	4
589.7	41	2		650.0	78	4
590.7	32	2		650.9	74	4
591.7	57	3		651.8	74	4
592.8	41	2		652.7	73	4
593.8	66	3		653.6	78	4
594.8	49	2		654.5	80	4
595.8	42	2		655.3	84	4

596.8	45	2		656.2	84	4
597.8	58	3		657.1	81	4
598.8	49	2		658.0	80	4
599.8	53	3		658.9	81	4
600.8	60	3		659.8	78	4
601.8	69	3		660.6	75	4
602.8	59	3		661.5	74	4
603.8	67	3		662.4	74	4
604.7	63	3		663.3	79	4
605.7	72	4		664.2	89	4
606.7	73	4		665.0	100	5
607.7	75	4		665.9	113	6
608.7	82	4		666.8	126	6
609.7	89	4		667.6	132	7
610.6	89	5		668.5	135	7
611.6	94	5		669.4	129	6
612.6	99	5		670.2	124	6
613.6	100	5		671.1	109	5
614.5	102	5		671.9	95	5
615.5	105	5		672.8	85	4
616.5	109	5		673.7	80	4
617.4	110	6		674.5	79	4
618.4	110	6		675.4	81	4
619.3	109	5		676.2	82	4
620.3	108	5		677.1	80	4
621.3	111	6		677.9	75	4
622.2	114	6		678.8	66	3
623.2	114	6		679.6	61	3
624.1	113	6		680.4	54	3
625.1	115	6		681.3	52	3
626.0	116	6		682.1	56	3
626.9	118	6		683.0	66	3
627.9	121	6		683.8	86	4
628.8	128	6		684.6	104	5
629.8	124	6		685.5	129	7
630.7	127	6		686.3	147	7
631.6	126	6		687.1	155	8
632.6	123	6		688.0	159	8
633.5	119	6		688.8	158	8
634.4	117	6		689.6	154	8
635.4	116	6		690.4	157	8
636.3	116	6		691.3	161	8
637.2	121	6		692.1	166	8

638.1	123	6		692.9	173	9
639.1	130	7		693.7	187	9
640.0	136	7		694.5	227	11
640.9	144	7		695.4	263	13
641.8	148	7		696.2	287	14
642.7	148	7		697.0	294	15
643.6	144	7		697.8	296	15
644.6	137	7		698.6	295	15
645.5	129	6		699.4	257	13
646.4	117	6		700.2	245	12

Nile red in chloroform (raw data)

λ (nm)	σ_2 (GM)	Error (GM)		λ (nm)	σ_2 (GM)	Error (GM)
662.4	902	98		688.0	782	594
663.3	725	79		688.8	744	654
664.2	2309	254		689.6	714	592
665.0	2457	272		690.4	692	405
665.9	2713	303		691.3	679	209
666.8	2906	327		692.1	674	170
667.6	3188	360		692.9	679	277
668.5	3161	360		693.7	692	309
669.4	3270	374		694.5	714	241
670.2	3251	374		695.4	743	93
671.1	3264	377		696.2	781	563
671.9	3120	362		697.0	826	185
672.8	2791	514		697.8	875	350
673.7	2610	406		698.6	928	391
674.5	2437	386		699.4	984	191
675.4	2273	328		700.2	1042	253
676.2	2118	324		701.0	1103	473
677.1	1971	307		701.8	1167	693
677.9	1832	312		702.6	1234	825
678.8	1702	283		703.4	1304	801
679.6	1579	272		704.2	1377	641
680.4	1465	266		705.0	1451	347
681.3	1359	284		705.8	1525	317
682.1	1260	388		706.6	1596	681
683.0	1169	511		707.4	1662	939
683.8	1085	872		708.2	1722	1059
684.6	1010	687		709.0	1775	1006
685.5	941	358		709.8	1820	853

686.3	880	119		710.6	1860	644
687.1	827	411				

Nile blue A in chloroform (raw data)

λ (nm)	σ_2 (GM)	Error (GM)		λ (nm)	σ_2 (GM)	Error (GM)
589.7	30	36		649.1	760	189
590.7	41	50		650.0	719	252
591.7	11	1		650.9	680	317
592.8	2	1		651.8	645	295
593.8	26	3		652.7	613	287
594.8	103	11		653.6	584	232
595.8	190	21		654.5	558	266
596.8	254	28		655.3	535	267
597.8	351	39		656.2	515	260
598.8	450	49		657.1	498	291
599.8	495	54		658.0	485	164
600.8	574	63		658.9	474	157
601.8	633	70		659.8	467	150
602.8	665	73		660.7	462	100
603.8	758	83		661.5	460	108
604.7	763	84		662.4	459	174
605.7	859	94		663.3	459	222
606.7	905	100		664.2	460	335
607.7	967	106		665.0	461	327
608.7	1050	116		665.9	463	335
609.7	1155	128		666.8	464	349
610.6	1227	136		667.6	465	369
611.6	1217	247		668.5	467	283
612.6	1294	256		669.4	470	302
613.6	1294	322		670.2	474	256
614.5	1273	395		671.1	479	398
615.5	1305	377		671.9	486	214
616.5	1329	380		672.8	495	93
617.4	1348	336		673.7	505	267
618.4	1363	296		674.5	523	271
619.3	1375	240		675.4	546	359
620.3	1384	162		676.2	573	364
621.3	1391	170		677.1	604	255
622.2	1396	174		677.9	636	217
623.2	1401	346		678.8	671	162
624.1	1404	373		679.6	708	186

625.1	1406	345		680.4	746	192
626.0	1407	341		681.3	786	249
626.9	1407	288		682.1	829	338
627.9	1405	263		683.0	873	466
628.8	1402	184		683.8	919	476
629.8	1398	240		684.6	968	413
630.7	1391	219		685.5	1018	302
631.6	1383	178		686.3	1071	180
632.6	1373	205		687.1	1127	476
633.5	1361	166		688.0	1184	707
634.4	1346	160		688.8	1244	762
635.4	1329	163		689.6	1306	746
636.3	1308	158		690.4	1371	574
637.2	1285	169		691.3	1438	656
638.1	1259	222		692.1	1508	372
639.1	1229	330		692.9	1579	188
640.0	1196	357		693.7	1653	305
640.9	1160	417		694.5	1729	373
641.8	1121	446		695.4	1808	413
642.7	1079	429		696.2	1888	357
643.6	1035	401		697.0	1971	334
644.6	989	342		697.8	2056	555
645.5	942	293		698.6	2143	2328
646.4	895	224		699.4	2232	789
647.3	849	165		700.2	2323	1095
648.2	803	101				

Appendix III

Table S1. Photophysical data used for the simulations of the optical spectra. Γ_{TDDFT} corresponds to the half width at half maximum (HWHM) chosen for the Lorentzian line shapes within the TD-DFT based formalism[27]. All other parameters are relevant to the few state model.

	Γ_{TDDFT}[eV]	Γ_{model} [eV]	$\hbar\omega_{ge}$ [eV]	$\hbar\omega_{ge'}$ [eV]
Rho6G	0.05	0.05	2.33	3.59
Rho123	0.05	0.05	2.44	3.73
C6	0.10	0.10	2.725	3.76
C343	0.10	0.10	2.77	3.76
Nile Red	0.10	0.10	2.30	3.67/3.71
Nile Blue A	0.075	0.075	1.984	3.57/3.60/3.87

Reference:

1. G.S. He, J.D. Bhawalkar, C.F. Zhao, and P.N. Prasad, Appl. Phys. Lett. **67**, 2433 (1995).
2. M.A.M. Versteegh and J.I. Dijkhuis, Opt. Lett. **36**, 2776 (2011).
3. W.R. Zipfel, R.M. Williams, and W.W. Webb, Nat Biotech **21**, 1369 (2003).
4. W. Denk, Proc. Natl. Acad. Sci. USA **91**, 6629 (1994).
5. S.W. Hell, M. Booth, S. Wilms, C.M. Schnetter, A.K. Kirsch, D.J. Arndt-Jovin, and T.M. Jovin, Opt. Lett. **23**, 1238 (1998).
6. A. Hayat, A. Nevet, P. Ginzburg, and M. Orenstein, Semicond. Sci. Tech. **26**, 083001 (2011).
7. C. Xu and W.W. Webb, J. Opt. Soc. Am. B **13**, 481 (1996).
8. M.A. Albota, C. Xu, and W.W. Webb, Appl. Opt. **37**, 7352 (1998).
9. Y. Tan, Q. Zhang, J. Yu, X. Zhao, Y. Tian, Y. Cui, X. Hao, Y. Yang, and G. Qian, Dyes and Pigments **97**, 58 (2013).
10. A. Nag, A.K. De, and D. Goswami, J. Phys. B: At. Mol. Opt. Phys. **42**, 065103 (2009).
11. Y. Xia, Y. Jiang, R. Fan, Z. Dong, W. Zhao, D. Chen, and G. Umesh, Opt. Laser Technol. **41**, 700 (2009).
12. N.S. Makarov, M. Drobizhev, and A. Rebane, Opt. Express **16**, 4029 (2008).
13. M. Drobizhev, S. Tillo, N.S. Makarov, T.E. Hughes, and A. Rebane, J. Phys. Chem. B **113**, 855 (2009).
14. P. Sperber and A. Penzkofer, Opt. Quant. Electron. **18**, 381 (1986).
15. J.P. Hermann and J. Ducuing, Opt. Commun. **6**, 101 (1972).
16. K.D. Belfield, D.J. Hagan, E.W. Van Stryland, K.J. Schafer, and R.A. Negres, Org. Lett. **1**, 1575 (1999).
17. S.A Kovalenko, A.L. Dobryakov, J. Ruthmann, and N.P. Ernsting, Phys. Rev. A **59**, 2369-2383

(1999).

18. C.M. Cirloganu, L.A. Padilha, D.A. Fishman, S. Webster, D.J. Hagan, and E.W. Van Stryland, Opt. Express **19**, 22951 (2011).

19. L.A. Padilha, J. Fu, D.J. Hagan, E.W. Van Stryland, C.L. Cesar, L.C. Barbosa, C.H.B. Cruz, D. Buso, and A. Martucci, Phys. Rev. B **75**, 075325 (2007).

20. G.S. He, L.-S. Tan, Q. Zheng, and P.N. Prasad, Chem. Rev. **108**, 1245 (2008).

21. Y.R. Shen, *The Principles of Nonlinear Optics* (J. Wiley, New York, 1984) p.203.

22. K.W. DeLong, R. Trebino, J. Hunter, and W.E. White, J. Opt. Soc. Am. B **11**, 2206 (1994).

23. B. Mallick, A. Lakhsmanna, and S. Umapathy, J. Raman Spectrosc. **42**, 1883 (2011).

24. J. Cascante-Vindas, A. Díez, J. L. Cruz, and M.V. Andrés, Opt. Express **18**, 14535 (2010).

25. J.M. Hales, D.J. Hagan, E.W. Van Stryland, K.J. Schafer, A.R. Morales, K.D. Belfield, P. Pacher, O. Kwon, E. Zojer, and J.L. Bredas, J. Chem. Phys **121**, 3152 (2004).

26. Gaussian 03, Revision D.02, M.J. Frisch, G.W. Trucks, H.B. Schlegel, G.E. Scuseria, M.A. Robb, J.R. Cheeseman, J.A. Montgomery, Jr., T. Vreven, K.N. Kudin, J.C. Burant, J.M. Millam, S.S. Iyengar, J. Tomasi, V. Barone, B. Mennucci, M. Cossi, G. Scalmani, N. Rega, G.A. Petersson, H. Nakatsuji, M. Hada, M. Ehara, K. Toyota, R. Fukuda, J. Hasegawa, M. Ishida, T. Nakajima, Y. Honda, O. Kitao, H. Nakai, M. Klene, X. Li, J.E. Knox, H.P. Hratchian, J.B. Cross, V. Bakken, C. Adamo, J. Jaramillo, R. Gomperts, R.E. Stratmann, O. Yazyev, A.J. Austin, R. Cammi, C. Pomelli, J.W. Ochterski, P.Y. Ayala, K. Morokuma, G.A. Voth, P. Salvador, J.J. Dannenberg, V.G. Zakrzewski, S. Dapprich, A.D. Daniels, M.C. Strain, O. Farkas, D.K. Malick, A.D. Rabuck, K. Raghavachari, J.B. Foresman, J.V. Ortiz, Q. Cui, A.G. Baboul, S. Clifford, J. Cioslowski, B.B. Stefanov, G. Liu, A. Liashenko, P. Piskorz, I. Komaromi, R.L. Martin, D.J. Fox, T. Keith, M.A. Al-Laham, C.Y. Peng, A. Nanayakkara, M. Challacombe, P.M.W. Gill, B. Johnson, W. Chen, M.W. Wong, C. Gonzalez, and J.A. Pople, Gaussian, Inc., Wallingford CT, 2004.

27. Gaussian 09, Revision A.02, M.J. Frisch, G.W. Trucks, H.B. Schlegel, G.E. Scuseria, M.A. Robb, J.R. Cheeseman, G. Scalmani, V. Barone, B. Mennucci, G.A. Petersson, H. Nakatsuji, M.

Caricato, X. Li, H.P. Hratchian, A.F. Izmaylov, J. Bloino, G. Zheng, J.L. Sonnenberg, M. Hada, M. Ehara, K. Toyota, R. Fukuda, J. Hasegawa, M. Ishida, T. Nakajima, Y. Honda, O. Kitao, H. Nakai, T. Vreven, J.A. Montgomery, Jr., J.E. Peralta, F. Ogliaro, M. Bearpark, J.J. Heyd, E. Brothers, K.N. Kudin, V.N. Staroverov, R. Kobayashi, J. Normand, K. Raghavachari, A. Rendell, J.C. Burant, S.S. Iyengar, J. Tomasi, M. Cossi, N. Rega, J.M. Millam, M. Klene, J.E. Knox, J.B. Cross, V. Bakken, C. Adamo, J. Jaramillo, R. Gomperts, R.E. Stratmann, O. Yazyev, A.J. Austin, R. Cammi, C. Pomelli, J.W. Ochterski, R.L. Martin, K. Morokuma, V.G. Zakrzewski, G.A. Voth, P. Salvador, J.J. Dannenberg, S. Dapprich, A.D. Daniels, Ö. Farkas, J.B. Foresman, J.V. Ortiz, J. Cioslowski, and D.J. Fox, Gaussian, Inc., Wallingford CT, 2009.

28. F. Terenziani, C. Katan, E. Badaeva, S. Tretiak, M. Blanchard-Desce, Advanced Materials, **20**, 4641 (2008)

29. S. Tretiak, V. Chernyak, J. Chem. Phys., **119**, 8809 (2003)

30. L. Ji, R.M. Edkins, L.J. Sewell, A. Beeby, A.S. Batsanov, K. Fucke, M. Drafz, J.A.K. Howard, O. Moutounet, F. Ibersiene, A. Boucekkine, E. Furet, Z. Liu, J.-F. Halet, C. Katan, T.B. Marder, Chem. Eur. J. 2014, **20**, 13618–13635

31. D. Jacquemin, C. Adamo, Computational Molecular Electronic Spectroscopy with TD-DFT, Topics in Current Chemistry, pp1-29, Springer Berlin Heidelberg 2015.

32. C. Katan, P. Savel, B. M. Wong, T. Roisnel, V. Dorcet, J.-L. Fillaut, D. Jacquemin, Phys. Chem. Chem. Phys. **16**, 9064–9073 (2014)

33. W. Liang, H. Ma, H. Zang and C. Ye, Int. J. Quantum Chem., **115**, 550–563 (2015)

34. J. Cascante-Vindas, A. Díez, J. L. Cruz, and M.V. Andrés, Opt. Express **18**, 14535 (2010).

35. S. Boinapally, B. Huang, M. Abe, C. Katan, J. Noguchi, S. Watanabe, H. Kasai, B. Xue, and T. Kobayashi, J. Org. Chem. **79**, 7822 (2014).

Chaptor 5: Summary

Pump probe spectroscopy is a powerful method to study dynamic processes in materials or chemical compounds. In this thesis, by using the femtosecond laser pulses, we investigate two kinds of photon induced incoherent and coherent phenomena in the different delay time domain:

The incoherent phenomena: the dynamics of excited states of RNA/DNA base molecule (uracil and thymine) by sub 10 femtosecond deep ultraviolet laser pulses excitation. From experimental result, two probe photon energy dependent lifetime constants are extracted from the difference absorption spectra measurement in the time range up to 1800 fs. From the lifetime constants, the relaxation processes through conical intersection (CI) are clearly understood. The shortest time constant less than 100 fs is assigned to due to relaxation through CI(S_2-S_1) from the first excited S_2 $^1(\pi\pi^*)$ state to the S_1 $^1(n\pi^*)$ state. The second shortest time constant about 1 picosecond is assigned to the relaxation through another CI(S_{2d}-S_0) from the deformed excited S_{2d} state to the S_0 ground state. Specially the location of CI(S_2-S_1) and CI(S_{2d}-S_0) are first time experimentally clarified at 4.33 eV and 4.36 eV for uracil, 4.45 eV and 4.36 for thymine. With the CI width of 0.21 eV and 0.038 eV for uracil, 0.05 eV and 0.031 eV for thymine, respectively.

The coherent phenomena: A new method for non-degenerate two photon absorption cross section measurement is demonstrated and applied for several laser dyes. We improve the traditional method by introducing white light supercontinuum probe and multi-channel lock-in detection. With the advantage of the simplified system structure ensured less error sources, broadband TPA coefficients can be directly acquired in single measurement procedure with high confident data reliability. In this work, several laser dye chromophores are investigated, several of them to be the first reported to our knowledge. Compare to reported degenerate TPA result, an enhancement phenomena is confirmed and discussed with the help of theoretical calculations.

Acknowledgment

My deepest gratitude goes first and foremost to Professor Kobayashi, my supervisor, for his constant encouragement and guidance. He has helped me to go through all the stages of the writing of this thesis. Without his consistent and illuminating instruction, this thesis could not have reached its present form.

A special thanks goes to the supervisor in my master degree, Professor Wenhui Fan, who led me into the world of modern science and introduced me to go advanced studies in Japan. He is not only the supervisor of my study but also the most important supervisor of my life.

Let me also say “thank you” to the following colleagues in Kobayashi Laboratory in UEC: Dr. Juan Du, Dr. Jinping He, Dr. Nan Wang, Dr. Jun Liu, Dr. Yongliang Jiang, Dr. Kida, Dr. Miyazaki, and Dr. Seto. Having scientific discussion with you guys at any time is a very fantastic thing; and also thanks to Professor Okuno, Professor Yabushita, Mr. Kawasumi and Miss. Yokoyama, Mr. Yamashita, Mr. Iiyama and Miss. Endo, and many kindness person I have met during the days.

Last my thanks would go to my beloved parents for their loving considerations and great confidence on me all through these years. And specially dedicated to my dear grandfather who fully supported my studies on abroad, wish you would be proud of me in the heaven. Thank you very much!

巻末：

論文題目　「Femtosecond spectroscopy studies of incoherent and coherent processes in DNA bases and laser dyes」

（和訳　核酸塩基及びレーザー色素のインコヒーレント・コヒーレント過程のフェムト秒分光）

関連論文の印刷公表の方法及び時期

全著者名　B. Xue, C. Katan, J.A. Bjorgaard, and T. Kobayashi

論文題目「Non-degenerate two photon absorption enhancement for laser dyes by precise lock-in detection」

平成27年12月AIP Advances雑誌5巻 127138（本文との関連）